

Interrogation Systems for Fiber Bragg Grating-Based Sensors

Maria-Iulia Comanici

Department of Electrical and Computer Engineering
McGill University
Montreal, Canada

June, 2010

A thesis submitted to McGill University in partial fulfilment of the requirements of the
degree of Master of Engineering

© Maria-Iulia Comanici

Abstract

As the potential application of fiber optic sensors broadens, there is much interest in finding measurement systems that are simple, cost effective and show high power efficiency. The latter is extremely useful when dealing with multiplexed sensors distributed over large distances, which results in high signal attenuation and limits the number of sensors that can be interrogated by a minimum number of measurement units. In this thesis we explore a fiber laser-based wavelength-to-power mapping interrogation system for wavelength-division-multiplexed FBG sensors, and we prove that such solution offers increased measurement reliability with high power efficiency.

Another aspect of improving the performance of sensing systems is the ability to measure multiple parameters, which are extremely useful when working with FBG-based sensors experiencing similar changes in spectral characteristics in response to changes in temperature or strain. These can be discriminated when they can be measured using different interrogation methods. For this purpose, we first explore and evaluate the performance of a vibration sensor designed by QPS Photonics, and we prove that it can be used to measure temperature and/or strain by translating the changes in its sinusoidal multi-wavelength spectrum to changes in the response of a single pass-band microwave photonic filter (MPF). The operation principle is based on monitoring the shift of the main filter band as temperature or strain changes. We demonstrate that such a system can achieve high-speed measurement with variable sensitivity.

Abrégé

Avec la croissance de l'application potentielle des capteurs à fibres optiques, il est important de trouver des systèmes de mesure simples, à coût réduit, et présentant une efficacité de puissance élevée. Celle-ci est extrêmement utile quand il s'agit de multiplexer des capteurs distribués sur des grandes distances, ce qui contribue à l'augmentation de l'atténuation du signal optique et impose une limite au nombre de capteurs qui peuvent être interrogés en utilisant un minimum d'unités de mesure. Dans cette thèse nous explorons un système d'interrogation basé sur un laser à fibre optique pour réaliser la traduction de la longueur d'onde en une mesure de puissance pour les capteurs à base de réseaux de Bragg. Nous prouvons que grâce à cette solution nous pouvons augmenter la fiabilité de la mesure avec une efficacité de puissance élevée ainsi que de réduire les erreurs de la mesure.

Pour augmenter la performance d'un système de capteurs, il est aussi important de pouvoir mesurer de paramètres additionnels. Ceci est extrêmement important quand le capteur est basé sur des réseaux de Bragg qui ont une réponse similaire aux changements de température ou tension. Ces deux facteurs peuvent être distingués en utilisant des méthodes d'interrogation différentes. Ainsi, nous explorons et évaluons premièrement la performance d'un capteur de vibration conçu par QPS Photonics. Nous prouvons qu'il est possible de mesurer aussi la température et/ou la tension en traduisant les changements du spectre à plusieurs longueurs d'onde en des changements de la réponse d'un filtre à micro-ondes photoniques (MPF) à une seule bande passante. Le principe de l'opération du système est basé sur la surveillance du déplacement de la bande passante principale du filtre quand la température ou la tension de la fibre changent. Nous montrons qu'un tel système est capable d'assurer une mesure très rapide avec une sensibilité variable.

Acknowledgements

First, I thank my supervisor, Professor Lawrence Chen, for his constant dedication at giving guidance and advice to help me improve my practical and analytical skills to attain my research goals. It has been an honour working with you for the past two years.

Second, I am grateful for the financial support provided by the Canadian Institute fo Photonic Innovations Technology, Exploitation, and Networking Grant with QPS Photonics. I thank Dr. Peter Kung, the founder and director of the company, for the additional help with providing equipment for the experiments involved in the project. I strongly appreciate the work of the people I met at the company. They were always available to share their expertise to help me acquire additional skills. Moreover, I am thankful to the team at Optech, who have allowed me to use their equipment for conducting a number of experiments at their lab.

Working within the Photonic Systems Group at McGill University has given me the opportunity to meet amazing people. I thank them for their help and friendship. I am grateful to Professors Andrew Kirk and Martin Rochette, who have shared their knowledge by teaching a number of undergraduate and graduate courses. I thank Dr. Pegah Seddighian for assisting with the project and for teaching me a number of practical skills during these two years. I also thank Dr. Victor Torres-Company, and Dr. Chen Chen for their availability on numerous occasions, when they helped me to either debug problems, or to use a number of measurement instruments. I thank Dr. Joshua Schwartz for always being available and prompt at providing me with the equipment necessary for the experimental setup. I thank Sandrine for her assistance with writing the abstract in French and being a great friend.

Last but not least, I am extremely grateful to my family for their always being available when I needed help and support the most. I thank my brothers: Johnny for being there for me, Silviu for always being cheerful, helpful, and, whenever possible, ready to escort me to or from school when I had pressing matters to deal with; and Ghita, who has been a great friend and always ready to give a helping hand. I also thank his fiancé Demetra, who was a real friend. I feel blessed to have my young sister Elena, who always succeeded at putting a smile on my face. I thank my parents Mariana and Ioan, who

always put their interests aside to attend to the needs of their children. My mother has been a remarkable parent and my best friend. I am extremely grateful to my father for the interest in my success he always showed. He taught me the valuable study skills that helped me achieve my goals.

Table of Contents

List of Figures	7
List of Acronyms	13
1. Introduction	14
1.1 <i>Fiber Optic Sensing</i>	14
1.2 <i>Characteristics of Fiber Optic Sensor Systems</i>	14
1.3 <i>Types of Fiber Optic Sensors</i>	15
1.4 <i>Fiber Bragg Grating (FBG) Sensors</i>	16
1.5 <i>Motivation and Thesis Contributions</i>	18
1.6 <i>References</i>	20
2. Fiber Bragg Gratings Background.....	22
2.1 <i>Introduction</i>	22
2.2 <i>Principles Behind FBGs Fabrication</i>	23
2.3 <i>Coupling Properties of FBGs</i>	25
2.3.1 <i>Non-uniform FBGs Used as Sensors</i>	27
2.4 <i>Strain and Temperature Effect on FBGs</i>	28
2.4.1 <i>Strain Effect on FBGs</i>	28
2.4.2 <i>Temperature Effect on FBGs</i>	29
2.4.3 <i>FBG Temperature and Strain Sensors Interrogation</i>	29
2.4.4 <i>Temperature Independent Strain Sensing</i>	31
2.5 <i>Summary</i>	32
2.6 <i>References</i>	33
3. Fiber Bragg Grating Vibration Sensors for Condition Monitoring	37
3.1 <i>Introduction</i>	37
3.2 <i>VibroFiber™ System Design</i>	38
3.2.1 <i>Operation Principle</i>	38
3.2.2 <i>Sensor Packaging</i>	40
3.2.3 <i>Sensor Measurement System and Instrumentation</i>	41
3.3 <i>Sensor Test Characterization</i>	44
3.3.1 <i>Frequency Response Measurement</i>	44
3.3.2 <i>Amplitude Response Measurement</i>	46
3.3.3 <i>Repeatability Test</i>	47
3.4 <i>Case Study</i>	50
3.4.1 <i>Sensor 1300-10</i>	50
3.4.2 <i>Sensor 1300-19</i>	52
3.4.3 <i>Sensor 1300-20</i>	54
3.4.4 <i>Sensor V1300-22</i>	56
3.5 <i>Summary of Measurement Results</i>	58
3.6 <i>Power Budget for TDM Applications</i>	60

3.6.1	Objective.....	60
3.6.2	Power Budget Experiment.....	61
3.7	<i>Discussion and Summary</i>	66
3.8	<i>References</i>	68
 4. Microwave Photonic Filter-based Interrogation System for VibroFiber™ Sensors.....		70
4.1	<i>Introduction</i>	70
4.2	<i>Microwave Photonic Filter Background</i>	71
4.3	<i>Fiber Bragg Grating Pair Based Sensor Temperature Response</i>	73
4.4	<i>Microwave Photonic Filter-based Temperature Measurement</i>	78
4.4.1	Temperature Effect on the Response of a MPF.....	78
4.4.2	Effect of Delay Fiber Length on the Characteristics of the MPF.....	79
4.4.3	Temperature Measurement Using a MPF System.....	82
4.5	<i>Conclusion and Discussion</i>	87
4.6	<i>References</i>	88
 5. Improved Arrayed Waveguide Grating-based Interrogation System for Fiber Bragg Grating Sensors.....		90
5.1	<i>Introduction</i>	90
5.2	<i>Fiber Laser Systems</i>	92
5.3	<i>AWGs as Edge Filter Components</i>	94
5.4	<i>Experimental Setup and Measurement Method</i>	97
5.5	<i>Experimental Results</i>	100
5.5.1	Using an SOA as Broadband Source.....	100
5.5.2	Using an EDFA as Broadband Source.....	107
5.5.3	Continuous-Time Measurement Results.....	111
5.6	<i>Discussion and Conclusion</i>	117
5.7	<i>References</i>	119
 6. Conclusion and Future Work.....		122

List of Figures

Figure 1.1: Fiber optic sensing system: a) transmission mode; b) reflection mode.	15
Figure 2.1: Schematic for the coupling between the wave reflected off the FBG and the input wave [2.8].	22
Figure 2.2: Interferometric method of writing FBGs in optical fiber's core [2.1].	24
Figure 2.3: Phase-mask (diffraction based) FBG writing method [2.6].	25
Figure 2.4: OSA based interrogation system for FBG strain or temperature sensors.	29
Figure 2.5: Passive interrogation system for FBGs [2.30].	30
Figure 3.1: Schematic for the VibroFiber™ sensor head.	39
Figure 3.2: Fiber Fabry-Perot cavity reflection spectrum for different reflectivities of the interferometer reflectors.	39
Figure 3.3: Reflection Spectrum for a VibroFiber™ sensor.	39
Figure 3.4: Sensor head placement inside the protection case.	40
Figure 3.5: Type B package: a) Three dimensional view of the individual components; b) Transverse view of the sensor head that is placed inside the sensor protection case.	41
Figure 3.6: Controlled sensor test system.	41
Figure 3.7: The method to place the sensor on the shaker plate: (a) physical, (b) pictorial.	42
Figure 3.8: VibroFiber™ detection system.	42
Figure 3.9: Wavelength at which the laser is biased for the vibration measurement.	43
Figure 3.10: User interface illustrating the measurement of the vibration signal.	44
Figure 3.11: Measured frequency response for a VibroFiber™ vibration sensor (sensor package of type A).	45
Figure 3.12: Amplitude response plot for a vibration sensor (sensor package of type A).	47
Figure 3.13: Qualitative characterization of the vibration sensor measurement repeatability (sensor package of type A): M1 to M8 represent the different measurements recorded.	48
Figure 3.14: Design for sensor 1300-10.	50
Figure 3.15: Frequency response for sensor V1300-10.	51

Figure 3.16: Plot of the measured value as a function of vibration amplitude at frequency 100 Hz for sensor V1300-10.....	52
Figure 3.17: Design for sensor 1300-19.	52
Figure 3.18: Frequency response for sensor V1300-19.....	53
Figure 3.19: Plot of the measured value as a function of vibration amplitude at 100 Hz for sensor V1300-19.	54
Figure 3.20: Design for sensor 1300-20.	54
Figure 3.21: Frequency response for sensor V1300-20.....	55
Figure 3.22: Plot of the measured value as a function of vibration amplitude at 100 Hz for sensor V1300-20.	55
Figure 3.23: Design for sensor 1300-22.	56
Figure 3.24: Frequency response for sensor V1300-22.	56
Figure 3.25: Plot of the measured value as a function of vibration amplitude at frequency 100 Hz for sensor V1300-22.....	57
Figure 3.26: Spectrum of sensor 1300-22 when the frequency is 150 Hz and the vibration amplitude is 10 μm	57
Figure 3.27: Power budget measurement system.	61
Figure 3.28: The system of N cascaded sensors: continuous vertical line represents a connector; double oblique lines represent the sensor double grating configuration. Note that the vertical lines represent APC connectors or splices.	62
Figure 3.29: Number of sensors that may be interrogated as a function of reflectivity, at different total lengths, when the input power is 10 dBm, the sensors are connected using splicing, and the last sensor reflectivity is 0.1.	63
Figure 3.30: Number of sensors that may be interrogated as a function of sensor reflectivity, at different total lengths, when the input power is 10 dBm, the sensors are connected using APC connectors, and the last sensor reflectivity is 0.1.....	63
Figure 3.31: Number of sensors that may be interrogated for two different last sensor reflectivity values when the input power is 0 dBm, the fiber length is 10 km and the sensors are connected using splicing.	64

Figure 3.32: Number of sensors that can be interrogated as a function of sensor reflectivity when the input power is -9.15 dBm, the sensors are connected using splicing over a distance of 10 km, and the last sensor reflectivity is 0.8.	65
Figure 4.1: General schematic for a MPF system [4.3][4.4].	71
Figure 4.2: Setup used to measure FBG pair spectrum change with temperature.	74
Figure 4.3: FBG comparison of reflection spectra at room temperature and at a) 100°C , and at b) 50°C.	75
Figure 4.4: Reflection spectrum center wavelength of an FBG pair as a function of temperature.	76
Figure 4.5: MPF response at room temperature when the single mode fiber length is 85 km.	79
Figure 4.6: First maximum superimposed on the estimated wavelength spacing between the filter peaks as functions of SMF fiber length.	80
Figure 4.7: Experimental setup used to find the optimum SMF fiber length.	80
Figure 4.8: MPF response superimposed on the dispersion response of the SMF fiber of length 85 km used as delay line.	81
Figure 4.9: Measured modulator transfer function over 20 GHz of RF frequency.	81
Figure 4.10: MPF experimental setup.	82
Figure 4.11: Shift in the MPF as temperature is increased from 25 to 100 °C.	83
Figure 4.12: Graph of power measured as temperature is increased for different modulator RF bias frequencies located on the rising edge of the second filter peak.	84
Figure 4.13: Graph of power measured as temperature is increased for different modulator RF bias frequencies located on the falling edge of the second filter peak.	84
Figure 4.14: Graph of normalized power variation as a function of temperature when the bias RF frequency is 8.98 GHz.	85
Figure 4.15: Graph of normalized power variation as a function of temperature when the bias RF frequency is 9.24 GHz.	86
Figure 5.1: Principle of mapping wavelength to power using an edge filter [5.1].	91
Figure 5.2: Fiber laser configurations: a) standing wave configuration; b) ring configuration.	92
Figure 5.3: (a) AWG geometric structure; (b) Geometric representation of the FPR.	95

Figure 5.4: Conventional wavelength to power mapping system.....	98
Figure 5.5: Standing wave fiber laser system used to achieve wavelength to power mapping.....	98
Figure 5.6: Ring fiber laser system used to achieve wavelength to power mapping.....	98
Figure 5.7: Mechanism to apply and measure strain.	99
Figure 5.8: FBG reflection spectra for the conventional wavelength to power mapping system.	101
Figure 5.9: FBG reflection spectra for the standing wave fiber laser wavelength to power mapping system.	101
Figure 5.10: FBG reflection spectra for the ring fiber laser wavelength to power mapping system.	102
Figure 5.11: Curve used to extract the zero strain point for the FBG whose reflection spectrum is centered at 1538.32 nm.....	103
Figure 5.12: Calibration curve for the FBG whose reflection spectrum is centered at 1538.32 nm.	103
Figure 5.13: Measured power as a function of strain plot.	104
Figure 5.14: Mapping curve showing the wavelength corresponding to the power level measured for different strain levels.....	105
Figure 5.15: Measured power at the output of the AWG corresponding to the FBG of reflection spectrum center wavelength at 1538.323 nm for the three wavelength-to-power mapping systems.....	106
Figure 5.16: Measured normalized power at the output of the AWG corresponding to the FBG of reflection spectrum center wavelength at 1538.32 nm for the three wavelength-to-power mapping systems used to evaluate measurement resolution.	106
Figure 5.17: In-house built EDFA for the FBG-based strain sensors interrogation systems.....	107
Figure 5.18: Measured power at the output of the AWG as a function of strain for the sensor whose reflection spectrum is centered at 1538.32 nm when the in-house built EDFA is used.	108

Figure 5.19: Measured power at the output of the AWG as a function of strain for the sensor whose reflection spectrum is centered at 1538.32 nm when a unidirectional EDFA is used.....	108
Figure 5.20: Normalized measured power at the output of the AWG as a function of strain for the sensor whose reflection spectrum is centered at 1538.32 nm when the in-house built EDFA is used.	109
Figure 5.21: Normalized measured power at the output of the AWG as a function of strain for the sensor whose reflection spectrum is centered at 1538.32 nm when a unidirectional EDFA is used.....	109
Figure 5.22: Spectral characteristic of FBG 2 when using the fiber laser configuration when an EDFA is used as gain medium.	110
Figure 5.23: Experimental setup for time-domain measurements using an RSOA.....	111
Figure 5.24: The FBG and AWG spectra when the former is placed in the ultrasonic bath at 25 °C.	112
Figure 5.25: Response to the ultrasonic signal when the FBG is placed in the ultrasonic bath at 25 °C.	112
Figure 5.26: The FBG and AWG spectra when the former is placed in the ultrasonic bath and water is heated to 50 °C.	113
Figure 5.27: Response to the ultrasonic signal when the FBG is placed in the ultrasonic bath at 50 °C.	113
Figure 5.28: DC amplitude level when the temperature is a) 25 °C, and b) 50 °C.....	114
Figure 5.29: FBG wavelength as a function of applied strain.	115
Figure 5.30: Measured mean amplitude measured with the oscilloscope at the output of the AWG channel corresponding to the FBG under test as a function of applied strain.	115
Figure 5.31: Wavelength-to-electric signal mean amplitude mapping when the FBG overlaps with a) the rising, and b) the falling edges of the AWG channel.	116

List of Tables

Table 3.1: Example of measuring the operability regions for a VibroFiber™	46
Table 3.3: Quantitative characterization of the VibroFiber™ measurement repeatability.	49
Table 3.4: Sensor versions V1295 with packages of type B.....	58
Table 3.5: Sensor versions V1300 with packages of type B.....	59
Table 3.6: Sensors with packages of type A.	59
Table 3.7: Sensor versions V1264 with packages of type A.	59
Table 3.8: Sensor versions V1300 with packages of type A	59
Table 3.9: Sensor versions V1280 with packages of type A.	60
Table 5.1: Summary of FBG reflection spectra measured bandwidths with the associated wavelength measurement errors.	102
Table 5.2: Summary of FBGs sensitivities to strain.	104
Table 5.3: Summary of FBG reflection spectra measured bandwidths with the associated wavelength measurement errors when an EDFA is used as BBS and as gain medium:110	

List of Acronyms

APC	Angle Polished Connector
ASE	Amplified Spontaneous Emission
AWG	Arrayed Waveguide Grating
BBS	Broadband Source
BW	Bandwidth
CW	Continuous-Wave
DC	Direct Current
EDFA	Erbium-Doped Fiber Amplifier
EO-MZM	Electro-Optic Mach-Zehnder Modulator
FBG	Fiber Bragg Grating
FSR	Free Spectral Range
FWHM	Full Width at Half Maximum
HPS	High Performance System
LCA	Lightwave Component Analyzer
LD	Laser Diode
LPG	Long Period Grating
MPF	Microwave Photonic Filter
MZM	Mach-Zehnder Modulator
OSA	Optical Spectrum Analyzer
RF	Radio Frequency
RSOA	Reflective Semiconductor Optical Amplifier
SMF	Single Mode Fiber
SOA	Semiconductor Optical Amplifier
TDM	Time-Division-Multiplexing
TEC	Thermo-Electric Controller
UV	Ultraviolet
VOA	Variable Optical Attenuator
WDM	Wavelength-Division-Multiplexing

1. Introduction

1.1 Fiber Optic Sensing

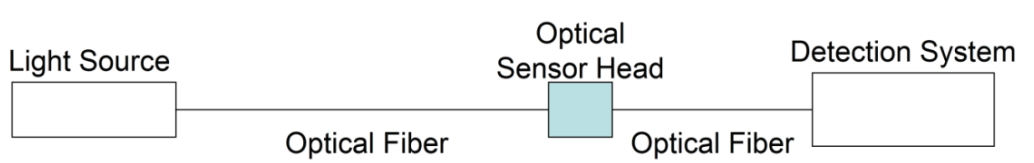
Sensing plays an important role in many applications using equipment that experiences degradation over time due to external forces or environmental factors. For example, civil structures experience degradation by being exposed to rain and to changing temperature. Moreover, these factors combined with exposure to external forces lead to cracks that can cause failure. Therefore, to avoid damage, it is important to detect and replace the equipment that experiences a certain amount of degradation, which in many cases can be considered dangerous. In this context, it is important to have sensors capable to detect changes in the physical or in the chemical composition of structures accurately. With the advent of fiber optic communications, it has been observed that using a dielectric medium to guide information in the form of light is more efficient than using metallic media to transmit electrical signals. Besides their excellent transmission characteristics, optical fiber sensors are attractive because they show the ability to confine the signal so that no electro-magnetic interference is experienced—a common issue encountered when using electrical signals: their operation requires electro-magnetic isolation and thus adds complexity to the detection system. Moreover, optical fibers are light and compact, which makes them useful in remote sensing and allows for packaging flexibility.

1.2 Characteristics of Fiber Optic Sensor Systems

A sensing system is built using the components shown in Figure 1.1. As observed, signal de-multiplexing can be achieved either in transmission or in reflection mode, as in Figure 1.1 a) and b), respectively. The light source is either broadband or pulsed, depending on the type of signal the sensor head is designed to process [1.1]. The optical sensor head responds to changes in environmental conditions by modulating the signal characteristics; these can then be detected using a photo-detector or an optical instrument that is able to measure the signal characteristic that has been modified; this change can be reflected in the wavelength, power, polarization, or phase of the optical signal. The detection system can be improved by processing the signal to get the accurate

measurement of the parameter the information is encoded into. The performance of a sensor system is determined by the extent to which, following calibration, a unique processed value corresponds to a particular environmental condition. Moreover, the sensitivity of the sensor and its measurement range play equally important roles. The former is defined by the change in the detected signal per unit of environmental condition change, while the latter defines the number of values that the system is able to accurately measure. In most applications, the sensors are used in real time, and the response time becomes an important parameter in evaluating the accuracy of the sensing system [1.1].

a)



b)

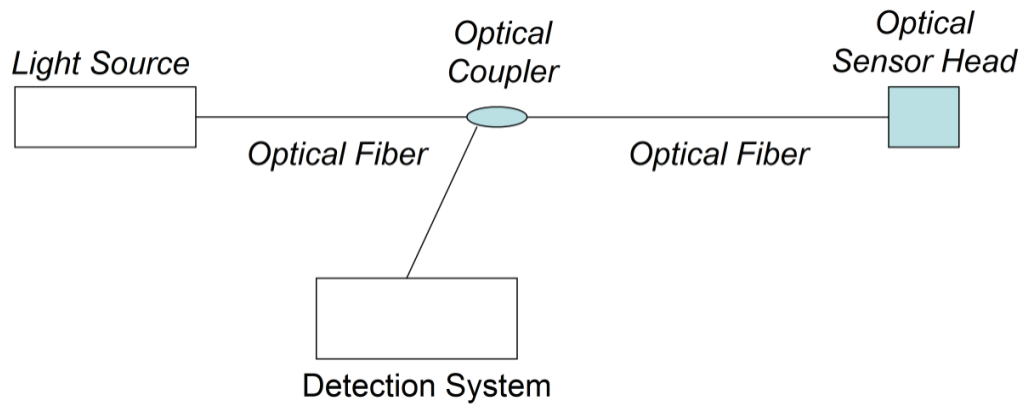


Figure 1.1: Fiber optic sensing system: a) transmission mode; b) reflection mode.

1.3 Types of Fiber Optic Sensors

Extensive studies show that optical fibers are sensitive to changes in external environmental parameters such as temperature, strain, and pressure. The former induces a change in refractive index which affects the guiding properties of the optical fibers. Strain and pressure affect the geometry of the fiber and thus induce changes in the effective refractive index, which characterizes the propagation mode area and losses.

These characteristics are reflected in the intensity or in the spectral characteristics of the optical signal detected at the output of the fiber: external factors modulate either the

light's amplitude or wavelength [1.2]. Moreover, progress in the field of fiber interferometers allows translating changes in phase or in spectral characteristics to changes in signal intensity. This approach extends the range of applications and the ability to tailor the sensing characteristics. Another classification of fiber optic sensor is based on whether the sensing region is lumped at the sensing location—point sensor—or it is distributed along the length of the fiber—distributed sensing [1.1]. The latter takes advantage of and explores techniques based on stimulated Brillouin scattering, stimulated Raman scattering, or optical time-domain spectrometers [1.3].

1.4 Fiber Bragg Grating (FBG) Sensors

FBGs can be used as point sensors because they are built by writing periodic structures resulting from the modulation of optical fibers' core refractive index over a short fiber length. Their spectral characteristics replicate the changes imposed on the effective refractive index resulting by the exposure to changing strain and temperature. In particular, FBGs reflect a narrow band of wavelengths centered about the Bragg (resonance) wavelength, which shifts in response to the aforementioned environmental factors. As a result, many applications aimed at monitoring strain and temperature changes have been explored and find practical use [1.4]. Of particular interest is the application of FBG sensors to structural health monitoring [1.5][1.6]. In this context, R. Maaskant *et al.* discuss the application of surface attached FBGs to monitoring the condition of different materials-based pre-stressed tendons, which are embedded in concrete girders, used in the structure of the Beddington Trail Bridge in Calgary, (Alberta, Canada) [1.5]. In the study, the strain monitoring helped researchers to identify the long-term behaviour of different materials and the effectiveness of using a newly proposed material— Carbon Fiber Composite Cable (CFCC). Other practical applications to civil structures have been used in monitoring the condition of Horsetail Falls Bridge in Oregon. In this case, the strains from twenty-six FBGs were successfully measured [1.7][1.8]. Saouma *et al.* have succeeded at applying FBG-based strain measurement to evaluate the properties of aluminum as a composite material for civil structures [1.7][1.9]. In another study, H.L. Ho *et al.* propose an FBG-based sensing system capable of detecting the static and dynamic responses of strain and temperature as applied to

studying the heat transfer properties of non-stationary flow and the induced vibrations. The static detection system involves using a scanning tuneable filter whose wavelength is tuned to the Bragg wavelength of the sensing FBGs and is placed before detecting the reflection spectrum of the grating. After the static measurement is completed, the dynamic measurement is achieved by setting the tuneable filter center wavelength to a wavelength where the slope of the FBG reflection spectrum is maximum—a point where the dynamic measurement is the most sensitive. Therefore, as dynamic strain is applied to the system is detected from a change in the voltage signal detected at the output of the tuneable filter [1.10]. The same principle can be also used to aerospace and civil applications, to determine the properties of composite materials, and to monitor the effect of static and dynamic load on electric transmission lines. An example of using a tuneable filter based detection system is provided by V.M. Murukeshan *et al.* in [1.11]. In this case, the sensor is used to monitor the cure process of composite materials, and is based on embedded FBG sensors. Temperature measurements have also been achieved using FBG sensors. For example, for application to civil structures, FBG temperature sensors are packaged to achieve isolation from strain and pressure effects [1.12].

Moreover, other parameters that are related to temperature or strain can be monitored. For example, to build a hydrophone, sound waves have the same effect strain has on FBGs, i.e., it causes a physical change in the length of the grating, and, consequently, its pitch. As a result of this phenomenon, the reflection wavelength shifts as it would under the effect of strain, with the difference that, in terms of sensitivity, sound waves have the same effect as pressure [1.13]. Recently, Y.-L. Park *et al.* propose embedding FBGs in robot component structures to measure contact or grasping forces. This parameter is measured using the information provided by changes in strain as forces are applied to FBGs [1.14]. Furthermore, as presented by F. Xie *et al.*, a Michelson interferometer built using FBGs can be used to measure displacement. Here, the property that FBGs are sensitive to temperature is used to compensate for environmental changes and thus measure the desired parameter—displacement—only [1.15]. Another application would be creating an acceleration sensor whose information can be converted to FBG strain changes, as proposed by J. Chang *et al* in [1.16].

1.5 Motivation and Thesis Contributions

Today, knowledge on the propagation and physical characteristics of optical fibers has led to the emergence of a number of applications. Even though sensing using FBG technology is mature enough to provide the necessary tools to generate, to transmit, and to modulate light in response to desired external parameters, the detection unit performance is limited by the propagation properties in guiding media. Specific limitations include the following:

- Power efficiency is limited by the losses incurred by the propagation distance, which is relatively long in most applications, especially remote sensing.
- The decoding method deployed usually involves using expensive, often bulky, and thus unpractical, instrumentation.
- Finally, multiplexing enhances the complexity of detection systems.

This thesis is aimed at providing simplified and less expensive solutions to decoding the information provided by two different designs of FBG-based sensors. First, chapter two introduces the theory behind light propagation in such structures. The chapters that follow provide solutions to the aforementioned problems that prevent the practical use of FBG sensors. Chapter 3 provides the characterization of a currently deployed vibration sensing system design. Next, in Chapter 4, the possibility to map this sensor's spectral information to microwave photonic filter variation to measure temperature is experimentally proven. Finally, previous studies show that using wavelength to power mapping using edge filters can simplify the method used to measure the changes induced when axial strain is applied to FBGs: instead of using an optical spectrum analyzer to measure wavelength change, a power meter, which is cheaper and less bulky, can be used to measure change in power. However, insertion losses are associated to both FBGs and filters, and, as a result, the simplified detection method comes at the expense of high transmission powers because this type of sensors find use in sensing over long distances. Therefore, Chapter 5 of this thesis proves the ability to combine the partial reflectivity and wavelength selectivity of FBGs in a fiber laser configuration to obtain improved mapping and enhanced power efficiency, which are associated to the lasing nature of the system. In this context, the performances of ring and of standing wave fiber laser

configurations will be compared and discussed. Performance will be evaluated in terms of the ability to achieve lasing at all FBGs in the sensor array and in terms of measurement sensitivity and power efficiency. In this context, the received power needs to be enhanced by at least 20 dB to satisfy the improved measurement capability over long distances. Moreover, the ability to use different sources and fiber laser gain media will be investigated for the purpose of reducing the overall system cost.

The studies that are presented in this thesis can also be found in the following publications:

- M.-I. Comanici and L. R. Chen, "Improved arrayed waveguide grating-based interrogation system for fiber Bragg grating sensors," *14th OptoElectronics and Communications Conference (OECC)*, 13-17 July 2009, Hong Kong, paper WQ3.
- P. Kung, M.-I. Comanici, and L.R. Chen, "Fiber Bragg grating vibration sensors for condition monitoring of hydro-electric turbine windings," *Photons*, vol.7 no. 2, 2009.
- M.-I. Comanici, L. R. Chen, and P. Kung, "Interrogating fiber Bragg grating sensors based on single bandpass microwave photonic filtering," *International Topical Meeting on Microwave Photonics*, 5 - 9 October 2010, Montreal, QC, paper FRI-5.

1.6 References

- [1.1] W. Boyes, Instrumentation Reference Book, pp. 191-216, Ed. 4, Butterworth-Heinemann: Burlington, MA, 2010.
- [1.2] E. Udd, “Overview of Fiber Optic Sensors” in Fiber Optic Sensors, edited by S. Yin, and P. B. Ruffin, F. T. S. Yu, ed. 2, pp. 1-34, CRC Press: Boca Raton, FL, 2008.
- [1.3] A. Bueno, K. Nonaka, and S. Sales, “Hybrid interrogation system for distributed fiber strain sensors and point temperature sensors based on pulse correlation and FBGs,” *IEEE Photonics Technology Letters*, vol. 21, no. 22, pp. 1671-1673, 2009.
- [1.4] A. Othonos, “Fiber Bragg gratings,” *Review of Scientific Instruments*, vol. 68, no. 12, pp. 4309-4341, 1997.
- [1.5] R. Maaskant, T. Alavie, R. M. Measures, G. Tadroq, S. H. Rizkalla, and A. Guha-Thakurta, “Fiber-optic Bragg grating sensors for bridge monitoring,” *Cement and Concrete Composites*, vol. 19, pp. 21-33, 1997.
- [1.6] C. K. Y. Leung, “Fiber optic sensors in concrete: the future?,” *NDT&E International*, vol. 34, pp. 85–94, 2001.
- [1.7] M. Majumder, T. K. Gangopadhyay, A. K. Chakraborty, K. Dasgupta, and D. K. Bhattacharya, “Fibre Bragg gratings in structural health monitoring—Present status and applications,” *Sensors and Actuators A*, vol. 147, pp. 150–164, 2008.
- [1.8] W. L. Schulz, J. P. Conte, E. Udd, and J. M. Seim, “Static and dynamic testing of bridges and highways using long-gage fibre Bragg grating based strain sensors,” *Proceedings SPIE*, vol. 4202, pp. 79-86, 2000.
- [1.9] V. E. Saouma, D. Z. Anderson, K. Ostrander, B. Lee, and V. Slowik, “Application of fibre Bragg grating in local and remote infrastructure health monitoring,” *Materials Structure*, vol. 31, pp. 259–266, 1998.
- [1.10] H. L. Ho, W. Jin, C. C. Chan, Y. Zhou, and X. W. Wang, “A fiber Bragg grating sensor for static and dynamic measurands,” *Sensors and Actuators A*, vol. 96, pp. 21-24, 2002.
- [1.11] V. M. Murukeshan, P. Y. Chan, L. S. Ong, and L. K. Seah, “Cure monitoring of smart composites using fiber Bragg grating based embedded sensors,” *Sensors and Actuators*, vol. 79, pp. 153–161, 2000.
- [1.12] P. Moyo, J. M. W. Brownjohn, R. Suresh, and S. C. Tjin, “Development of fiber Bragg grating sensors for monitoring civil infrastructure,” *Engineering Structures*, vol. 27, pp. 1828–1834, 2005.

- [1.13] N. Takahashi, K. Yoshimura, S. Takahashi, and K. Imamura, "Development of an optical fiber hydrophone with fiber Bragg grating," *Ultrasonics*, vol. 38, pp. 581–585, 2000.
- [1.14] Y. Park, K. Chau, R. J. Black, and M. R. Cutkosky, "Force sensing robot fingers using embedded fiber Bragg grating sensors and shape deposition manufacturing," *2007 IEEE International Conference on Robotics and Automation Roma*, Italy, 10-14 April 2007.
- [1.15] F. Xie, X. Chen, and L. Zhang, "High stability interleaved fiber Michelson interferometer for on-line precision displacement measurements," *Optics and Lasers in Engineering*, vol. 47, pp. 1301-1306, 2009.
- [1.16] J. Chang, Q. Wang, X. Zhang, D. Huo, L. Ma, X. Liu, T. Liu, and C. Wang, "A fiber Bragg grating acceleration sensor interrogated by a DFB laser diode," *Laser Physics*, vol. 19, no. 1, pp. 134-137, 2009.

2. Fiber Bragg Gratings Background

2.1 Introduction

With the advent of optical communications, optical fiber plays an important role in signal transmission. Also, work has been invested in fabricating in-fiber devices capable of tailoring the properties of light so optical fibers can be used to perform other tasks, which usually are accomplished by electronic devices and thus involve conversion losses and limit the system's speed. One such in-fiber structure is the FBG, whose properties were investigated after the discovery of photosensitivity: by doping the core of a single mode optical fiber with certain compounds, ultraviolet (UV) radiation can be absorbed and thus induce a permanent refractive index change [2.1]. Different methods are used in combination with the photosensitivity effect to obtain the periodic modulation of the core refractive index, which is able, through partial reflection at each high-low and low-high refractive index change, to reconstruct a reflected signal whose spectrum is centered at a wavelength that satisfies the Bragg condition: $\lambda_B = 2n\Lambda$, where Λ is the pitch of the periodically modulated core refractive index, and n is the effective refractive index [2.2]. The structure of an FBG and its spectral characteristics are shown in Figure 2.1.

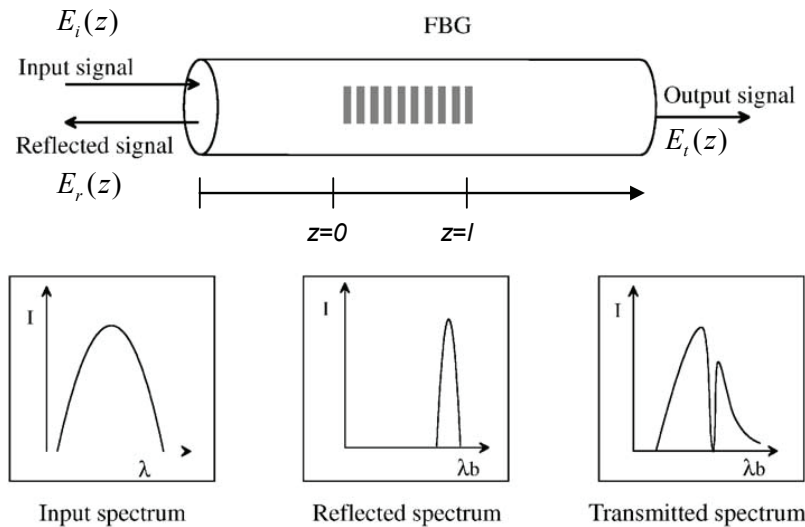


Figure 2.1: Schematic for the coupling between the wave reflected off the FBG and the input wave [2.8].

This chapter first describes the principle behind the writing of FBGs in the core of optical fibers. This is followed by the presentation of the coupled mode theory behind the

operation of FBGs. Next, the principles behind the effect of two environmental and physical factors, i.e., temperature and strain, are presented, followed by a discussion on the methods used to measure and discriminate these parameters.

2.2 Principles Behind FBGs Fabrication

The photosensitivity effect was first observed in highly Ge doped fiber. However, other methods to increase photosensitivity in single mode fibers usually used in telecommunications include hydrogenation (hydrogen loading), flame brushing, and boron co-doping. Hydrogenation is achieved because, under conditions of high pressure and high temperature, hydrogen diffuses into the Ge-Si core. This method is not permanent, so as the hydrogen concentration decreases, the strength of the photosensitivity effect decreases. The next method is flame brushing and involves hydrogen diffusion into the fiber core under very high temperatures (up to 1700° C). [2.3] This is achieved by repeatedly (and for short periods of time) exposing the region to be photosensitized to a hydrogen-rich flame. The high temperature causes the hydrogen diffusion. The major problem encountered when using high temperatures is the possibility of damaging the fiber. While the aforementioned methods increase photosensitivity through the formation of germanium-oxygen deficiency centers, boron co-doping helps to enhance photosensitivity through photo-induced stress relaxation, which affects the thermo-mechanical interaction between the boron doped core and the silica cladding. This implies the accumulation of thermo-elastic stress in the core [2.3].

In the writing process, the properties of FBGs depend on the wavelength of the ultraviolet light for photosensitivity and on the inscription method for the refractive index distribution, which sets the resonance reflected wavelength. There are two methods of writing FBGs into the core of an optical fiber: holographic and non-interferometric [2.1]. Holographic inscription uses interfering UV light to create the periodic pattern induced by the photosensitive effect. A first mechanism (illustrated in Figure 2.2) to create the interference would be to split an incoming radiation into two separate beams that experience different optical path lengths. However, since these paths are sensitive to external environmental conditions, this technique needs to be applied in a controlled environment to avoid FBG inscription errors.

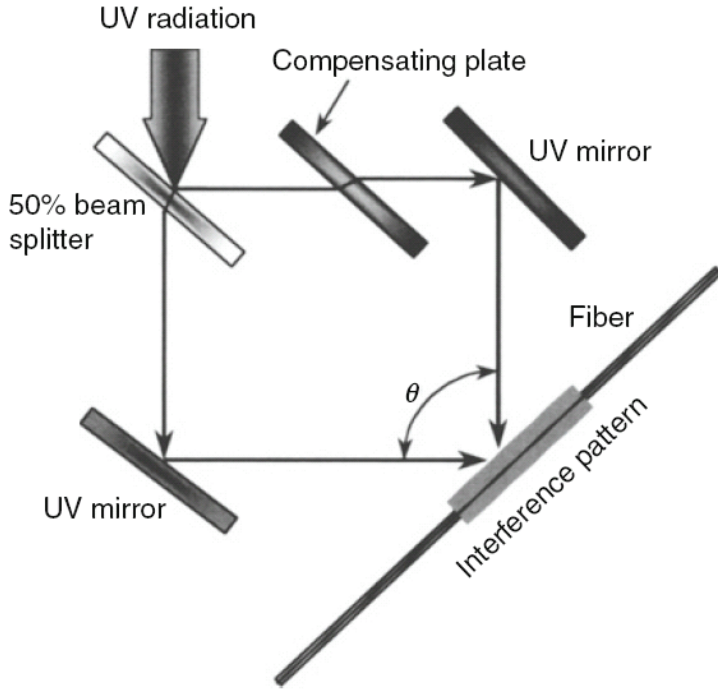


Figure 2.2: Interferometric method of writing FBGs in optical fiber's core [2.1].

An alternative that is widely used involves using a phase mask, which is a diffractive optical element (DOE) aimed at spatially modulating the UV beam (see Figure 2.3) [2.1]. This technique achieves the modulation of the core refractive index by creating an interference pattern between the +1 and -1 orders of the diffraction mask. Note that it is important to suppress the 0th order to achieve proper interference between the first order modes; this is achieved by tailoring the mask's grating corrugations depth, and the process is dependent on the wavelength of the incident UV beam. The refractive index modulation pitch of the FBG $\Lambda_{Bragg_grating}$ only depends on the DOE's period Λ_{DOE} , i.e.,

$\Lambda_{Bragg_grating} = \frac{\Lambda_{DOE}}{2}$. Therefore, the phase mask method allows improving the fabrication cost, reliability and repeatability. [2.4]

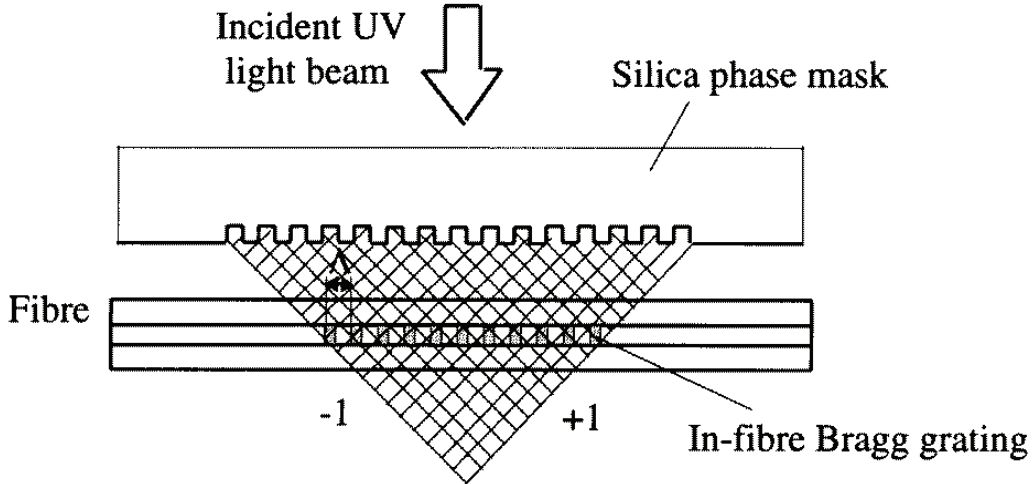


Figure 2.3: Phase-mask (diffraction based) FBG writing method [2.6].

2.3 Coupling Properties of FBGs

FBGs are written in the guiding region of a single mode fiber, and their refractive index varies sinusoidally according to the equation $n(z) = n_0 + n_1 \cos(Kz)$, where z is the spatial direction of propagation, n_0 is the average refractive index, n_1 is the refractive index modulation depth, and K is a constant that is related to the pitch of the grating (Λ) by the equation $K = \frac{2\pi}{\Lambda}$ [2.5]. FBGs act as reflectors when coupling between the forward and the backward propagating waves is achieved, i.e., power is transferred between the forward and counter-propagating waves of the same mode. [2.5][2.7-2.8] When coupling between the forward core mode and the forward cladding mode occurs, the power that is coupled for transmission is lost in the cladding mode for a narrow band of wavelengths. This phenomenon is observed in long period gratings, which act as transmission mode filtering components with no reflected power [2.9-2.11].

For the case when the Bragg grating is uniform, the forward $E_f(z)$ and backward $E_r(z)$ waves propagating through a FBG are described by the following coupling equations:

$$\frac{dE_i(z)}{dz} = -j\kappa E_r(z)e^{-j2\delta z} \quad (2.1)$$

$$\frac{dE_r(z)}{dz} = j\kappa E_i(z)e^{j2\delta z} \quad (2.2)$$

In Equations (2.1) and (2.2), κ is the coupling constant, and δ characterizes the phase matching condition [2.5][2.8]. The latter is defined by the following relation:

$$\delta = \frac{1}{2}(2\beta - K) = 2\pi n_{eff} \left(\frac{1}{\lambda} - \frac{1}{\lambda_B} \right),$$

where the parameters β , K , n_{eff} , λ , and λ_B are the

magnitude of the propagation vector, the magnitude of the grating vector as defined earlier, the effective refractive index, the operation wavelength, and the Bragg wavelength, respectively [2.8].

Using the transfer matrix theory presented by T. Erdogan in [2.7], and denoting the length of the FBG as l , the following relationship between the input at $z=0$ and the output at $z=l$ electric fields is the following:

$$\begin{bmatrix} E_i(0) \\ E_r(0) \end{bmatrix} = [T] \begin{bmatrix} E_i(l) \\ 0 \end{bmatrix}, \text{ with } T = \begin{pmatrix} \cosh(\alpha l) - \frac{j\delta \sinh(\alpha l)}{\alpha} & -j \frac{\kappa \sinh(\alpha l)}{\alpha} \\ j \frac{\kappa \sinh(\alpha l)}{\alpha} & \cosh(\alpha l) - \frac{j\delta \sinh(\alpha l)}{\alpha} \end{pmatrix} \quad (2.3)$$

where $\alpha = \sqrt{|\kappa|^2 - \delta^2}$ and $\kappa = \frac{\pi n_{eff} \Gamma}{\lambda}$. The newly introduced parameter Γ represents the fraction of the input power that is confined to the core of the fiber grating (confinement factor) [2.8]. Note that it is assumed that there is no input from the right of the fiber as referenced by Figure 2.1, i.e., $E_r(l) = 0$.

The transfer function is useful to find the reflectance of the FBG as a function of the operation wavelength, which is given as

$$R(\lambda) = \left| \frac{E_r(0)}{E_i(0)} \right|^2 = \left| \frac{T_{21}(\lambda)}{T_{11}(\lambda)} \right|^2 = \frac{\kappa^2 \sinh^2(\alpha l)}{\alpha^2 \cosh^2(\alpha l) + \delta^2 \sinh^2(\alpha l)} \quad (2.4)$$

Owing to their wavelength dependent characteristics, uniform FBGs have been extensively used as filter and WDM components, which take advantage of the ability of such periodic structures to reflect a narrowband of wavelengths [2.13]. Many applications require the characteristics of the grating to be tailored so as to achieve certain functions.

In this context, sometimes it is desirable to have non-uniform gratings. For example, FBGs characterized by non-uniform periodicity can be applied to long distance systems because they offer the possibility to tailor the width of optical pulses, and can be applied to dispersion compensation [2.13][2.16]. When the periodicity of the grating changes with distance along its length, the grating is said to be chirped; when the refractive modulated index varies with propagation distance, the FBG is said to be apodized [2.14]. In the case when non-uniform gratings are used, the reflection characteristics of the gratings can be calculated by dividing the grating into segments each of which can be treated a uniform grating over a small distance. Therefore, each segment can be characterized by its own transmission matrix. This way, the signal that is output from the left to the $(j+1)$ th segment is the transmitted signal from the j th grating segment, and the wave that is reflected by the $(j+1)$ th segment, is the input from the right to the j th segment. Mathematically, this can be represented as follows:

$$\begin{bmatrix} E_i(0) \\ E_r(0) \end{bmatrix} = [T_1][T_2][T_3] \dots [T_N] \begin{bmatrix} E_i(l) \\ 0 \end{bmatrix} \quad (2.5)$$

where N is the number of segments along the length of the FBG [2.15].

2.3.1 Non-uniform FBGs Used as Sensors

Recently, different types of non-uniform FBGs find application to sensing. For example, in [2.17] Y. Okabe *et al.* proposed using the capability of chirped FBGs to detect cracks along the length of a structure. This relies on the change in the chirped FBG spectrum owing to the tensile load imposed by cracks. The same characteristics of chirped FBGs were used in [2.18] by D. Inaudi *et al.* to detect damage caused to carbon fiber reinforced plastic. Moreover, there are novel structures such as tilted FBGs, characterized by a tilt in the index modulation pattern relatively to the propagation axis of the optical fiber. The spectral characteristic of tilted FBGs is the presence of a large number of resonances centered on the Bragg wavelength in the transmission spectrum. Since the response of such structures also depends on the cladding modes, it can be used to measure refractive index [2.19]. In general, FBG sensing relies on the sensitivity to strain and temperature to achieve the measurement of different parameters. Over the past years, the sensitivity to temperature and to strain of FBGs has been used as tuning

parameters in optical filtering [2.20]. Recently, these properties have shown potential and practical use in fiber optic sensing. However, strain and temperature have a similar effect on the spectra of FBGs, and, as a result, interrogation systems have to be designed to discriminate the desired parameter, irrespective of the effect the other has on the measurement.

2.4 Strain and Temperature Effect on FBGs

As discussed earlier, the Bragg wavelength of an FBG depends on both the effective refractive index, and on the pitch of the periodic structure. The change in the resonance wavelength of the FBG due to changes in temperature and applied strain is given in the following equation:

$$\Delta\lambda_{Bragg} = 2 \left[A \frac{\partial n_{eff}}{\partial l} + n_{eff} \frac{\partial A}{\partial l} \right] \Delta l + 2 \left[A \frac{\partial n_{eff}}{\partial T} + n_{eff} \frac{\partial A}{\partial T} \right] \Delta T \quad (2.6)$$

where, n_{eff} , A , Δl , and ΔT are the effective refractive index of the FBG, its period, the change in length due to longitudinal strain, and the change in temperature, respectively [2.10].

2.4.1 Strain Effect on FBGs

In Equation (2.6), the first term in brackets describes the effect strain has on the FBG, i.e., a change in length owing to tension induces a change in the grating pitch, and a change in refractive index as a result of the strain optic effect [2.10]. Therefore, the strain dependent term can be expressed as $\Delta\lambda_{Bragg, strain} = \lambda_{Bragg,0} (1 - P_{\alpha}^{eff}) \varepsilon$ [2.21], where P_{α}^{eff} is the index-weighted strain optic coefficient at a certain temperature, denoted by the alpha in the subscript, and ε is the applied strain, which is defined as $\Delta l / l$ [2.10]. Note the zero in the subscript of the Bragg wavelength expresses the resonance reflection wavelength when no strain is applied to the FBG. The strain optic coefficient has the components as defined by $P_{\alpha}^{eff} = \frac{n_{eff}^2}{2} [p_{12} - \nu(p_{11} + p_{12})]$ [2.10], where p_{12} and p_{11} are the strain-optic tensors, which are characteristic of the glass materials [2.22-2.24], and ν is the Poisson's

ratio [2.1][2.24-2.25]. The typical value for the effective strain optic coefficient in silica glass is 0.22 [2.26].

2.4.2 Temperature Effect on FBGs

The second term in Equation (2.6) accounts for the temperature effect on the resonance frequency of an FBG, which can be expressed as

$$\Delta\lambda_{Bragg,temp} = \lambda_{Bragg,0}(\alpha_A + \alpha_n)\Delta T, \text{ with } \alpha_A = \left(\frac{1}{A}\right)\left(\frac{\partial A}{\partial T}\right)$$

as the thermal expansion coefficient and with $\alpha_n = \left(\frac{1}{n}\right)\left(\frac{\partial n}{\partial T}\right)$ as the thermo-optic coefficient [2.9][2.26-2.27]; they

have values of $0.55 \times 10^{-6} K^{-1}$ and $8.0 \times 10^{-6} K^{-1}$, respectively [2.26].

2.4.3 FBG Temperature and Strain Sensors Interrogation

As shown in Figure 2.4, the simplest interrogation system for the wavelength encoded FBG based sensors involves the use of an optical spectrum analyzer to detect the change in wavelength with changing either temperature or strain. However, this is not practical because OSAs are expensive and experience low wavelength scanning speed [2.29].

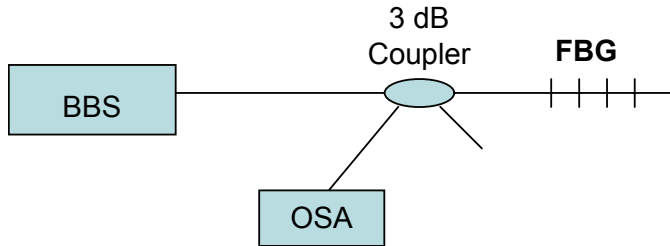


Figure 2.4: OSA based interrogation system for FBG strain or temperature sensors.

To avoid using expensive instrumentation to measure the response of FBGs due to changing strain or temperature, a number of passive or active detection schemes have been used [2.29]. For example, devices whose spectrum power level changes with wavelength can be used as filtering elements capable of associating a power level to each shift in wavelength. This method is presented by Q. Wang *et al.* in [2.30] and by G. Lloyd *et al.* in [2.31], and its schematic is shown in Figure 2.5. In this case, the input signal is the reflection spectrum from the FBG under test. As a result, the ratio of the

detected signal at a certain wavelength λ_0 is given by

$$R(\lambda_0) = -10 \log_{10} \left[\frac{\int I_{\lambda_0}(\lambda) T_f(\lambda) d\lambda}{\int I_{\lambda_0}(\lambda) d\lambda} \right],$$

where $I_{\lambda_0}(\lambda)$ and $T_f(\lambda)$ are the spectral response

of the input signal and the spectral transmission response of the edge filter, which experiences an increasing or a decreasing variation in power with increasing wavelength [2.29]. This method can be used to account for the power fluctuation in the incoming light while passing through the system, i.e., a change in the total incident power is reflected in the power of the FBG's reflection spectrum. Therefore, the ratio of the latter to the former cancels out the undesirable power fluctuation. Among the edge filters that have been previously used include long period FBGs, which, as mentioned earlier, experience a filtering response in transmission mode, ramp filters [2.30], thin film filters [2.32], interference filters [2.33], Sagnac loop filters [2.34], single-multiple-single-mode (SMS) fiber filters [2.35], and AWGs [2.36].

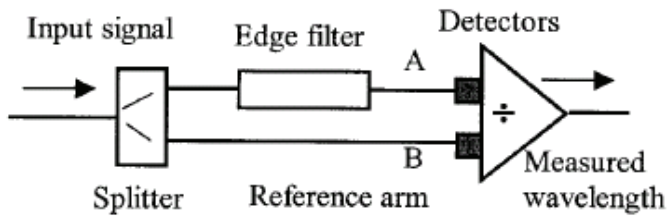


Figure 2.5: Passive interrogation system for FBGs [2.30].

Other interrogation systems include active elements to measure the response of FBGs. For example, tuneable filters were used as wavelength selective elements to measure the shift in the Bragg wavelength as temperature or strain conditions change [2.29]. Other active methods involve using interference based detection systems. For example, in [2.37] Kersey *et al.* propose a Mach-Zehnder interferometer based fiber interrogation system able to achieve relatively large measurement resolution.

2.4.4 Temperature Independent Strain Sensing

When using the detection systems presented in the previous section, in practice it is important to be able to measure strain independently of changes in temperature. As discussed, the two affect the spectrum of the FBG in a similar manner. A straightforward method, as proposed by Y.-J. Chiang *et al.* in [2.38] involves using a pair of FBGs, both susceptible to temperature effect, with one of them being protected from strain. In this case, it is desirable that both FBGs experience the same sensitivity to temperature so its effect can be isolated from the strain effect. Another method involves using nonlinear effects such as stimulated Brillouin scattering to discriminate temperature from strain measurements [2.39]. Furthermore, it has been proposed that using LPGs with known temperature responses can help to only measure strain. This approach, however, suffers from longer physical length, LPGs and FBGs show different sensitivities to bends, and LPGs experience relatively large bandwidths, which imposes a limit on the measurement accuracy and on the number of sensors that can be multiplexed [2.40]. Another strain-temperature discrimination system involves using different cladding FBGs, which experience different shifts in wavelength owing to temperature change. In this case, the FBGs can have different resonance wavelengths, and, thus, their response can be measured using wavelength division multiplexing. One problem with this approach is that there are issues related to the need for splicing, with splicing strength limiting the measurement accuracy [2.41]. As in [2.42], interference based methods use an unbalanced Mach-Zehnder interferometer with two FBGs of different diameters to discriminate temperature from strain. Moreover, rare-earth components doped fiber can be used to achieve temperature and strain measurements independently. For example, in [2.43], J. Jung *et al.* propose writing an FBG in a length of *Er-Yb* doped fiber. This way, it is proven that the ASE power of the *Er-Yb* doped amplifier decreases monotonically with temperature. Therefore, a relationship can be found between the Bragg shift owing to strain, and the effect temperature has on the ASE of the amplifier. Moreover, the ability to obtain different signal properties for different polarization states can be used to achieve strain-temperature discrimination. For example, O. Haderler *et al.* propose using a distributed feedback grating fiber laser system with two polarizations and using two of their properties to measure the two environmental factors separately: polarization beat

frequency and the polarization absolute wavelength [2.44]. Recent work shows that it is possible to use novel fiber grating structures such as, for example, tilted FBGs, which was proposed by E. Chehura *et al.* in [2.45]. This method relies on the property that the core and the cladding have different responses to temperature, and the loss fringe pattern in the transmission spectrum of tilted FBGs depends on the coupling between the cladding and the core modes.

2.5 Summary

In this chapter, the theory behind FBGs, which is necessary to understand the properties that make these in-fiber structures useful for sensing, is provided. A first aspect involves understanding the fiber composition that allows using UV light to change the refractive index in a periodic fashion to achieve the narrowband reflection spectrum. Moreover, the fabrication methods that are most frequently used to inscribe FBGs in the core of an optical fiber are reviewed. These are in general chosen according to the quality of the writing process, and, in practical sensing systems design, gives an idea on the cost of fabricating the sensor components. Next, the coupled mode theory allows the designer to understand how different external or environmental factors influence the properties of the spectral component of a signal passing through an FBG. This discussion is followed by a presentation of the way the information provided by the signal modulated by the guiding structure has been used in different configurations to achieve the required parameter measurements more effectively. A review of past studies is included, which may help in the development of new and innovative sensing systems. Since both temperature and strain affect the same parameter of an FBG's reflection spectrum, detection systems able to differentiate between these so as to achieve the desired measurement are necessary. Therefore, it is mandatory to be familiar with the existing temperature-strain discrimination methods that can be used to achieve reliable measurement.

2.6 References

- [2.1] R. Kashyap, Fiber Bragg Gratings, ed. 2, pp. 53-118, 441-502, Academic Press: San Diego, California, 2010.
- [2.2] L. Zhang, W. Zhang, and I. Bennion, "In-Fiber Grating Optic Sensors" in Fiber Optic Sensors edited by S. Yin, P. B. Ruffin and F. T. S. Yu, ed. 2, CRC Press: Boca Raton, FL, 2008.
- [2.3] A. Othonos, "Fiber Bragg gratings," *Review of Scientific Instruments*, vol. 68, no. 12, pp. 4309-4341, 1997.
- [2.4] K. O. Hill and G. Meltz, "Fiber Bragg Grating Technology Fundamentals and Overview," *Journal of Lightwave Technology*, vol. 15, no. 8, pp. 1263-1276, 1997.
- [2.5] A. Yariv and P. Yeh, Photonics: optical electronics in modern communications, ed. 6, Oxford University Press: 2007.
- [2.6] Y.-J. Rao, "In-fibre Bragg grating sensors," *Measurement Science Technology*, vol. 8, pp. 355-375, 1997.
- [2.7] T. Erdogan, "Fiber grating spectra," *Journal of Lightwave Technology*, vol.15, no. 8, pp. 1277-1294, 1997.
- [2.8] A. M. Abdi, S. Suzuki, A. Schülzgen, and A. R. Kost, "Modeling, design, fabrication, and testing of a fiber Bragg grating strain sensor array," *Applied Optics*, vol. 46, no. 14, pp 2563-2574, 2007.
- [2.9] V. Bhatia and A. M. Vengsarkar, "Optical fiber long-period grating sensors," *Optics Letters*, vol. 21, no. 9, pp. 692-,1996.
- [2.10] S. W. James and R. P. Tatam, "Optical fibre long-period grating sensors: characteristics and application," *Measurement Science and Technology*, vol. 14, pp. R49-R61, 2003.
- [2.11] V. Bhatia, D. Campbell, and R.O. Claus, "Simultaneous strain and temperature measurement with long-period gratings," *Optics Letters*, vol. 22, no. 9, pp. 648-650, 1997.
- [2.12] P. Ferraro and G. De Natale, "On the possible use of optical fiber Bragg gratings as strain sensors for geodynamical monitoring," *Optics and Lasers in Engineering*, vol. 37, pp. 115-130, 2002.
- [2.13] A. Othonos, K. Kalli, D Pureur, and A. Mugnier, "Fibre Bragg Gratings" in Wavelength Filters in Fibre Optics, edited by H. Venghaus, pp. 189-269, Springer Series: Berlin, 2006.

- [2.14] C. Yang and Y. Lai, "Apodised fiber Bragg gratings fabricated with a uniform phase mask using Gaussian beam laser," *Optics and Laser Technology*, vol. 32, pp. 307-310, 2000.
- [2.15] S. Huang, M. LeBlanc, M. M. Ohn, and R. M. Measures, "Bragg intragrating structural sensing," *Applied Optics*, vol 34, no. 22, pp. 5003-5009, 1995.
- [2.16] X. Dong, B.-O. Guan, S. Yuan, X. Dong, and H.-Y. Tam, "Strain gradient chirp of uniform fiber Bragg grating without shift of central Bragg wavelength," *Optics Communications*, vol. 202, pp. 91-95, 2002.
- [2.17] Y. Okabe, R. Tsuji, and N. Takeda, "Application of chirped fiber Bragg grating sensors for identification of crack locations in composites," *Composites: Part A*, vol. 35, pp. 59-65, 2004.
- [2.18] N. Takeda, Y. Okabe, R. Tsuji, and S. Takeda, "Application of chirped fiber Bragg grating sensors for damage identification in composites," *Proceedings SPIE*, Vol. 4694, no. 106, 2002.
- [2.19] Y. Miao, B. Liu, and Q. Zhao "Refractive index sensor based on measuring the transmission power of tilted fiber Bragg grating," *Optical Fiber Technology*, vol. 15, pp. 233-236, 2009.
- [2.20] T. Inui, T. Komukai, and M. Nakazawa, "Highly efficient tunable fiber Bragg grating filters using multilayer piezoelectric transducers," *Optics Communications*, vol. 190, pp. 1-4, 2001.
- [2.21] C. Y. Wei, S. W. James, C. C. Ye, R. P. Tatam, and P. E. Irving, "Application issues using fibre Bragg gratings as strain sensors in fibre composites," *Strain*, vol. 36, no. 3, pp. 143-150, 2000.
- [2.22] N. F. Borrelli and R. A. Miller, "Determination of the individual strain-optic coefficients of glass by an ultrasonic technique," *Applied Optics*, vol. 7, no. 5, pp. 745-750, 1968.
- [2.23] L. Kang, D. Kim, and J. Han, "Estimation of dynamic structural displacements using fiber Bragg grating strain sensors," *Journal of Sound and Vibration*, vol. 305, pp. 534-542, 2007.
- [2.24] D.H. Kang, S.O. Park, C.S. Hong, and C.G. Kim, "The signal characteristics of reflected spectra of fiber Bragg grating sensors with strain gradients and grating lengths," *NDT & E International*, vol. 38, pp. 712-718, 2005.
- [2.25] S. Zhang, S.B. Lee, X. Fang, and S.S. Choi, "In-fiber grating sensors," *Optics and Lasers in Engineering*, vol. 32, pp. 405-418, 1999.

- [2.26] P.S. André, J.L. Pinto, I. Abe, H.J. Kalinowski, O. Frazão, and F.M. Araújo, “Fibre Bragg grating for telecommunications applications: tuneable thermally stress enhanced OADM,” *Journal of Microwaves and Optoelectronics*, vol 2, no. 3, pp. 32-45, 2001.
- [2.27] Y. Lo, Y. Lin, and Y. Chen, “Athermal fibre Bragg grating strain gauge with metal coating in measurement of thermal expansion coefficient,” *Sensors and Actuators A*, vol. 117, pp. 103–109, 2005.
- [2.28] P. Moyo, J.M.W. Brownjohn, R. Suresh, and S.C. Tjin, “Development of fiber Bragg grating sensors for monitoring civil Infrastructure,” *Engineering Structures*, vol. 27, pp. 1828–1834, 2005.
- [2.29] B. Lee, “Review of the present status of optical fiber sensors,” *Optical Fiber Technology*, vol. 9, pp. 57–79, 2003.
- [2.30] Q. Wang, G. Farrell, and T. Freir, “Study of transmission response of edge filters employed in wavelength measurements”, *Applied Optics*, vol. 44, no. 36, pp. 7789-7792, 2005.
- [2.31] G. Lloyd, L. Everall, K. Sugden, and I. Bennion, “Resonant cavity based fibre Bragg grating sensor interrogation using ratiometric detection,” *Optics Communications*, vol. 244, pp. 193–197, 2005.
- [2.32] Q. Wang, G. Rajan, G. Farrell, P.Wang, Y. Semenova, and T. Freir, “Macrobending fibre loss filter, ratiometric wavelength measurement and application,” *Measurement Science and Technology*, vol. 18, pp. 3082–3088, 2007.
- [2.33] L.N. Hadley and D.M. Dennison, “Reflection and transmission interference filters,” *Journal of the Optical Society of America*, vol. 37, no. 6, pp. 451-453, 1947.
- [2.34] D. Zhao, X. Shu, L. Zhang, and I. Bennion, “Sensor interrogation technique using chirped fibre grating based Sagnac loop,” *Electronics Letters*, vol. 38, no. 7, pp. 312-313, 2002.
- [2.35] Q. Wu, A.M. Hatta, Y. Semenova, and G. Farrell, “Use of a single-multiple-single-mode fiber filter for interrogating fiber Bragg grating strain sensors with dynamic temperature compensation,” *Applied Optics*, vol. 48, no. 29, pp. 5451-5458, 2009.
- [2.36] A. Hongo, S. Kojima, and S. Komatsuzaki, “Applications of fiber Bragg grating sensors and high-speed interrogation techniques,” *Structural Control Health Monitoring*, vol 12, pp. 269-282, 2005.

- [2.37] A. D. Kersey, T. A. Berkoff, and W. W. Morey, "High-resolution fibre-grating based strain sensor with interferometric wavelength-shift detection," *Electronics Letters*, vol. 28, no. 3, pp. 236-238, 1992.
- [2.38] Y.-J. Chiang, L. Wang, H. Chen, C. Yang, and W.-F. Liu, "Multipoint temperature-independent fiber-Bragg-grating strain-sensing system employing an optical-power-detection scheme," *Applied Optics*, vol. 41, no. 9, pp. 1661-1667, 2002.
- [2.39] M. N. Alahbabi, Y. T. Cho, and T. P. Newson, "Long-range distributed temperature and strain optical fibre sensor based on the coherent detection of spontaneous Brillouin scattering with in-line Raman amplification," *Measurement Science Technology*, vol. 17, pp. 1082-1090, 2006.
- [2.40] Y. Zhao and Y. Liao, "Discrimination methods and demodulation techniques for fiber Bragg grating sensors," *Optics and Lasers in Engineering*, vol. 41, pp. 1-18, 2004.
- [2.41] S.W. James, M.L. Dockney, and R.P. Tatam, "Independent measurement of temperature and strain using in fiber Bragg grating sensors," *Proceedings of the 11th International Conference on Optical Fiber Sensors*, Sapporo, Japan, post deadline paper: Fr3-3, 1996.
- [2.42] M. Song, B. Lee, S. B. Lee, and S.S. Choi, "Interferometric temperature-insensitive strain measurement with different-diameter fiber Bragg gratings," *Optics Letters*, vol. 22, no. 11, pp. 790-792, 1997.
- [2.43] J. Jung, N. Park, and B. Lee, "Simultaneous measurement of strain and temperature by use of a single fiber Bragg grating written in an erbium:ytterbium-doped fiber," *Applied Optics*, vol. 39, no. 7, pp. 1118-1120, 2000.
- [2.44] O. Hadeler, E. Ronnekleiv, M. Ibsen, and R.I. Laming, "Polarimetric distributed feedback fiber laser sensor for simultaneous strain and temperature measurements," *Applied Optics*, vol. 38, no. 10, pp. 1953-1958, 1999.
- [2.45] E. Chehura, S.W. James, and R.P. Tatam, "Temperature and strain discrimination using a single tilted fibre Bragg grating," *Optics Communications*, vol. 275, pp. 344-347, 2007.

3. Fiber Bragg Grating Vibration Sensors for Condition Monitoring

3.1 Introduction

Today the ability to perform condition monitoring finds prevalent use in industry. This includes applications that involve the necessity to assess the condition of certain hydro-electric generators' key components. Over time, hydro-electric turbine windings experience deterioration, resulting in an increase in vibration amplitude. If the amplitude of these vibrations increases above a certain threshold, fire and/or damage to the equipment and eventually to neighbouring components can occur. The possibility to monitor vibration amplitudes would allow for replacing the windings before they cause hazards. Since for such applications the working conditions involve high electric and magnetic fields, fiber optic sensors, which are immune to electromagnetic interference, are a suitable option. Because of their fiber optic nature, FBG sensors have found extensive use in applications that require strain and temperature monitoring primarily because they are immune to electromagnetic interference. Moreover, they are compact, light, low-cost, and they can be multiplexed along the same fiber [3.1]. Besides their ability to sense strain or temperature, FBGs can be used for vibration measurements. For example, a proposed method is to embed the FBG in a flexible structure and correlate its wavelength shift due to strain to the curvature of the surface as vibration is applied [3.2-3.4]. Another proposed design involves measuring vibration by inscribing the sensing FBGs onto tapered optical fiber. This imposes a chirp on the grating and any disturbance of the structure leads to a change in this chirp, which can be quantitatively related to vibration change [3.5]. Recently, QPS Photonics (Montreal, QC) has developed an interference based vibration sensor especially designed for vibration measurement in hydro-electric turbine windings that makes use of the FBG technology to measure vibration amplitude and frequency. The purpose of this chapter is primarily to characterize these sensors, which need to be operated at either 100 Hz or 120 Hz, i.e., at twice the wire line frequencies of 50 Hz and 60 Hz, respectively that typically are used [3.6]. Different sensor packages have been investigated to assess the impact they have on the sensor's vibration resonant frequencies, on the operability regions, and on the measured amplitude resolution that can be obtained. For design optimization purposes,

the different designs were evaluated in terms of measurement repeatability, which is correlated to the sensor reliability. Moreover, repeatability measurements are aimed at ensuring that the different sensor designs satisfy the sensing requirements. The chapter is organized as follows: first, the design and detection principle of the VibroFiberTM sensor is presented. This is followed by a presentation of the types of measurements performed on the vibration sensor, i.e. amplitude and frequency of vibration, which are illustrated through experimental results on different sensor packaging designs. The final section focuses on the power budget needed to achieve time division multiplexing (TDM) capabilities for FBG-based sensors. TDM is required to achieve lower cost sensing systems by increasing the number of sensors that can be monitored.

3.2 VibroFiberTM System Design

3.2.1 Operation Principle

As illustrated in Figure 3.1, the VibroFiberTM sensor head consists of two identical, low reflectivity FBGs written on the same single mode fiber and spaced by 5 mm to 20 mm [3.7]. This structure forms a low-finesse cavity, which is characterized by low reflectivity mirrors, which cause the interference signal spectrum to experience sinusoidal fringe variation [3.8]. For example, Figure 3.2 shows the calculated reflection response of two partial reflectors (e.g. FBGs) separated by 10 mm for different reflectivities. Note that at low reflectivities (7% and 17%) the variation is sinusoidal, and this is no longer observed high reflectivities (57% or 87%). As shown in Figure 3.3, the overall reflection spectrum of the VibroFiberTM consists of interference fringes within an envelope corresponding to the reflection spectra of the individual FBGs. The cavity modes are separated by the free spectral range (FSR) $\Delta\lambda = \frac{\lambda^2}{2nL}$, where λ is the center wavelength of the reflection spectrum, n is the effective mode index of the fiber, and L is the spatial separation between the FBGs, which changes in response to a vibration applied to the fiber. As a result, the FSR of the FBG sensor head also changes.

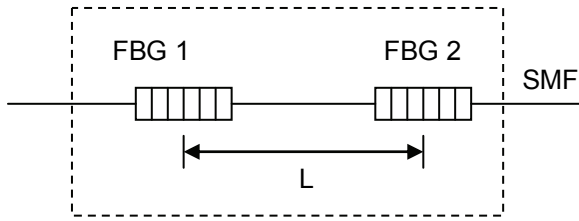


Figure 3.1: Schematic for the VibroFiber™ sensor head.

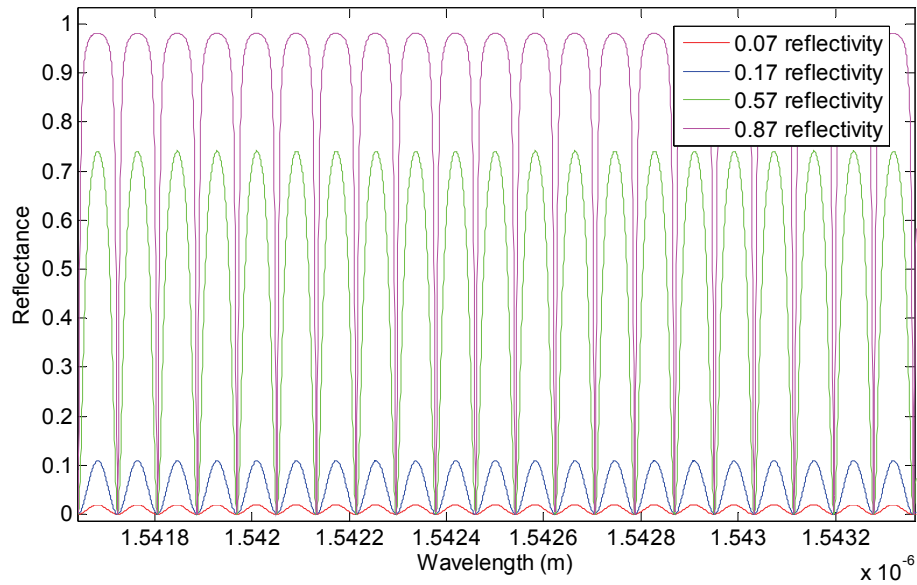


Figure 3.2: Fiber Fabry-Perot cavity reflection spectrum for different reflectivities of the interferometer reflectors.

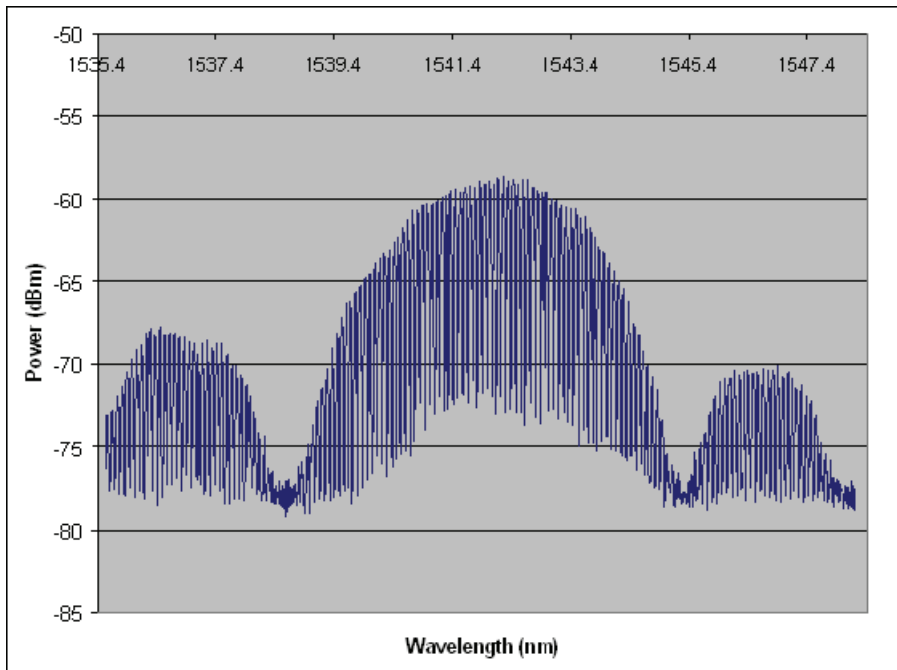


Figure 3.3: Reflection Spectrum for a VibroFiber™ sensor.

3.2.2 Sensor Packaging

A first design, package type A, involves placing the fiber end containing the FBG pair centered between two rectangular adhesive polyamide sheets, which affects the effect of vibration on the sensing structure. As such, the length and the width of the polyamide sheet influence sensing characteristics such as measurement repeatability and reliability, and vibration resonant frequency. The polyamide covered sensor head is placed inside a protection case, which is designed to protect the fiber from harsh environmental factors such as impact, or from dust and other particles in the air. Also, the package is designed to fit between the windings of the hydro-electric turbine: the package sides are flat and parallel to the rectangular polyamide sheet, as illustrated in Figure 3.4.

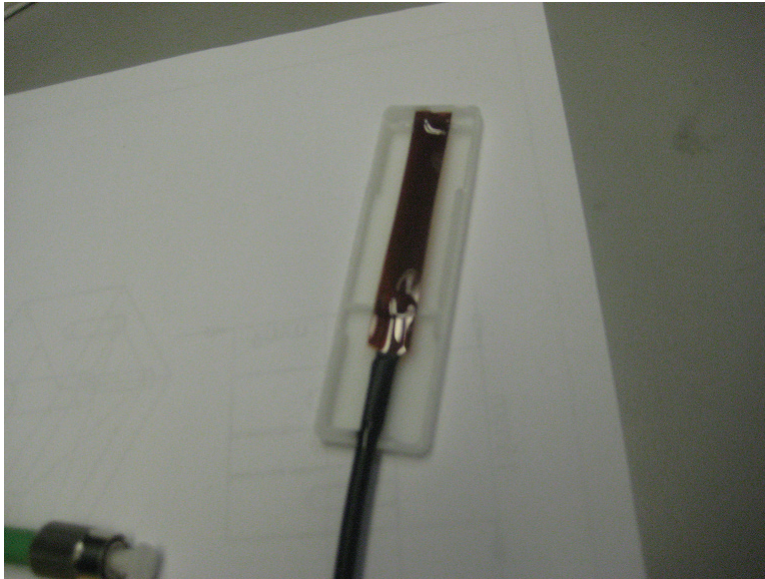


Figure 3.4: Sensor head placement inside the protection case.

The second design alternative, package type B, consists of replacing the polyamide sheet by two thin, rigid, plastic plates, each provided with a v-groove at its center so the fiber head can easily be placed so as to avoid axial pressure. As illustrated in Figure 3.5, a movable plastic piece is placed over the sensor head such that slight pressure can be applied at different locations along the length of the fiber sensor head. Depending on the distance from the FBG pair where the pressure is applied, different vibration resonance frequencies are obtained. The operability region can thus be tuned. For optimum vibration transmission, the sensor head thus formed is placed in the same casing as in the polyamide sheet covered FBG pair sensor head.

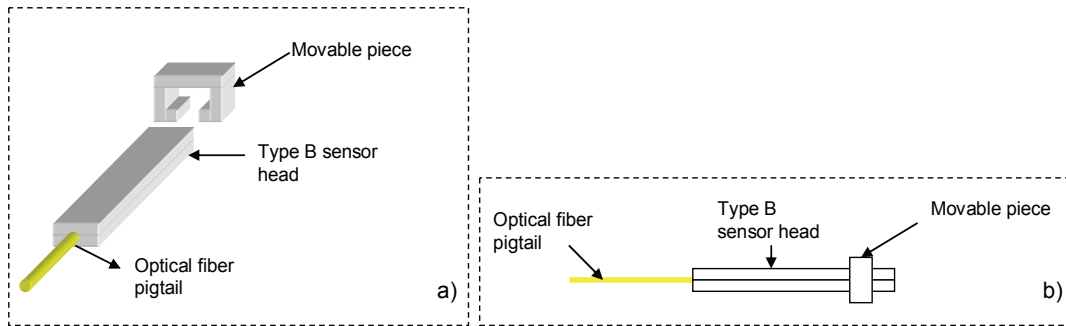


Figure 3.5: Type B package: a) Three dimensional view of the individual components; b) Transverse view of the sensor head that is placed inside the sensor protection case.

3.2.3 Sensor Measurement System and Instrumentation

To measure the response to vibration of the different sensor designs, the system in Figure 3.6 was used. The vibration sensor was placed and fixed on the horizontal plate of a tuneable shaker, which allowed for both the amplitude and the frequency of vibration to be changed. Figure 3.7 illustrates the way the sensor is placed on the shaker plate. Note that in practical applications, the sensor case is glued to the windings at specific locations, which accounts for the method used to fix the sensor onto the shake plate. The same can be achieved by using adhesive tape. The electro-optic processing unit, which is illustrated in Figure 3.8, incorporates both the optical (laser) source and the detection circuit. The source power is distributed among a number of channels (4, 8 or 16, typically), each of which is used to monitor the response of distinct sensors.

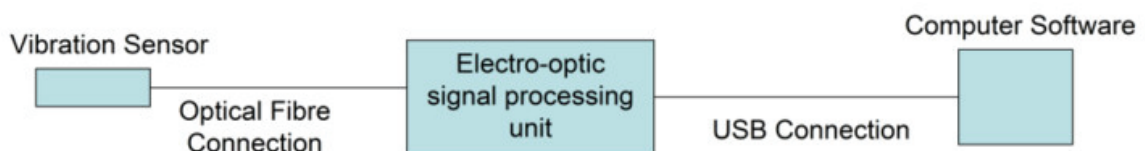
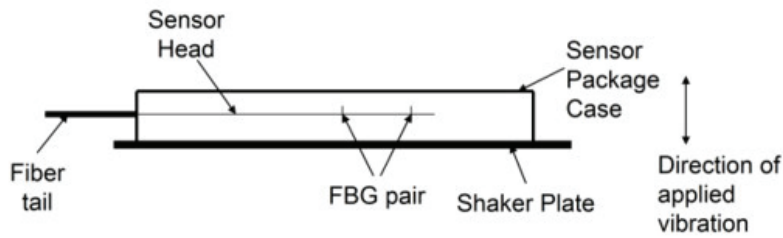


Figure 3.6: Controlled sensor test system.



(a)



(b)

Figure 3.7: The method to place the sensor on the shaker plate: (a) physical, (b) pictorial.



Figure 3.8: VibroFiber™ detection system.

For each channel, as illustrated in Figure 3.9, the optical (laser) signal sent to the fiber is fixed at the wavelength that intersects the reflection spectrum at the midpoint of the rising edge close to the central fringe (denoted by ‘A’ in the inset). At the detector, the power of the reflection spectrum at this wavelength is measured. As the FSR of the VibroFiber™ changes with the change in FBG spatial separation (due to the applied vibration), the power at the bias wavelength fluctuates between the values corresponding to the maximum and minimum of an interference fringe [3.9].

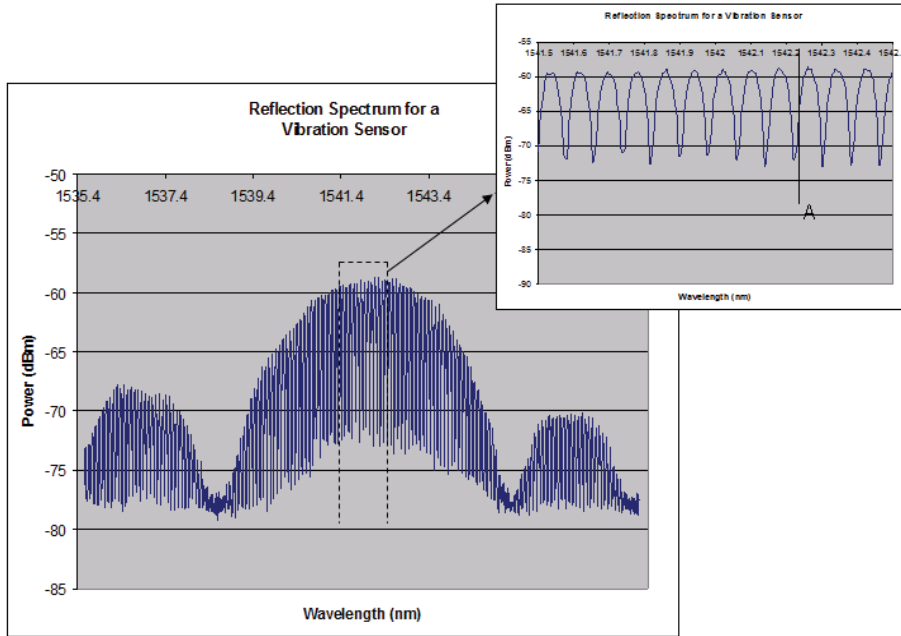


Figure 3.9: Wavelength at which the laser is biased for the vibration measurement.

The detection circuit is connected to a LabView designed virtual instrument which accounts for the measurement calibration and for the conversion of the voltage measurement provided by the detector to a vibration measurement (in micrometer units). The user interface allows performing the calibration of the sensor each time data acquisition is performed. It also provides the numeric values for the measurements of vibration amplitude and frequency. The user interface for the data acquisition software is illustrated in Figure 3.10, which shows a typical plot of the measured change in the optical power at the signal wavelength as a function of time. As observed, for a periodic vibration applied to the sensor head, the corresponding detected signal varies sinusoidally in time, and the user interface displays the measured peak-to-peak amplitude and frequency of the vibration. Note that different versions of the software allow for different capabilities. For example, the latest version allows the continuous calibration and data acquisition in real time, with the possibility of recording snap-shots of data acquired at different moments in time. Moreover, data may be sampled at different rates, and over a certain period of time (1 s by default, but it can be changed manually). For the user interface, the waveform of the sampled data waveform, the measured frequency, and the measured amplitude are displayed in the same window.

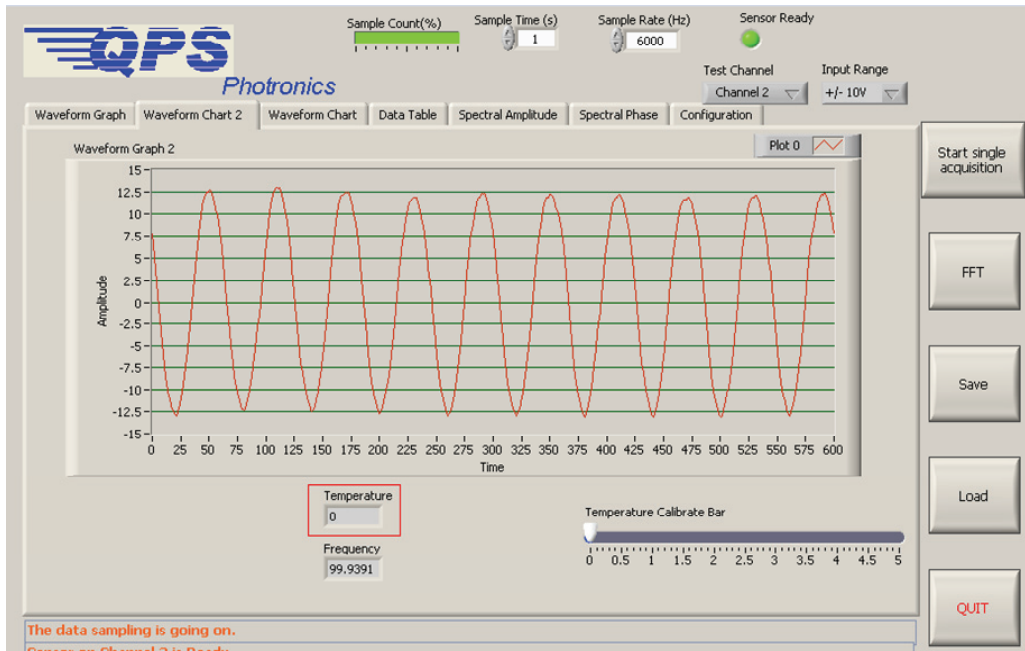


Figure 3.10: User interface illustrating the measurement of the vibration signal.

3.3 Sensor Test Characterization

There are two tests that can be performed to evaluate the operability and sensitivity of a vibration sensor: (1) a frequency response characterization and (2) an amplitude response characterization. Moreover, for each vibration amplitude and frequency selected, a repeatability test proves the degree of reliability of the sensor. For a measurement, the shaker is set to vibrate at the desired frequency and amplitude, and, as mentioned in the previous section, data can be collected either in real time or in a single acquisition over a certain period of time.

3.3.1 Frequency Response Measurement

The first test is performed starting with the assumption that a sensor must be operated at a frequency where the measured amplitude does not change abruptly with small fluctuations about the operating frequency. Ideally, the sensors have a resonance frequency located far from the vibration frequency for which the amplitude is monitored. To get an idea of the operability region, the vibration amplitude is set at 10 μm and the frequency is swept from 50 Hz to 1000 Hz (or 1500 Hz) in steps of 100 Hz. A typical plot for a measured frequency response is shown in Figure 3.11. Note that the measured

values need to be calibrated to obtain the actual value of the amplitude of vibration applied. The calibration method is presented in section 3.3.2.

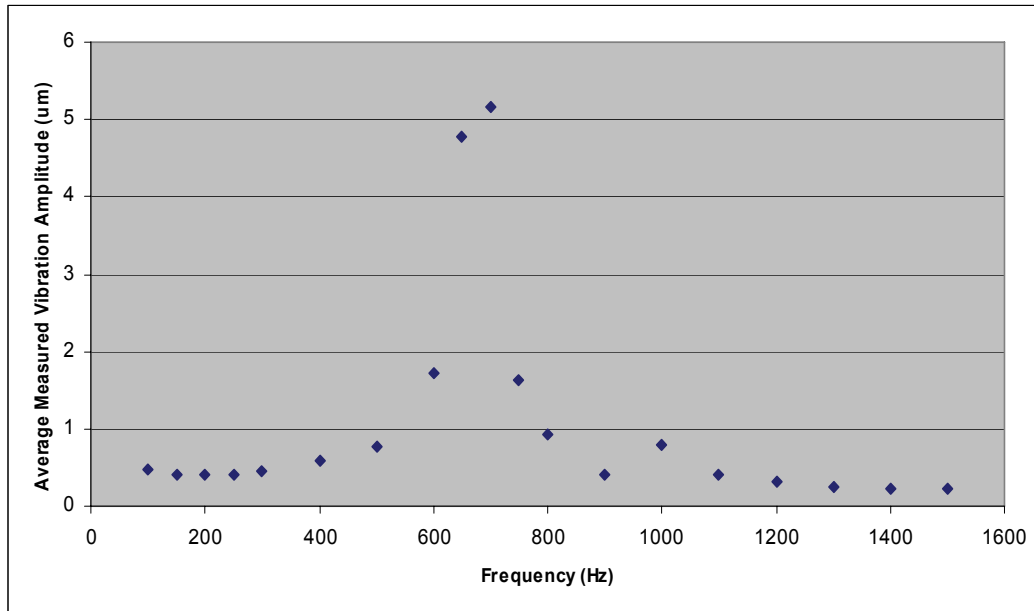


Figure 3.11: Measured frequency response for a VibroFiber™ vibration sensor (sensor package of type A).

Once the frequency response is obtained, a good operability region can be found by choosing the frequency intervals for which the measured amplitude varies with an error of 10 % around the mean of the measurement. For example, from the data used to obtain the plot in Figure 3.11, the possible operability regions extend either from 100 Hz to 300 Hz, or from 1200 Hz to 1500 Hz. Table 3.1 gives an example of how these regions can be quantitatively characterized. The higher and lower frequency regions experience errors of 9.14 % and 6.66 %, respectively. As a result, the sensor can be used at frequencies that are within both regions.

Table 3.1: Example of measuring the operability regions for a VibroFiber™.

Frequency (Hz)	Measured Amplitude (μm)									
	Measurement Number									
	1	2	3	4	5	6	7	8	Mean	
100	0.47	0.46	0.47	0.46	0.47	0.47	0.47	0.46	0.47	
150	0.38	0.41	0.38	0.43	0.43	0.43	0.33	0.46	0.41	
200	0.42	0.38	0.45	0.40	0.42	0.42	0.41	0.43	0.42	
250	0.42	0.41	0.39	0.39	0.42	0.41	0.43	0.40	0.41	
300	0.46	0.46	0.45	0.45	0.46	0.45	0.46	0.45	0.45	
									0.43	Mean (μm)
									0.03	Standard Deviation (μm)
									6.66	Error (%)

3.3.2 Amplitude Response Measurement

This measurement represents a first factor that is used in evaluating sensor reliability, and it gives a measure of sensor sensitivity. In this case, the frequency is set at a value that lies within the pre-determined operability region, and the amplitude is swept from 5 μm to 100 μm in steps of 5 μm . As illustrated in Figure 3.12, with the vibration frequency set at 100 Hz, the measured amplitude is plotted against the applied vibration amplitude, where a package of type A is used. As observed, the curve is linear, which means that there is a one-to-one correspondence between the applied and the measured vibration amplitudes. Moreover, the plot in Figure 3.12 is used to calibrate the measured and the actual vibration amplitudes, with the slope giving a measure of the sensitivity of the sensor. Note that, in the case of a sensor, any calibration curve that does not allow two applied vibration amplitudes to correspond to the same measured amplitude value can be used to achieve reliable measurement.

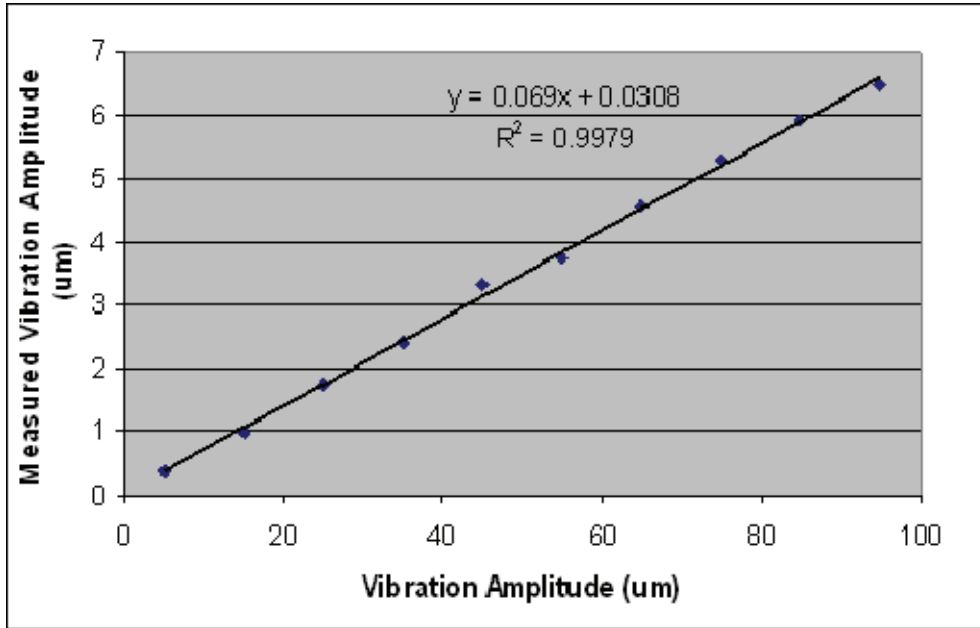


Figure 3.12: Amplitude response plot for a vibration sensor (sensor package of type A).

3.3.3 Repeatability Test

As a second test of sensor reliability, the measurement repeatability ensures that for a certain vibration condition, the value measured by the detection system does not change considerably for different data acquisitions [3.10]. For this test trial, measurements were repeated and data was recorded six to eight times for the same vibration conditions, and using the same measurement unit. In general, the measurement error, which is given as a measure of coefficient of variation and defined as the standard deviation divided by the mean [3.11][3.12], needs to be at most 5%. To obtain a qualitative interpretation of the results, all repeated measurements can be plotted on the same graph. A qualitative example of a good repeatability performance is shown in Figure 3.13. The data corresponding to this graph is shown in Table 3.2, and the associated averages, standard deviations, and errors are shown in Table 3.3. The calculated error values in the operability region found from the frequency response measurements, which covers the range from 100 Hz to 300 Hz, are less than 5 % for every vibration condition, with a repeatability error of 10.002 % at 150 Hz. Note that a larger number of repeated measurements would give a more accurate quantitative repeatability measure.

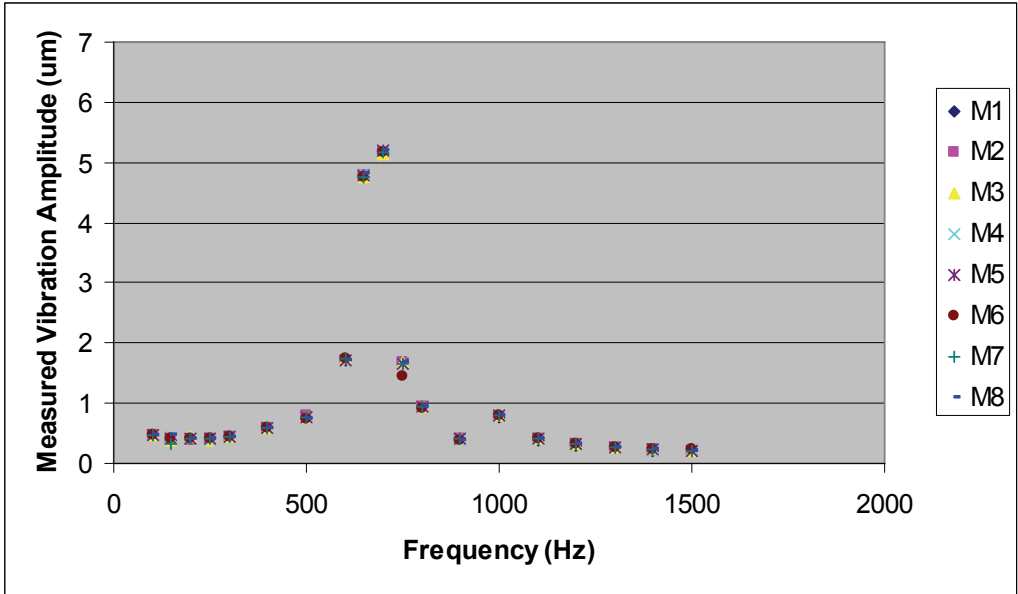


Figure 3.13: Qualitative characterization of the vibration sensor measurement repeatability (sensor package of type A): M1 to M8 represent the different measurements recorded.

Table 3.2: Measured acquired vibration amplitude as a function of frequency.

Frequency (Hz)	Measured amplitude (µm)							
	Measurement number							
	1	2	3	4	5	6	7	8
100	0.473	0.461	0.474	0.46	0.47	0.47	0.474	0.463
150	0.383	0.406	0.382	0.429	0.427	0.425	0.33	0.464
200	0.423	0.382	0.451	0.402	0.422	0.423	0.405	0.426
250	0.415	0.41	0.389	0.387	0.423	0.409	0.426	0.399
300	0.455	0.456	0.452	0.454	0.456	0.452	0.457	0.446
400	0.58	0.591	0.59	0.582	0.592	0.594	0.591	0.584
500	0.769	0.796	0.765	0.772	0.765	0.738	0.766	0.741
600	1.717	1.712	1.736	1.722	1.699	1.732	1.747	1.721
650	4.766	4.798	4.742	4.821	4.772	4.767	4.752	4.819
700	5.146	5.177	5.126	5.192	5.185	5.176	5.158	5.201
750	1.686	1.675	1.678	1.654	1.661	1.448	1.655	1.672
800	0.938	0.944	0.95	0.939	0.937	0.921	0.931	0.939
900	0.427	0.4	0.418	0.377	0.414	0.393	0.408	0.398
1000	0.782	0.774	0.792	0.783	0.795	0.796	0.783	0.799
1100	0.398	0.405	0.414	0.409	0.408	0.406	0.401	0.41
1200	0.31	0.316	0.315	0.316	0.311	0.317	0.315	0.314
1300	0.257	0.26	0.256	0.253	0.265	0.264	0.269	0.253
1400	0.219	0.23	0.225	0.22	0.225	0.23	0.231	0.222
1500	0.222	0.216	0.219	0.223	0.22	0.223	0.217	0.221

Table 3.3: Quantitative characterization of the VibroFiber™ measurement repeatability.

Frequency (Hz)	Average (μm)	Standard Deviation (μm)	Error (%)
100	0.468	0.0059	1.258
150	0.406	0.0407	10.022
200	0.417	0.0205	4.907
250	0.407	0.0145	3.572
300	0.454	0.0035	0.782
400	0.588	0.0052	0.886
500	0.764	0.0182	2.385
600	1.723	0.0149	0.867
650	4.780	0.0297	0.622
700	5.170	0.0251	0.486
750	1.641	0.0789	4.805
800	0.937	0.0086	0.918
900	0.404	0.0158	3.901
1000	0.788	0.0087	1.106
1100	0.406	0.0051	1.254
1200	0.314	0.0025	0.793
1300	0.260	0.0059	2.273
1400	0.225	0.0047	2.092
1500	0.220	0.0026	1.200

3.4 Case Study

A set of sensors of type A were tested to find the relationship between the sensor design and the measurement characteristics. For this purpose, four sensors of different designs in terms of the encased sensor head lengths, with the casing package length held constant, were characterized and compared based on frequency response and on the position of the resonant frequency, which defines the operability region, and based on measurement linearity (or sensor reliability).

3.4.1 Sensor 1300-10

A. Sensor Design

For this design, a 45 mm long sensor head is placed between two adhesive polyamide sheets of dimensions 15 mm by 53 mm. Figure 3.14 shows the position of the sensor head and of the grating relative to the sensor package case. Note that in this figure, the green lines represent the position of the grating sensor along the encased fiber length, which is constant.



Figure 3.14: Design for sensor 1300-10.

B. Frequency Response

With the vibration amplitude set at $30\ \mu\text{m}$, the sensor frequency response as shown in Figure 3.15 illustrates the existence of two resonant frequencies, one at 50 Hz, and a smaller one at 300 Hz. Also, the intended operating frequency, i.e., 100 Hz, is located between the two frequency peaks. This makes the sensor useful in this region. Furthermore, relatively high values could be collected at frequencies in the kHz region, which means that the sensor may be used for high frequency applications. Some customers require that the sensor can be reliably used in the range from 100 Hz to 400 Hz. From error calculations, the sensor values are almost constant in the region from 100

Hz to 200 Hz (the measurement values within this region differ by an error of 7.12 %), and this can be considered as one of the operability regions of the sensor.

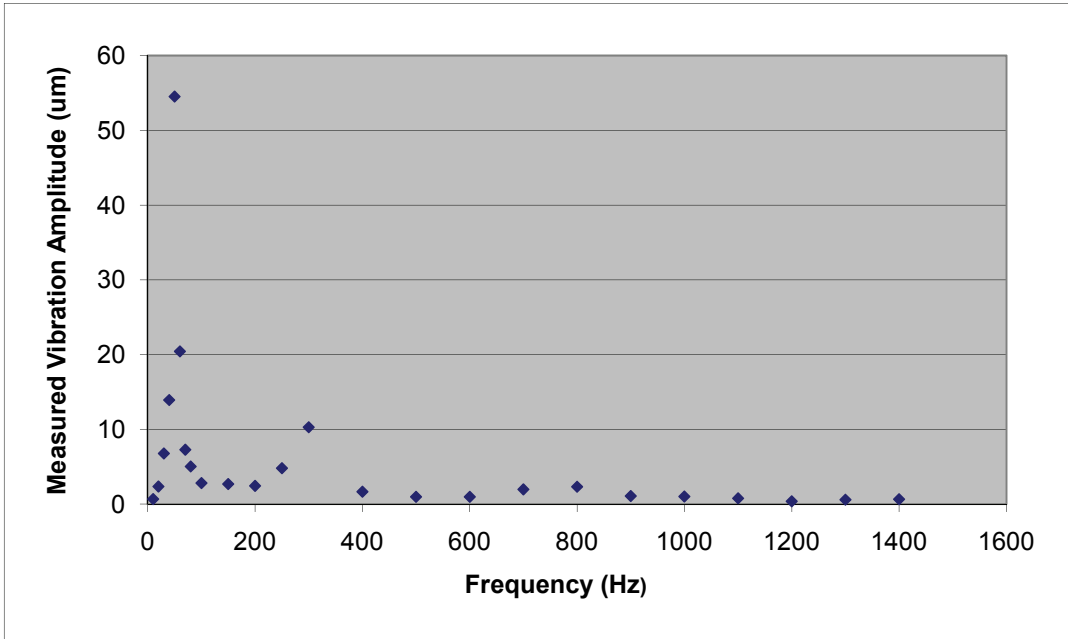


Figure 3. 15: Frequency response for sensor V1300-10.

C. Linearity

The line approximating the measurement dependence on vibration amplitude for a frequency of 100 Hz is shown in Figure 3.16. As observed, measurement increases quite linearly (with a relatively high slope of 0.0981) with increasing vibration amplitude, which means that the sensor may be confidently used at 100 Hz to measure changes in vibration amplitude.

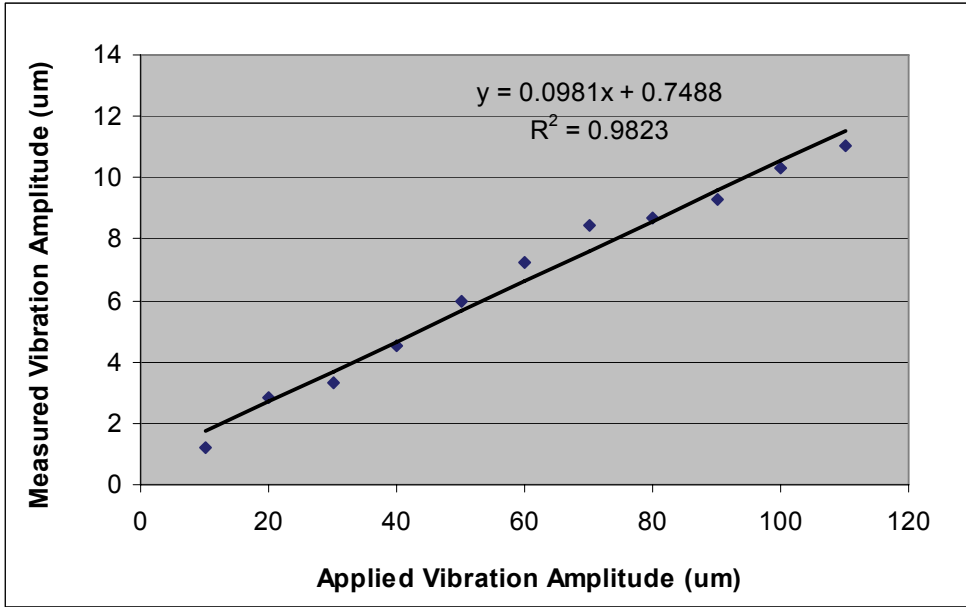


Figure 3.16: Plot of the measured value as a function of vibration amplitude at frequency 100 Hz for sensor V1300-10.

3.4.2 Sensor 1300-19

A. Sensor Design

Next, a sensor head of 40 mm is placed between two adhesive polyamide sheets of dimensions 9.5 mm by 48 mm. Figure 3.17 shows the position of the grating inside the packaging case.

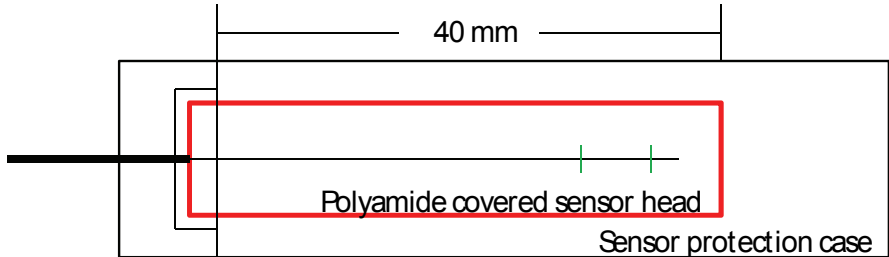


Figure 3.17: Design for sensor 1300-19.

B. Measurement Frequency Response

When the vibration amplitude is set to 30 μm, the frequency response is illustrated in Figure 3.18. As observed, the sensor experiences two resonant frequencies, one at 40 Hz, and a smaller one at 125 Hz. The resonance at the higher frequency makes it difficult to the use the sensor around 100 Hz. Nevertheless, operability region can be considered at

frequencies between 400 Hz and 600 Hz, and between 800 Hz to 1000 Hz, since the measured amplitude is quite invariable with changing frequency.

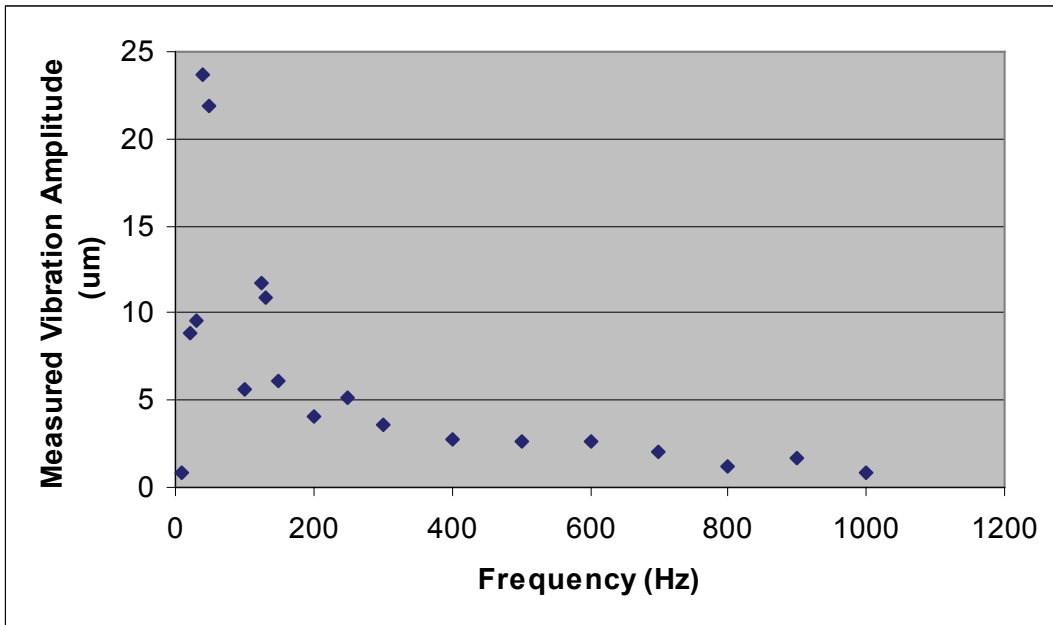


Figure 3.18: Frequency response for sensor V1300-19.

C. Linearity

As observed in Figure 3.19, even though at 100 Hz the operability of the sensor is restricted by resonance, the measurement increases linearly with increasing vibration amplitude (slope of 0.1668). However, since small changes in frequency may lead to high changes in measurement, the measurement repeatability is compromised when the sensor is operated at around 100 Hz.

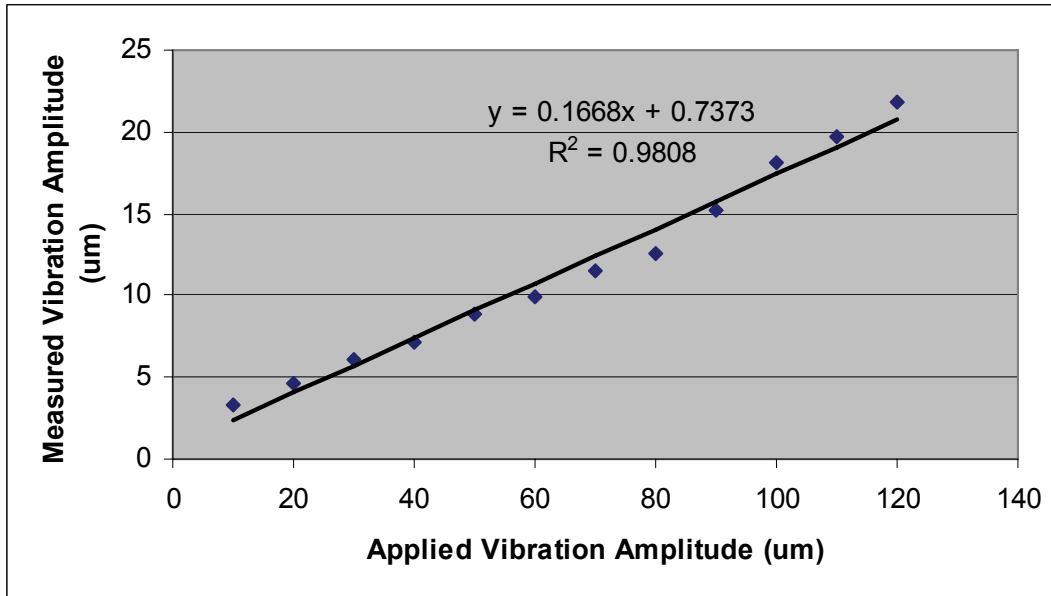


Figure 3.19: Plot of the measured value as a function of vibration amplitude at 100 Hz for sensor V1300-19.

3.4.3 Sensor 1300-20

A. Sensor Design

For this design a 30 mm long sensor head is placed between two polyamide sheets of dimensions 8.5 mm by 38 mm each. The diagram showing the position of the sensor head inside the protecting case is shown in Figure 3.20.

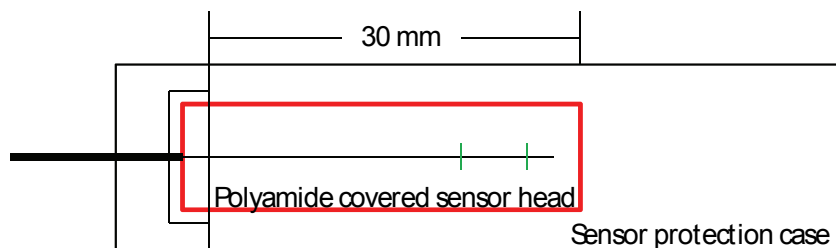


Figure 3.20: Design for sensor 1300-20.

B. Measurement Frequency Response

As observed in Figure 3.21, with the vibration amplitude set at 30 μm , the sensor experiences a resonant frequency at 125 Hz. Thus, the VibroFiberTM's use at around 100 Hz is limited.

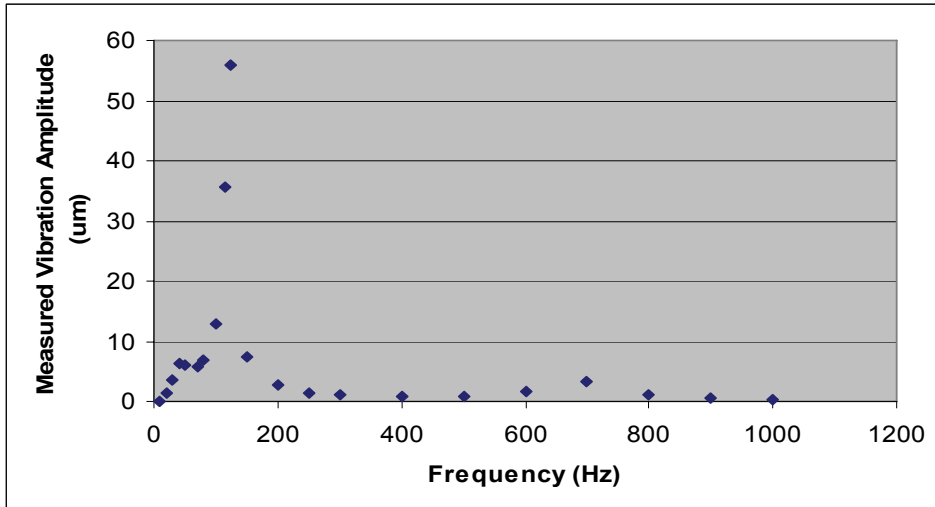


Figure 3.21: Frequency response for sensor V1300-20.

C. Linearity

Even though the operability of the sensor is restricted by the resonance at 125 Hz, the amplitude response at 100 Hz increases linearly (with a relatively high slope of 0.3891) with increasing vibration amplitude, as shown in Figure 3.22. However, the repeatability of measurements may be influenced by the abrupt changes in measurement around the resonant frequency, and specifically at 100 Hz.

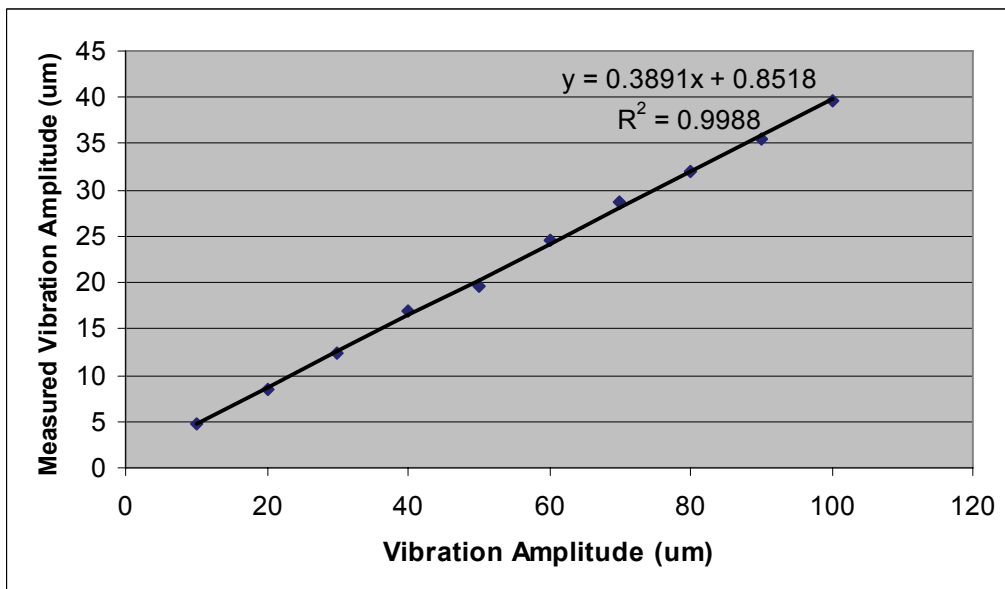


Figure 3.22: Plot of the measured value as a function of vibration amplitude at 100 Hz for sensor V1300-20.

3.4.4 Sensor V1300-22

A. Sensor Design

This design consists of a 15 mm long sensor head placed between two polyamide sheets of dimensions 15 mm by 23 mm each. The diagram showing the position of the sensor head inside the sensor case is shown in Figure 3.23.

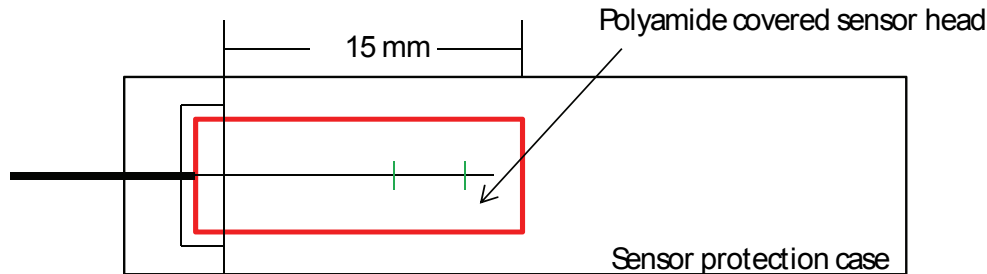


Figure 3.23: Design for sensor 1300-22.

B. Measurement Frequency Response

As illustrated in Figure 3.24, from the frequency response measured at a vibration amplitude of 30 μm , this sensor experiences two resonant frequencies, one at 150 Hz, and a smaller one at 750 Hz. As observed, the first resonant frequency is very close to 100 Hz, which means that, in this region, small changes in frequency may result in different measurement results, thus compromising the repeatability. Nevertheless, the sensor can be used in a region around 400 Hz because, from 300 Hz to 500 Hz, where the measurement varies with an error of 3.01 %.

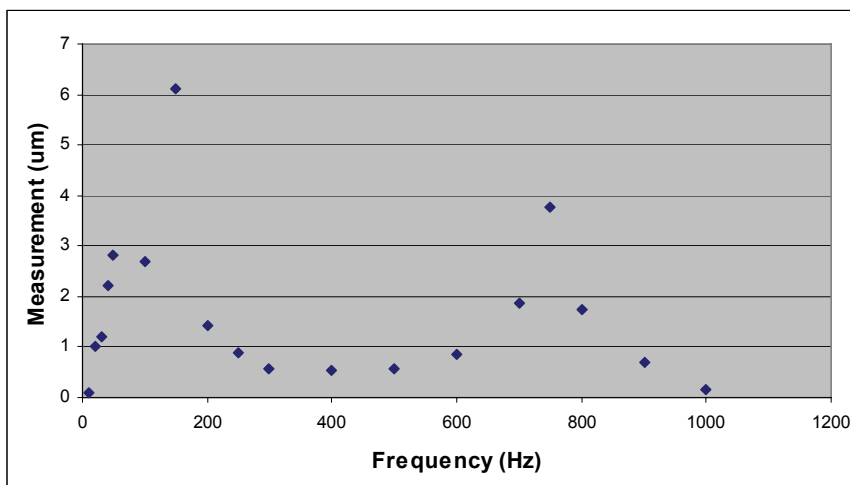


Figure 3.24: Frequency response for rensor V1300-22.

C. Linearity

As shown in Figure 3.25, the linearity of this sensor is not as good as for previous designs which have longer sensor head designs. Also, the measured amplitude is relatively low, which means that energy is distributed among the many harmonics observed in the detected signal spectrum. For example, when the vibration amplitude is 10 μm at 159.2 Hz, the spectrum in Figure 3.26 shows that the difference between the energies of the first harmonic and that of the main frequency is less than 20 dB. Thus, a large amount of energy is transferred to the first harmonic.

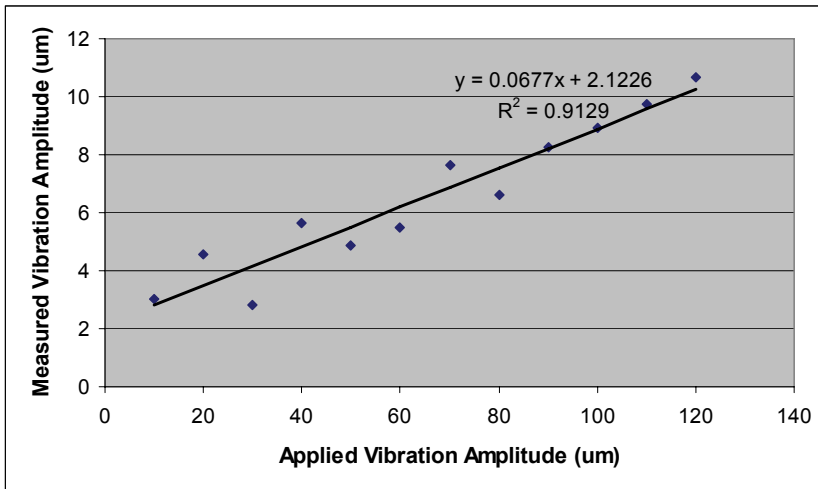


Figure 3.25: Plot of the measured value as a function of vibration amplitude at frequency 100 Hz for sensor V1300-22.

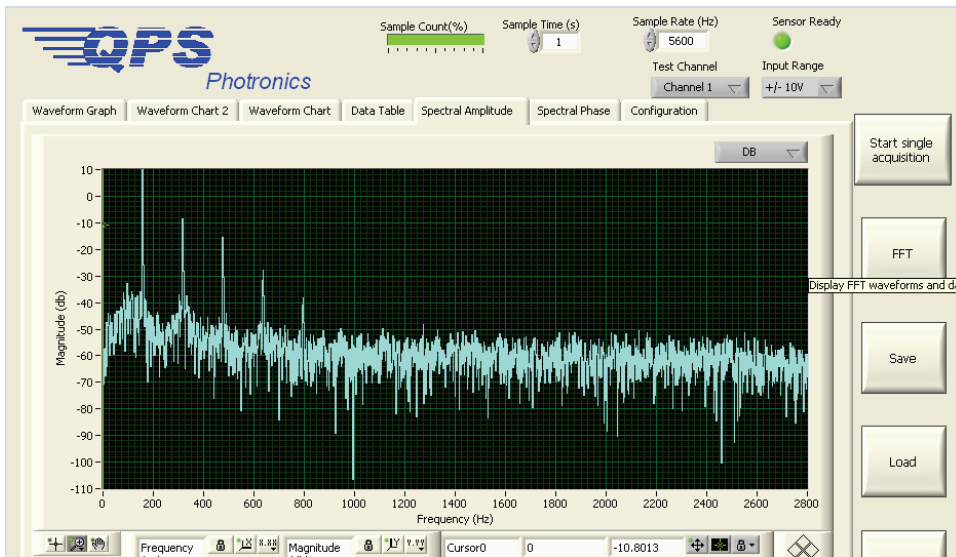


Figure 3.26: Spectrum of sensor 1300-22 when the frequency is 150 Hz and the vibration amplitude is 10 μm .

The results for the four designs tested show that, for the specified conditions, the best suited design is the one with the longest sensor head. However, depending on the application the sensor is intended to be used for, the intermediate size sensor head designs may also be used: they show almost constant variation with frequency for the region 400 Hz to 1500 Hz. However, to reach a decision about the best sensor head length, these tests need to include a higher number of designs of each type. Moreover, these tests ignored the repeatability measurement, which makes it possible to further decide on the proper operability of the vibration sensor.

3.5 Summary of Measurement Results

The results of testing a number of type A and B packaged sensors are summarized in Tables 3.4 to 3.9. From a calibration curve perspective, sensor packages of type A show better linearity than packages of type B. Here linearity is represented by the value of R-squared, which needs to be as close to 1 as possible. For example, most sensors of type A (56 % of the ones tested) show R-squared values greater than 0.99, with the lowest value of 0.9473. On the other hand, the lowest R-squared value for type B packaged sensors is 0.8776, with only 21 % of sensors having linearity higher than 0.99. Moreover, Tables 3.4 and 3.5 show that for different sensors with operability regions around 100 Hz, the slopes of the calibration curves vary from 0.0377 to 0.5675. This shows that the sensors experience a large difference from one design to another, which is undesirable in practical applications.

Table 3.4: Sensor versions V1295 with packages of type B.

Sensor (V1295-)	Operability Region (Hz)	Resonant Frequency (Hz)	Slope	R_squared
6	100-300	NA	0.0476	0.9414
8	100-250	650	0.3137	0.9493
10	100-400	NA	0.0176	0.9787
11	100-350	NA	0.0701	0.9687
13	100-400	900	0.0969	0.9909
16	100-350	NA	0.055	0.9614
17	100-400	800	0.055	0.9916
18	100-400	NA	0.0666	0.8776

Table 3.5: Sensor versions V1300 with packages of type B.

Sensor (V1300-)	Operability Region (Hz)	Resonant Frequency (Hz)	Slope	R_squared
2	100-400	750	0.5675	0.9597
5	100-400	850	0.0407	0.9524
7	100-200	700	0.069	0.9979
8	100-300	700	0.0383	0.9757
11	100-300	650	0.0377	0.9955
14	100-400	650	0.0404	0.9959

Table 3.6: Sensors with packages of type A.

Sensor Code	Operability Region (Hz)	Resonant Frequency (Hz)	Slope	R squared
V11	100-300	550	0.0689	0.9644
T126316V6	100-400	700	0.0158	0.9985
V1280-20	500-700	200	0.0853	0.9959
T126317V6	100-300	600	0.0216	0.9972
V18	100-300	700	0.0122	0.9738
126-12	500-900	300	0.0291	0.9863
V7	100-400	700	0.1532	0.9878

Table 3.7: Sensor versions V1264 with packages of type A.

Sensor Code (V1264-)	Operability Region (Hz)	Resonant Frequency (Hz)	Slope	R squared
7	300-600	1400 and 100(lower)	0.0117	0.9645
9	100-300, 1000-1400	600	0.1259	0.9938
11	40-70, 100-300, 1100-1500	700	182	0.9995
12	100-200	350 and 1100(lower)	0.0411	0.9886

Table 3.8: Sensor versions V1300 with packages of type A

Sensor Code (V1300)	Operability Region (Hz)	Resonant Frequency (Hz)	Slope	R squared	Sensor Head Length(mm)
10	100-200	50 and 300(lower)	0.0981	0.9823	45
19	400-700	40 and 125(lower)	0.1668	0.9808	40
20	300-500	125	0.3891	0.9988	30
22	NA	150	0.0677	0.9129	15

Table 3.9: Sensor versions V1280 with packages of type A.

Sensor (V1280-)	Operability Region (Hz)	Resonant Frequency (Hz)	Slope	R squared
1	100-200	400	0.0838	0.9986
2	100-400	800	0.0784	0.9974
3	100-300	700	0.1079	0.9979
4	100-400	675	0.0729	0.9942
5	100-300	650	0.2272	0.9995
6	100-200	470	0.1999	0.9626
7	100-400	800 and 1300 (lower)	0.0902	0.9864
8	100-250	475	0.2356	0.9967
9	700-900	375	0.0729	0.9937
10	100-400	700	0.1662	0.9999
11	800-1400	500	0.2016	0.9974
12	100-200 and 800-1400	450	0.0551	0.9995
13	100-300	600	0.2983	0.9473
14	90-100	450 and 1500(lower)	0.2272	0.9681
15	100-500	950	0.225	0.9979
21	100-250, 800-1400	500	0.1461	0.9997

3.6 Power Budget for TDM Applications

3.6.1 Objective

One of the advantages that wavelength-encoded information based sensors, such as the VibroFiberTM proposed by QPS Photonics, is the possibility to measure the response from multiple sensors using wavelength multiplexing techniques. Moreover, for each spatial channel (i.e., each fiber length connected to one of the channel inputs), TDM can be used to further increase the number of sensors that can be interrogated [3.13]. The power budget analysis is used to find the number of sensors that can be multiplexed over different spans of SMF length and for different sensor reflectivity values.

3.6.2 Power Budget Experiment

To characterize the power budget for the sensor system, the system in Figure 3.26 was used. The laser source is divided among the channels of the detection system proposed by QPS Photonics. First, the power meter is connected directly to the input laser source (point A in Figure 3.27) to find the amount of power that is launched down the sensor link. The measured value was -9.15 dBm. Then the VOA is connected between the source and the sensor under test. The attenuation introduced by the VOA is increased until no signal can be measured by the High Performance System (HPS) 1600 software. The measurement gives a loss tolerance of 6.35 dB. This means that the round trip tolerated loss is 12.7 dB. The power detected at the output of the system is the difference between the power launched into the system and the tolerated loss. Therefore, the minimum power needed to detect a signal at the output is -21.85 dBm.

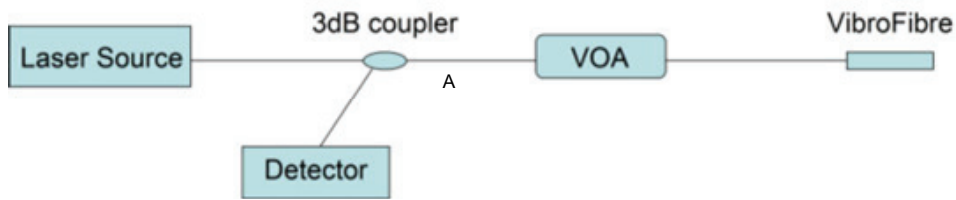


Figure 3.27: Power budget measurement system.

For the given system, the components amounting for the total loss are the optical fiber, which accounts for the distance over which the sensors are distributed, the system margin, and sensor loss owing to the reflection of a narrow band of frequencies as light passes through each sensor. Fiber loss is obtained quantitatively by multiplying the attenuation per kilometre (0.2 dB/km) by the total length of the fiber used, and the system margin is assumed to be 6 dB [3.14].

For a TDM configuration, a number of sensors are connected in series using either APC connectors or splicing (Figure 3.28). To connect the sensors uniformly over a large distance, additional fiber lengths need to be added, which increases the number of connectors. We assume that the APC connector loss is 0.3 dB, while splicing loss is 0.03 dB [3.14].

In the power budget simulation, to calculate the loss of a sensor, the components considered are (1) the overall connector loss, which is given by $4 \times N \times CL$, where CL represents the connector loss; and (2) the overall grating loss calculated as

$10 \times \log_{10}(P_{in} / P_{received})$. Therefore, the loss due to the gratings is $10 \log_{10}((1 - R)^2 / R_{LastSensor}) - 20N \log_{10}(1 - R)$.

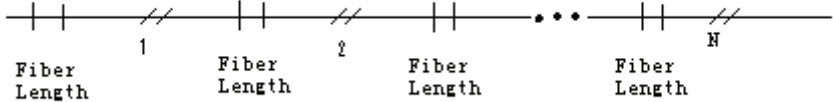


Figure 3.28: The system of N cascaded sensors: continuous vertical line represents a connector; double oblique lines represent the sensor double grating configuration. Note that the vertical lines represent APC connectors or splices.

The four parameters that influence loss in the TDM configuration are FBG sensor reflectivity, fiber length, the type of connector, and the launch power. Depending on these parameters, the results for the number of sensors as functions of these parameters are illustrated in the figures that follow. The reflectivity of the last sensor is assumed to be 0.1 because the sensor cavity operability needs a sensor’s reflectivity to be small. Figures 3.29 and 3.30 show the number of sensors that can be interrogated using TDM as a function of sensor reflectivity for different parameter values. As observed, the number of sensors that can be interrogated decreases with increasing the sensor distribution distance. On the other hand, for a given propagation distance, the number of sensors that can be measured using TDM considerably increases as the APC adaptors are replaced by fusion splices. Moreover, the ability to measure a large number of sensor on one channel improved because a relatively high power was used, i.e., 10 dBm.

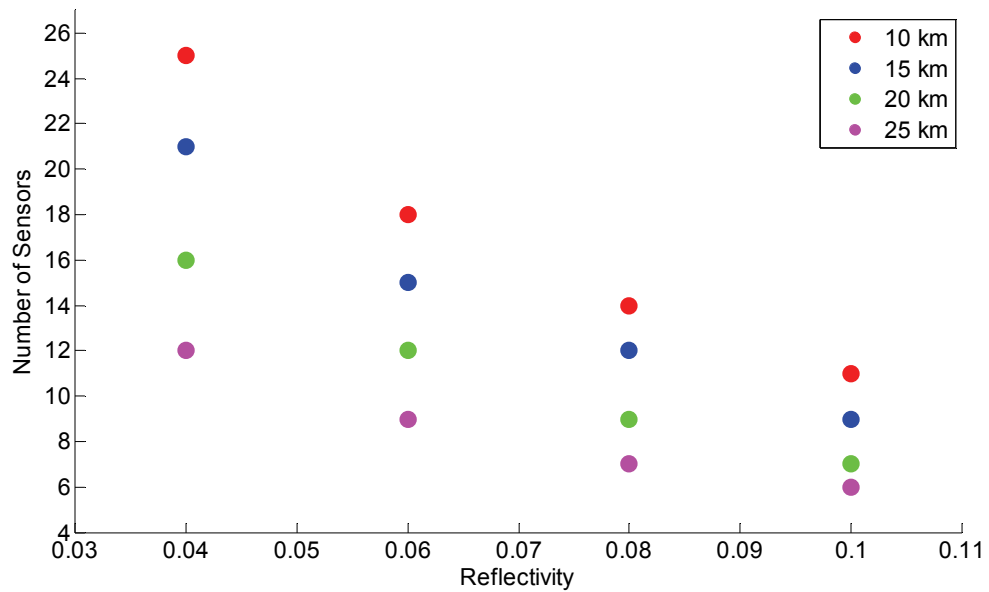


Figure 3.29: Number of sensors that may be interrogated as a function of reflectivity, at different total lengths, when the input power is 10 dBm, the sensors are connected using splicing, and the last sensor reflectivity is 0.1.

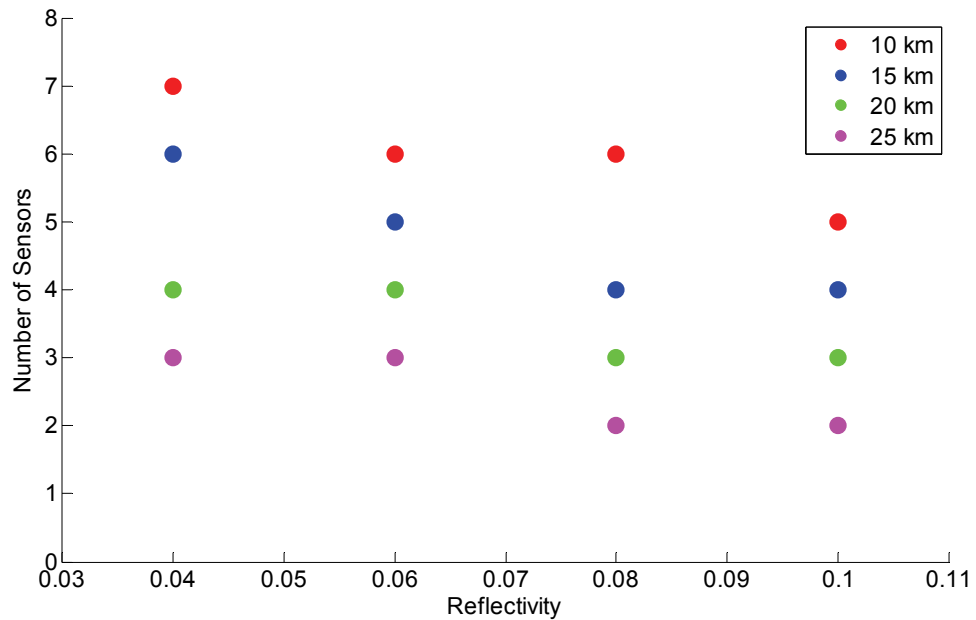


Figure 3.30: Number of sensors that may be interrogated as a function of sensor reflectivity, at different total lengths, when the input power is 10 dBm, the sensors are connected using APC connectors, and the last sensor reflectivity is 0.1.

If the laser power is decreased to 0 dBm, the number of sensors decreases such that no sensors can be interrogated when the fiber length is 15 km or larger. Figure 3.31 illustrates the number of sensors when the fiber length is 10 km for two different reflectivity values of the last sensor (0.1 and 0.2).

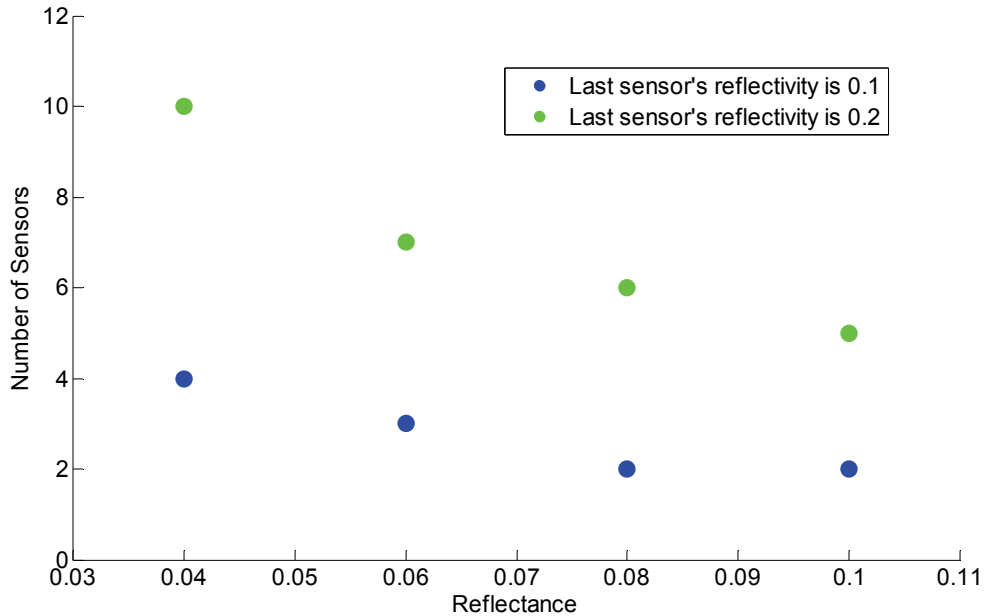


Figure 3.31: Number of sensors that may be interrogated for two different last sensor reflectivity values when the input power is 0 dBm, the fiber length is 10 km and the sensors are connected using splicing.

As the last sensor's reflectivity is increased, the number of sensors that can be interrogated at lower powers increases. However, when the power is -9.15 dBm, with a reflectivity of 0.8 for the last sensor and with splicing, for a fiber length of 10 km, the number of sensors that can be interrogated is only 2 (Figure 3.32). For the same input power, the same fiber length and last sensor reflectivity, when APC connectors are used, no sensor can be interrogated. Therefore, a combination of power amplification and increase in the last sensor's reflectivity would result in a reasonable number of sensors that can be interrogated by using TDM. Note that if the last FBG pair is to be used as sensor, the FBG's reflectivity must be lower than 0.8. Therefore, the power delivered to each channel needs to be increased to be able to measure the response of sensors distributed over distances larger than 10 km.

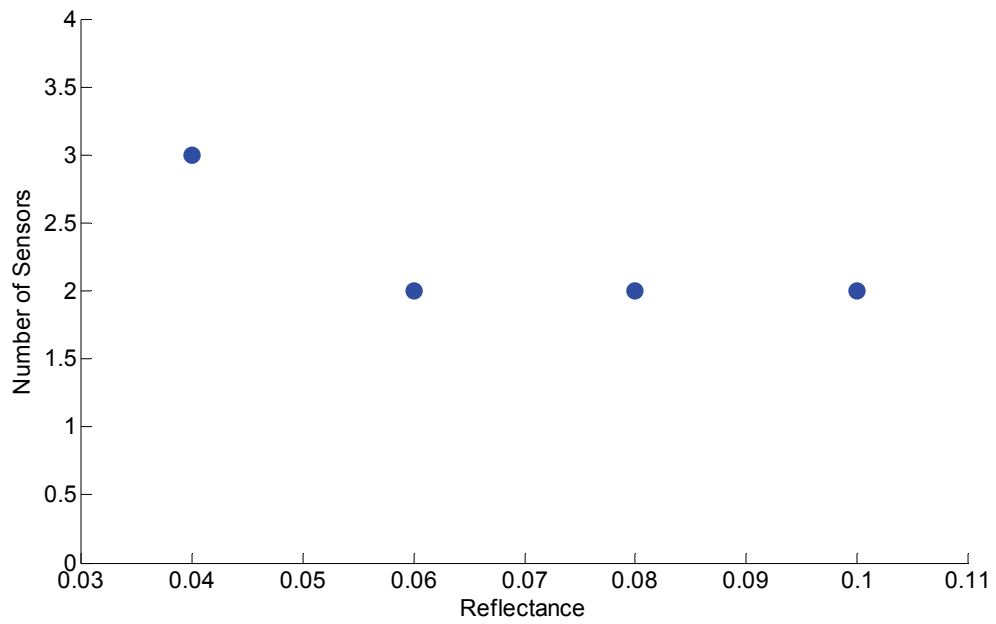


Figure 3.32: Number of sensors that can be interrogated as a function of sensor reflectivity when the input power is -9.15 dBm, the sensors are connected using splicing over a distance of 10 km, and the last sensor reflectivity is 0.8.

3.7 Discussion and Summary

The characterization of the vibration sensors proposed by QPS Photonics is important because the ability to tailor the sensor response by different packaging methods offers the possibility to achieve sensing for a broad range of applications. For example, even though their initial purpose was to monitor vibrations in hydro-electric turbine windings, which vibrate at around 100 Hz, VibroFiber™ sensors find potential use to monitoring the condition of other equipment units experiencing a different vibration frequency. Moreover, experimental results show that the vibration sensor can experience different sensitivities, even though they experience different degrees of repeatability. Therefore, when choosing a desired design, it is important to find a trade-off between operability region, sensitivity, and reliability (this depends both on the linearity of the vibration amplitude response and on measurement repeatability).

Moreover, the wavelength-encoded information provided by the VibroFiber™ and its fiber optic nature allow the sensor to be multiplexed either in the by WDM or by TDM. As provided in this chapter, a rigorous evaluation of the power budget of the system allows the system designer to find a trade-off between the number of sensors that can be multiplexed, the distance over which they are distributed, and the spectral characteristics of the FBG-based sensor used. As discussed, the power budget characteristics for different conditions are as follows:

- Depending on the type of connecting the fiber chords, splicing offers the possibility to multiplex a larger number of sensors, e.g., if the sensor distribution distance is 25 km, a maximum of 11 and 3 sensors can be measured when splicing the fiber and when using APC connectors, respectively.
- The number of sensors that can be interrogated decreases with increasing the distance over which the sensors are distributed.
- As the reflectivity of the last sensor increases, the number of sensors that can be multiplexed increases.
- As the power delivered to the multiplexed sensors increases, the number of sensors that can be interrogated increases. This also allows increasing the number distance over which the sensors are distributed.

From the conditions summarized above, given certain power availability conditions, the system can be designed to optimize the number of sensors that can be multiplexed, which depends on the nature of the measurement required, e.g., long or short distance sensing.

3.8 References

- [3.1] T.K. Gangopadhyay, “Prospects for fibre Bragg gratings and Fabry-Perot interferometers in fibre-optic vibration sensing,” *Sensors and Actuators A*, vol. 113, pp. 20–38, 2004.
- [3.2] H. Fan, J. Qian, Y. Zhang, and L. Shen, “FBG sensors for flexible surface vibration test,” in *Proceedings of the 2007 International Conference on Information Acquisition* July 9-11, 2007, Jeju City, Korea.
- [3.3] H. Fan, J. Qian, Y. Zhang, and L. Shen, “A novel FBG sensors network for smart structure vibration test,” in *Proceedings of the 2007 IEEE International Conference on Robotics and Biomimetics*, December 15 -18, 2007, Sanya, China.
- [3.4] Q. Jiang, Q. Sui, and J. Wang, “Technical and experimental study of fiber Bragg grating vibration sensor based on matching demodulation method,” *Proceedings of the IEEE International Conference on Automation and Logistics*, pp. 18-21, August 2007, Jinan, China.
- [3.5] A. Gonzalez-Segura, J.L. Cruz, M.V. Andres, P. Barrios, and A. Rodriguez, “Fast response vibration sensor based on Bragg gratings written in tapered core fibers,” *Measurement Science and Technoogy.*, vol.18, pp. 3139–3143, 2007.
- [3.6] P. Tavner, L. Ran, J. Penman, and H. Sedding, “Vibration Monitoring” in Condition Monitoring of Rotating Electrical Machines, pp. 159-192, Institution of Engineering and Technology, London, UK, 2008.
- [3.7] K.O. Lee and K.S. Chiang, “Temperature-insensitive fiber-Bragg-grating-based vibration sensor,” *Optical Engineering*, vol. 40, pp. 2582-2585, 2001.
- [3.8] A. Yariv and P. Yeh, “Optical Resonators” in Photonics: Optical Electronics in Modern Communications, ed. 6, pp. 156-210, Oxford University Press, Inc., New York, NY, 2007.
- [3.9] H.-J. Bang, S.-M. Jun, and C.-G. Kim, “Stabilized interrogation and multiplexing techniques for fibre Bragg grating vibration sensors,” *Measurement Science and Technology*, vol. 16, pp. 813–820, 2005.
- [3.10] A.J. Wheeler and A.R. Ganji, “General Characteristics of Measurement Systems” in Introduction to Engineering Experimentation, ed. 3, pp. 7-29, Prentice Hall: Upper Saddle River, NJ, 2010.
- [3.11] G. Atkinson and A.M. Nevill, “Statistical methods for assessing measurement error (reliability) in variables relevant to sports medicine,” *Sports Medicine*, vol. 26, no. 4, pp. 217-238, 1998.

- [3.12] H. Stark and J.W. Woods, Probability and Random Processes with Applications to Signal Processing, ed. 3, p. 170, Prentice Hall: Upper Saddle River, NJ, 2002.
- [3.13] D.J.F. Cooper and P.W.E. Smith, “Simple high-performance method for large-scale time division multiplexing of fibre Bragg grating sensors,” *Measurement Science and Technol.*, vol. 14, pp. 965–974, 2003.
- [3.14] G.P. Agarwal. Fiber-Optic Communication Systems, Third edition, Wiley & Sons Inc.: New York, 2002.

4. Microwave Photonic Filter-based Interrogation System for VibroFiber™ Sensors

4.1 Introduction

Conventionally, sensing using FBGs involves processing the information encoded in the shift of the Bragg wavelength with strain or temperature. Usually this information is extracted by monitoring wavelength shift using an optical spectrum analyzer, or power change using a wavelength-to-power mapping method, which involves using an edge filter. In this experiment, we extend the use of the FBG pair written on the same fiber and separated by 5 to 20 mm. This results in a cavity whose reflection spectrum forms an interference fringe pattern that follows the shape of the individual FBG's reflection spectrum, whose FSR changes with changing FBG separation. As discussed earlier, QPS Photonics used this characteristic to design a sensor capable of monitoring the periodic change in cavity length imposed by vibrations at a fixed frequency. A microwave photonic filter (MPF) is obtained when modulating a multi-wavelength optical source with an RF signal guided through a dispersion medium. We propose using the FBG pair multi-wavelength signal as the source to a MPF system to detect changes in temperature and/or strain. These affect both the center wavelength of the FBG reflection spectrum and the optical path length of the cavity. The former influences the dispersion characteristics of the delay medium, and the latter results in a change in the FSR of the interference signal reflected off the FBG pair structure. We prove that these changes modify the MPF characteristics and allow reliable measurement with increased speed (useful for real-time strain monitoring), and with variable sensitivity and operation range. Note that the packaging method of the vibration sensor allows sensitivity to temperature only. Therefore, the detection principle is proven by monitoring the response of the system to temperature.

In this chapter, the first section presents the theory behind MPF systems. Section two focuses on the effect temperature has on the vibration sensor structure, followed by the results of a conventional method used to measure temperature using the FBG technology, i.e., monitoring the shift in peak wavelength of the FBG pair reflection spectrum with increasing temperature. The final section presents the way the vibration sensor can be

incorporated in a MPF system to achieve temperature measurement; here the principles behind this approach and relevant results are presented. A discussion of the performance achieved and future work solutions that may improve system performance are provided in the conclusion.

4.2 Microwave Photonic Filter Background

A MPF has been historically used in the context of processing radio frequency (RF) signals in the optical domain. The basic structure of such a system is shown in Figure 4.1. As observed, a MPF is obtained when the light from a multi-wavelength optical source (or from a number of sources at different wavelengths) is modulated using an RF signal and sent to a dispersive medium that causes the individual wavelength components to be delayed with respect to each other, and this results in a change in the modulated optical signal, which also depends on the frequency of the modulating RF signal. The delay experienced by the spectral components of the optical input depends on the wavelength spacing between adjacent peaks ($\Delta\lambda$) of the multi-wavelength source, on the length of the dispersive medium (L), and on its dispersion coefficient (D), i.e., $\Delta\tau = DL\Delta\lambda$ [4.1][4.2].

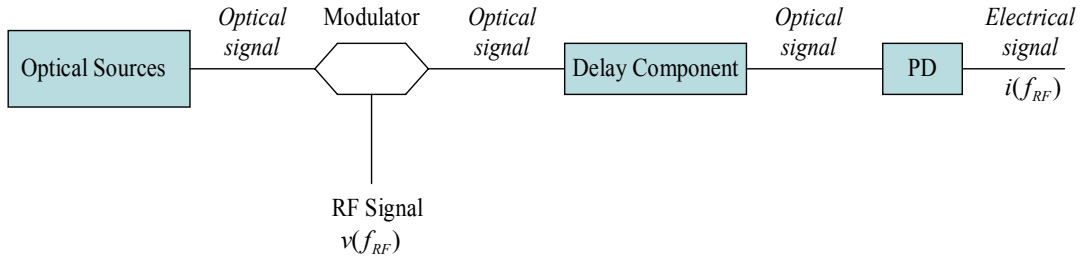


Figure 4.1: General schematic for a MPF system [4.3][4.4].

The responses of MPFs when using double sideband and single sideband amplitude modulation can be defined in [4.3], respectively, as

$$|H_{DSB}(f_{RF})| = R \cos(\beta_2 f_{RF}^2 / 2) \left| \sum_{k=1}^N p_k \exp(-j f_{RF} (k-1) \Delta\tau) \right| \quad (4.1)$$

and

$$|H_{SSB}(f_{RF})| = R \left| \sum_{k=1}^N p_k \exp(-j f_{RF} (k-1) \Delta\tau) \right| \quad (4.2)$$

In these equations, R is the photo-detector responsivity, f_{RF} is the modulating signal frequency, p_k is the peak amplitude of wavelength number k , β_2 is the group delay slope of the dispersive medium, N is the number of peaks in the multi-wavelength source, and $\Delta\tau$ is the delay experienced by each wavelength component. In practice, the amplitude modulation that results from using an electro-optic Mach-Zehnder Modulator (MZM) is double sideband, which causes carrier suppression at certain RF frequencies after the modulated signal passes through a dispersive medium. The second term, $\cos(\beta_2 f_{RF}^2 / 2)$, characterizes the dispersion of the delay medium, and predicts the modulating frequencies at which carrier suppression occurs. The modulating frequency at which this phenomenon observed depends on the dispersion of the delay medium and on its length, which acts as the tuning element of the carrier suppression characteristic. Equations (4.1) and (4.2) also show that the resulting MPF is periodic, with a free spectral range that is inversely proportional to the time delay imposed on the modulated signal by the dispersive medium, which can be used as tuning element if the system is designed such that one or more of the components on which the time delay depends can be changed.

Studies show that there are different methods to tailor the response of a MPF by changing its delay component and/or source characteristics. For example, switching between propagation paths characterized by different delay line lengths can be used to change the delay the different wavelength components of a multi-wavelength source to change the FSR of a MPF. Another possibility is having dispersive media such as single mode fibers, dispersion compensating fibers, or linearly chirped fiber Bragg gratings combined with tuneable sources. Furthermore, fixed wavelength sources can be combined with tuneable delay lines capable to induce a change in filter characteristics, and special chirped FBGs are part of this category [4.3]. There are two types of filters, which are characterized according to their delay component characteristics. First, when optical fiber is used, the MPFs are referred to as fiber delay line filters. They have been extensively investigated since 1980, and, as reported in [4.5], a shift of the filter peaks was achieved in this case using tuneable sources, with a delay element composed of highly dispersive fiber lines. On the other hand, in [4.6] tunability of the filter peaks was achieved using dispersion shifted fibers combined with longer lengths of high dispersion fiber. Moreover, filtering can be achieved by incorporating fiber gratings. For example,

some applications use AWGs as delay components because they of their wavelength selectivity property [4.4][4.7-4.9], which, as discussed in [4.1], can also be used as spectrum slicing components. These can also be built using FBGs, which can easily be tuned by applying strain or by changing the ambient temperature [4.10]. Also, in [4.11], D. Hunter *et al.* use a number of FBGs in series as spectrum slicing or as tap elements, and the distance between them serves as the delay components of the system. In [4.12], S. Torres *et al.* use chirped FBGs of different dispersions as delay components. In their approach, tuning is achieved by applying the same strain to the gratings, whose behaviour changes with dispersion.

In this work, we consider the spectrum slicing property of an FBG pair in a fiber delay line MPF. Its FSR can be changed by applying different temperatures, which affect the spectral characteristics of an FBG pair structure. In this case, the signal that passes through the delay medium changes in response to temperature.

4.3 Fiber Bragg Grating Pair Based Sensor Temperature Response

As introduced earlier, an FBG pair sensor consists of an in-fiber Frabry-Perot interferometer having as partial reflectors two FBGs separated by a small distance (as referred in Figure 3.1). Therefore, the structure can be used to slice a broadband source into a multi-wavelength signal. The wavelength separation between peaks can be calculated as $\Delta\lambda = \frac{\lambda^2}{2nL}$, where n and L are the effective refractive index and the length of the cavity, respectively, and λ is the wavelength corresponding to the peak of the reflection spectrum [4.13]. Moreover, the reflectivities of the FBGs are very low, e.g. 10% to 20%, and, as a result, the resulting taps have an almost sinusoidal variation. The reflection spectrum and its fringe shape were presented in Figure 3.2. For the packaged FBG pair sensor for which the measurement was taken, the FSR is approximately 80 pm.

As mentioned earlier, FBGs reflection spectra are sensitive to temperature, which affects the effective refractive index, a parameter the wavelength reflected by the FBG depends on. Moreover, the spectrum of the FBG pair structure follows the spectrum of the individual gratings. Thus, the most common method to monitor wavelength shift as a result of temperature change is to use an optical spectrum analyzer (OSA) and measure

the center wavelength. As such, the experimental setup used is as illustrated in Figure 4.2. Light from a broadband source (BBS), which corresponds to the ASE from an EDFA, is sent to the FBG pair-based sensor through a circulator. The reflected signal is sent to a high resolution OSA (of 0.16 pm resolution bandwidth) from Apex Technologies. Note that the high resolution is necessary to observe the interference peaks inside the FBG spectrum envelope. To obtain the temperature response, the spectrum was first measured at room temperature (25°C). Then, the sensor was placed in boiling water at 100°C, and a measurement of its spectrum was recorded. Then, the temperature was periodically measured using a thermometer, and measurements were taken at intervals of 10°C from 80°C to 40°C. Figures 4.3a) and 4.3b) show how temperature change affects the reflection spectrum. For clarity, only the spectra at two temperatures are shown in each plot.

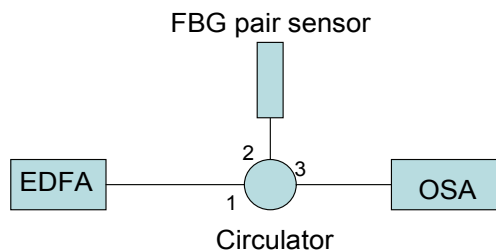
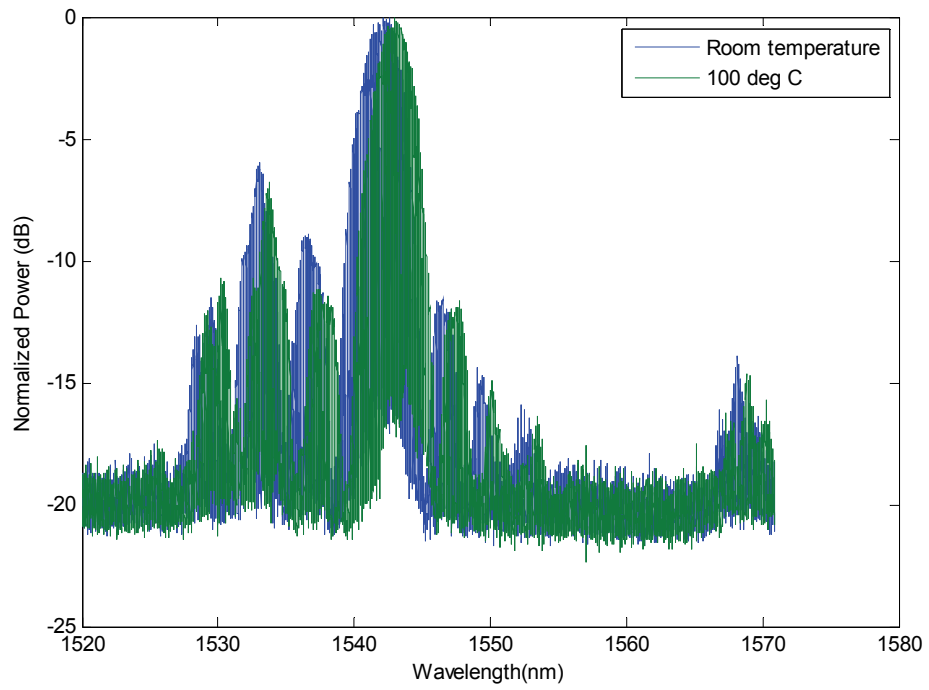
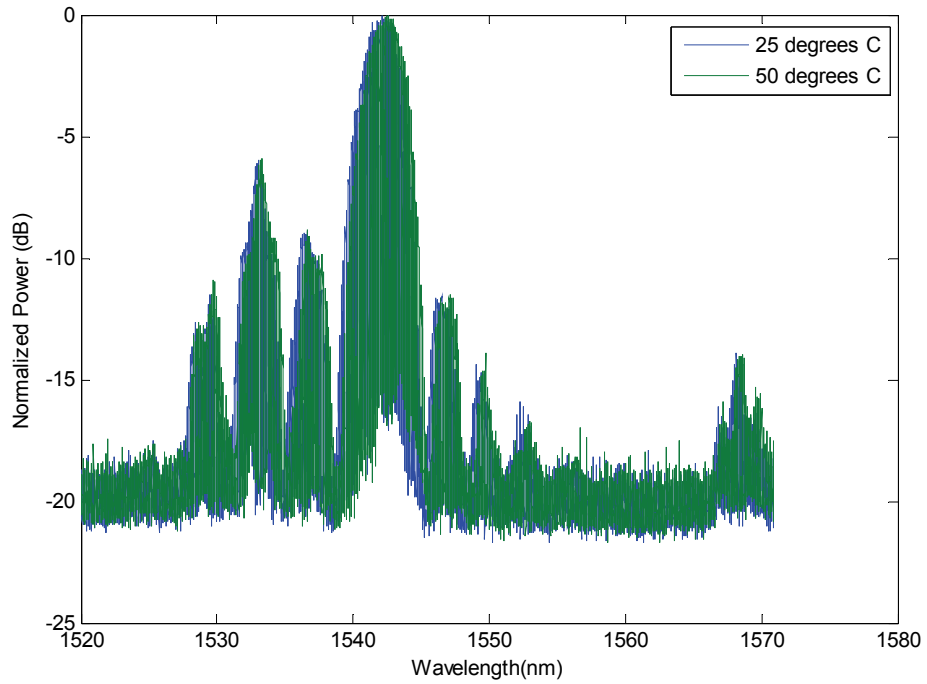


Figure 4.2: Setup used to measure FBG pair spectrum change with temperature.



a)



b)

Figure 4.3: FBG comparison of reflection spectra at room temperature and at a)100° C , and at b)50° C.

The sensitivity of the temperature measurement method is found by plotting the Bragg wavelength, which corresponds to the center wavelength of the spectrum, versus temperature, which is shown in Figure 4.4. As observed, the sensitivity is 12.1 pm/°C, which closely corresponds to the typical sensitivities observed in previous temperature measurement methods that employ FBG as sensing elements: sensitivities of 16 pm/°C and of 13 pm/°C were reported in [4.15] and [4.16], respectively. Therefore, for precise measurements, wavelength shift with temperature requires using OSAs with resolutions lower than 10 pm.

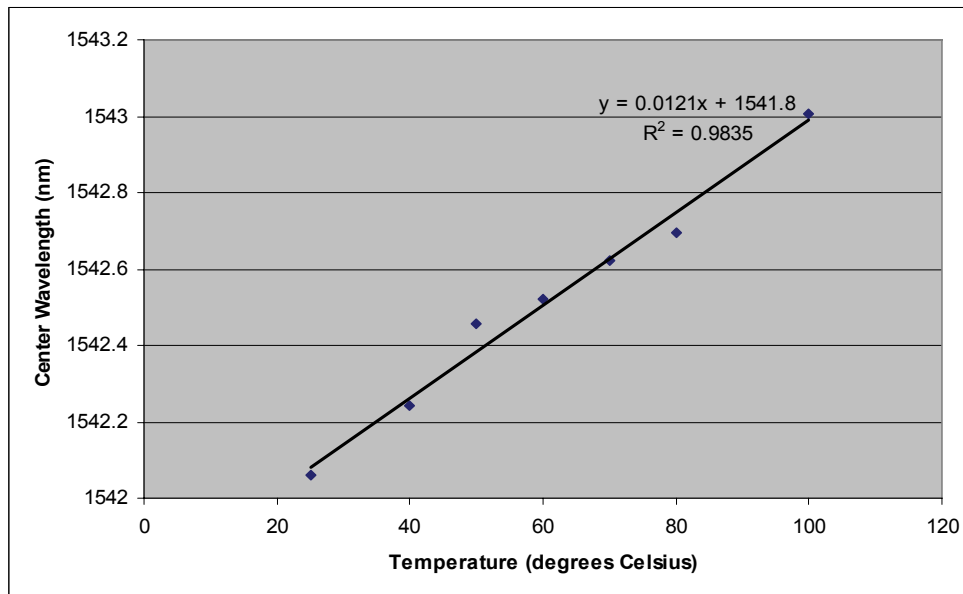


Figure 4.4: Reflection spectrum center wavelength of an FBG pair as a function of temperature.

When temperature changes are applied to the FBG pair, the refractive index of the fiber between the FBGs also changes, and this implies a change in the optical path length of the cavity. As a result, the free spectral range of the interference pattern is expected to change with temperature. The average fringe separation was thus calculated from the traces of the reflection spectra measured at different temperatures. For this purpose, the separations between adjacent peaks that had power levels greater than the level 6 dB lower than the peak value were calculated. For each temperature, the average FSRs are shown in Table 4.1. As observed, the fringe separation of the interference spectrum changed from 80.85 pm at room temperature (25°C) to 81.03 pm at 100°C. Since the change is so

small, the FSRs at temperatures in between these two values are within the aforementioned extremes.

Table 4.1: Average free spectral range for the reflection spectrum of the FBG pair as a function of temperature.

Temperature (°C)	Free Spectral Range (pm)
25	80.85
40	80.97
50	80.98
60	80.93
70	80.95
80	80.93
100	81.03

As presented in this section, for the FBG pair, temperature affects both the center wavelength of the reflection spectrum for the individual gratings and the fringe separation of the interference pattern inside the FBG spectrum. The observed insignificant change in FSR as a function of temperature can only be measured with even higher resolution optical spectrum analyzers. Therefore, to avoid using these, the multi-wavelength nature of the FBG pair structure reflection spectrum allows it to be used as spectrum slicing element in a fiber delay MPF system. Moreover, since the filter peaks separation is dependent on the characteristics of the multi-wavelength source, whose spectral characteristics change with temperature, it is worthwhile to use a MPF as an interrogation unit, i.e., take advantage of the changes on the filtering characteristics by temperature change.

4.4 Microwave Photonic Filter-based Temperature Measurement

As mentioned earlier, the spectrum slicing property of the FBG pair structure allows it to be used to achieve the source to a MPF system. For convenience, a lightwave spectrum analyzer (LCA) was used to provide the RF frequency bias to the amplitude modulator used to modulate the multi-wavelength signal. The delay medium used was a length of SMF, for which the length had to be determined according to the characteristics of the source used so as to avoid the aforementioned carrier suppression effect that would suppress certain filter peaks. This section first presents how changing the source characteristics affects the response of the MPF. Then, the effect of the delay component on the filter variation is explored, and the section ends with the presentation of the experimental results for the MPF approach used to measure temperature with the FBG pair sensor.

4.4.1 Temperature Effect on the Response of a MPF

Theoretically, since the Bragg wavelength is directly proportional to the refractive index— $\lambda_{Bragg} = 2n\Lambda$ where Λ is the pitch of the grating—the free spectral range also changes as $\Delta\lambda = \frac{2n\Lambda^2}{l}$ [4.14]. Therefore, the FSR of the grating increases with increasing temperature, which affects both the optical path length of the cavity and the reflection spectrum center wavelength. This implies an increase in the time delay experienced by the different wavelength components of the source after passing through the dispersive medium. Since the frequency spacing between the peaks of the MPF is inversely proportional to the time delay [4.13], as temperature increases, the peak frequency of the filter decreases, i.e., the free spectral range of the filter decreases.

As discussed in [4.3], the sinusoidal variation of the fringes of the reflection spectrum for the FBG pair structure, which results from the low reflectivity of the gratings, disrupts the periodic nature of the filter, and results in a two peaks filtering response: one peak corresponds to the direct current (DC) value, which can be ignored, and another peak at a frequency given by $f_{RF} = \frac{1}{DL\Delta\lambda}$. Figure 4.5 illustrates the MPF response over 20 GHz.

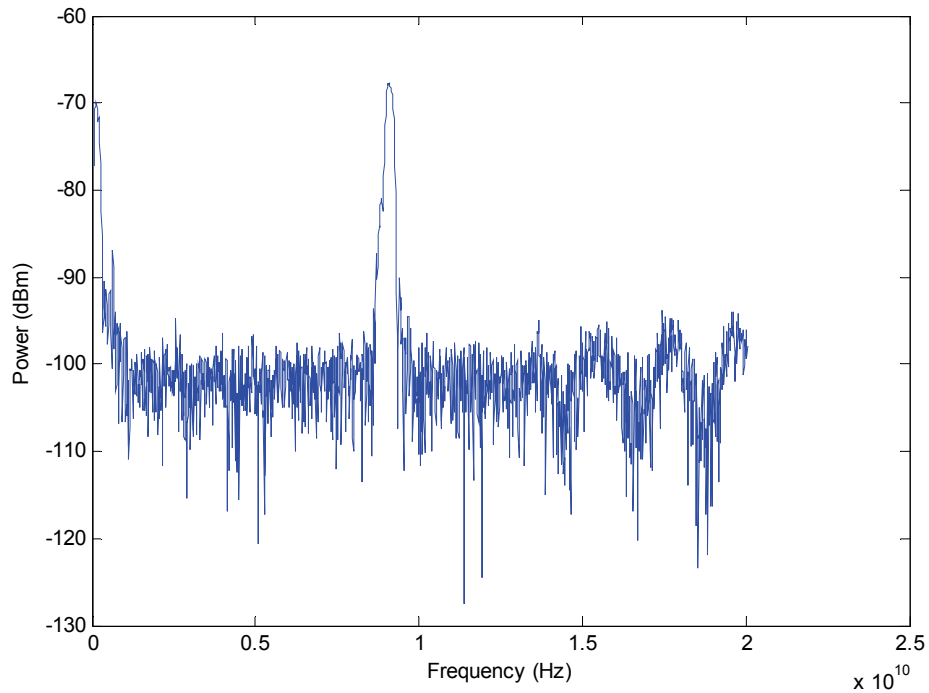


Figure 4.5: MPF response at room temperature when the single mode fiber length is 85 km.

4.4.2 Effect of Delay Fiber Length on the Characteristics of the MPF

As a consequence to the expected two peak variation of the MPF in response to the FBG pair structure used as source, the first experiment performed on the system is finding the appropriate length of SM fiber used here as delay component that does not result in carrier suppression at the frequencies where the filter peaks are predicted by Equation (4.2). For this purpose, theoretical simulations were performed to find the potential lengths of fiber that do not result in filter peak suppression. The plot of the first maximum of the carrier suppression term and the wavelength spacing between the filter peaks as functions of SMF fiber length are shown on the same graph in Figure 4.6. As observed from simulation, any length of fiber between 65 km and 85 km shows potential use in achieving double peak filtering response.

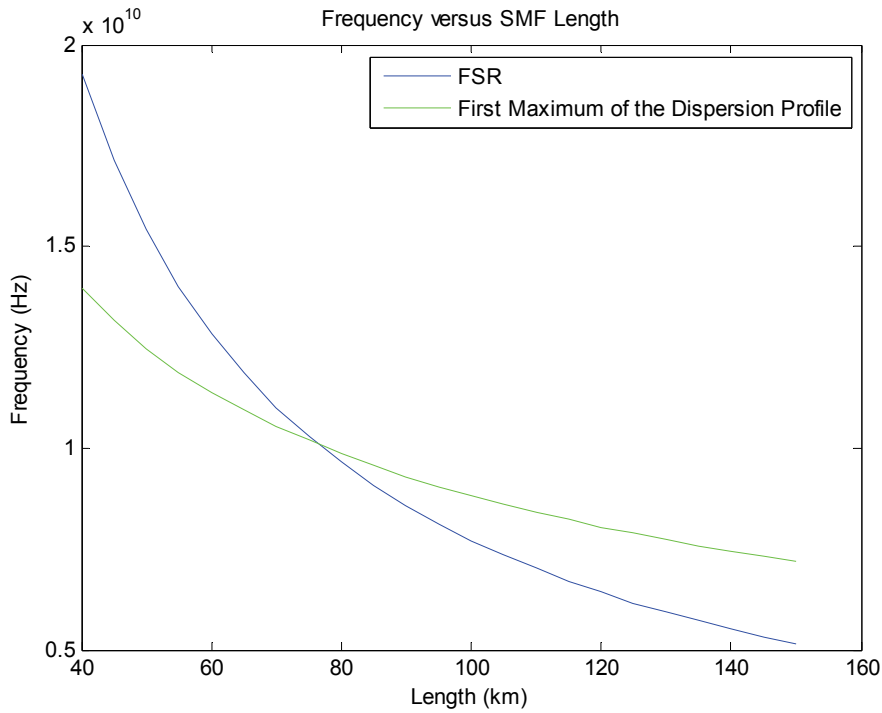


Figure 4.6: First maximum superimposed on the estimated wavelength spacing between the filter peaks as functions of SMF fiber length.

The setup in Figure 4.7 was used to confirm that the lengths of fiber predicted by theory result in the expected two peaks filter response. An example of a dispersion transfer function obtained for an SMF length of 85 km, whose dips account for carrier suppression at those frequencies, and the measured MPF response are shown on the same plot in Figure 4.8 where FSR represents the theoretical calculation for the frequency spacing between the two peaks of the MPF. For the plots in the same figure, the observed decrease in amplitude of the curve characterizing dispersion can be explained by the decreasing linear variation of the EO-MZM, which is illustrated in Figure 4.9.

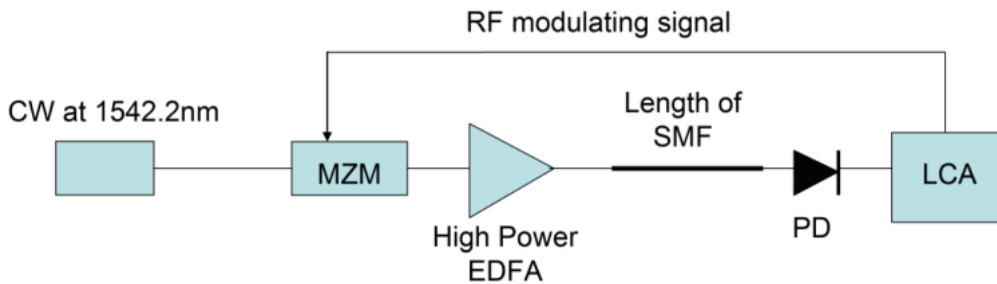


Figure 4.7: Experimental setup used to find the optimum SMF fiber length.

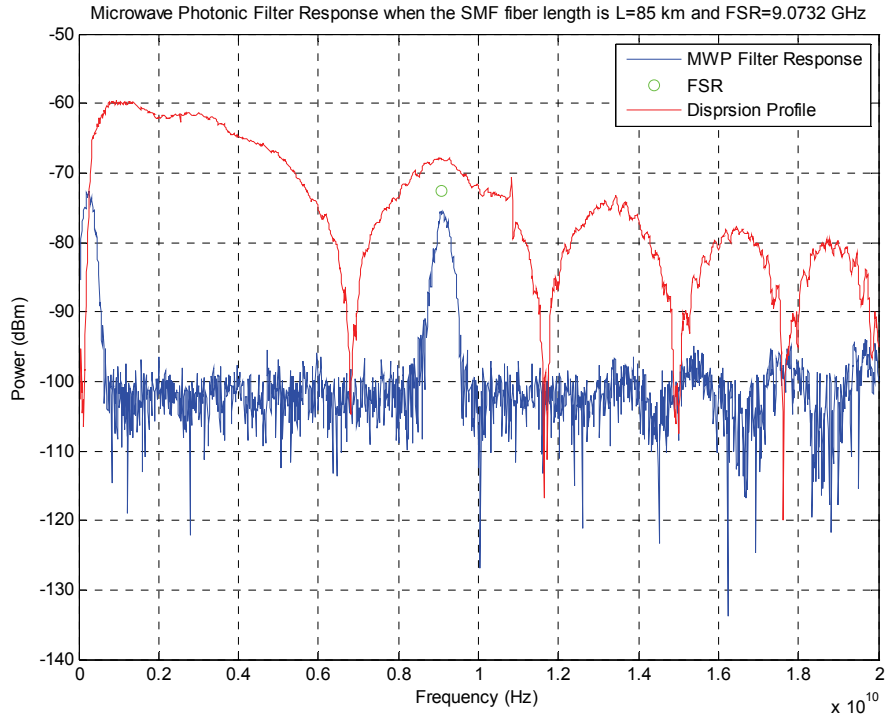


Figure 4.8: MPF response superimposed on the dispersion response of the SMF fiber of length 85 km used as delay line.

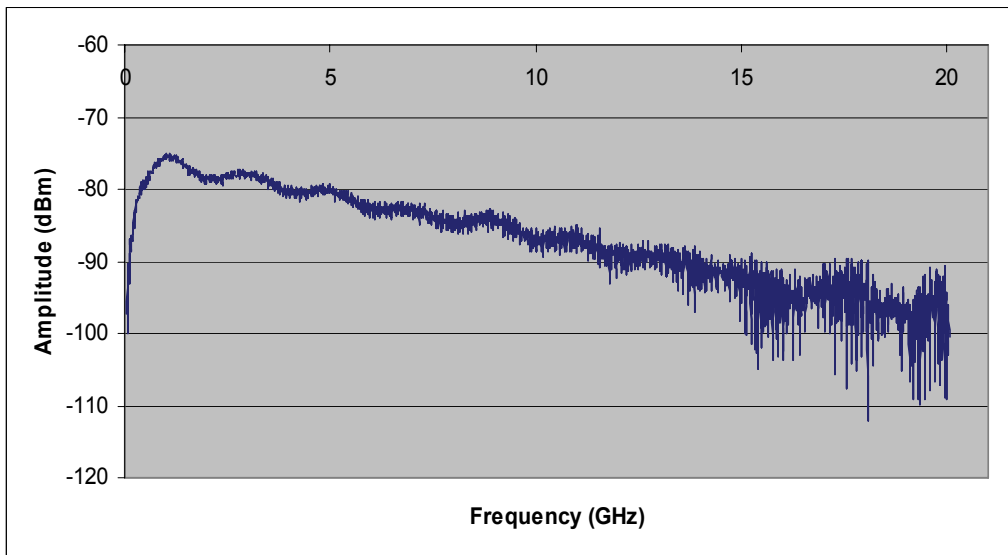


Figure 4.9: Measured modulator transfer function over 20 GHz of RF frequency.

4.4.3 Temperature Measurement Using a MPF System

The experimental setup used to obtain the MPF based interrogation system for temperature change monitoring is shown in Figure 4.10. Light from a BBS is sliced using reflection off the FBG pair. The resulting multi-wavelength source is sent to a modulator using the RF frequency from a LCA as modulating signal. The modulated optical signal is amplified before it is sent to an 85 km length of SMF fiber, which acts as the dispersive medium (delay component) of the MPF system. Amplification before the fiber is necessary to avoid information loss due to attenuation over such a long fiber distance. The RF signal is swept over a 20 GHz frequency span, so the LCA displays the detected electrical signal, which is obtained after the output to the 85 km SMF passes through a photo-detector.

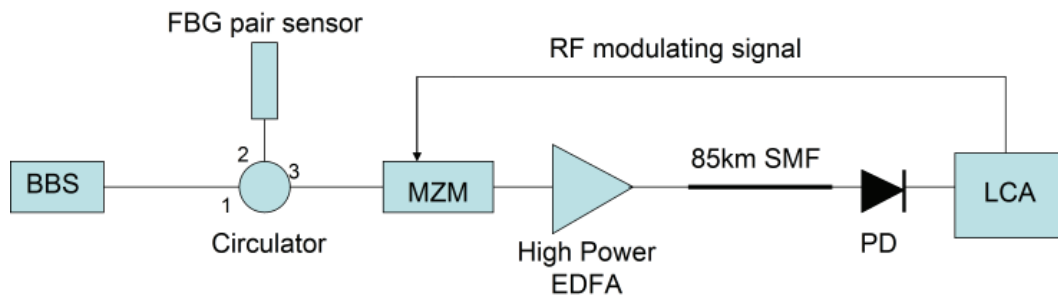


Figure 4.10: MPF experimental setup.

First, the LCA was used to measure the filter response at room temperature. Then, the sensor was immersed into the kettle where water was boiled, and the temperature was measured using a thermometer. Next, a measurement of the MPF was performed. The process was repeated for subsequent lower temperatures, at temperatures spaced by 10 °C, for a range from 80 to 40 °C. The MPF shift is shown in Figure 4.11. As predicted by theory, the filter peak moves toward lower frequencies. Also, biasing the modulator at a fixed RF frequency causes the measured power to change with increasing temperature as follows: if the modulating frequency corresponds to a value on the rising edge of the filter, the power measurement increases with increasing temperature. This is shown in Figure 4.12. On the other hand, if the modulator is modulated with an RF frequency value on the falling edge of the filter, the measured power decreases with increasing temperature, and this is illustrated in Figure 4.13. As observed in Figures 4.12 and 4.13,

sensitivity increases as the bias point approaches the edges of the filter. However, this imposes a limit on the range of temperatures that can be measured using this measurement configuration. Thus, when choosing the bias frequency, the trade-off between sensitivity and measurement range must be considered. For example, the frequency of modulation can be set at a value located at the midpoint on either the rising or the falling edges of the filter response.

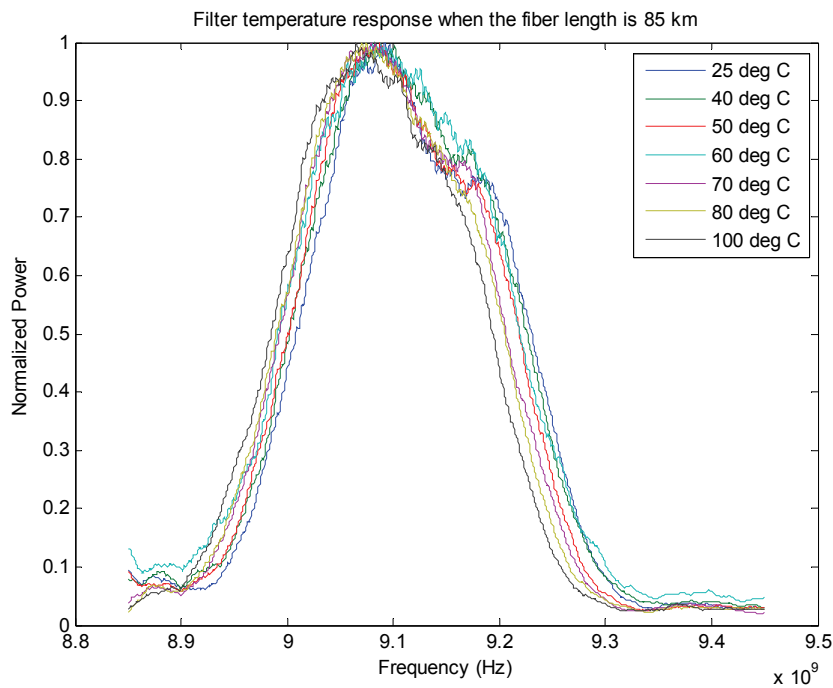


Figure 4.11: Shift in the MPF as temperature is increased from 25 to 100 $^{\circ}$ C.

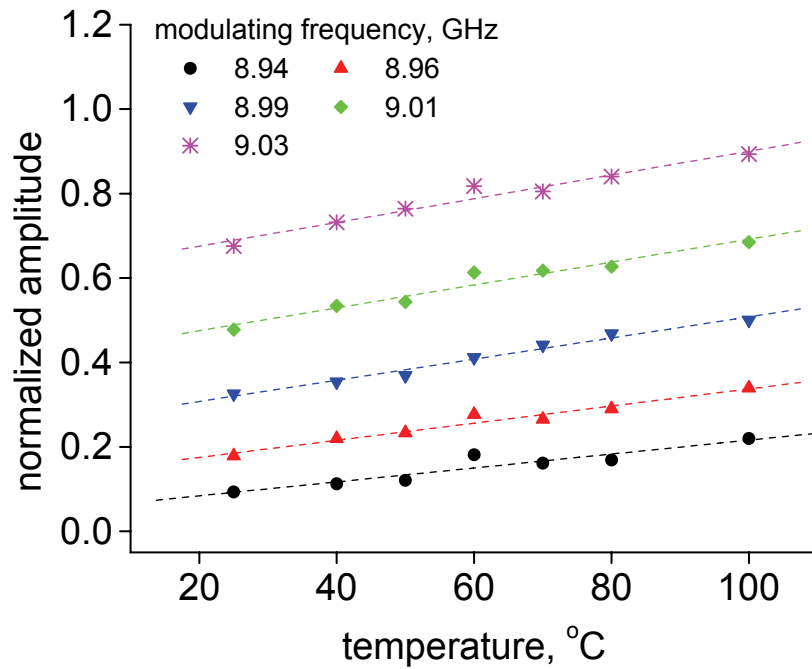


Figure 4.12: Graph of power measured as temperature is increased for different modulator RF bias frequencies located on the rising edge of the second filter peak.

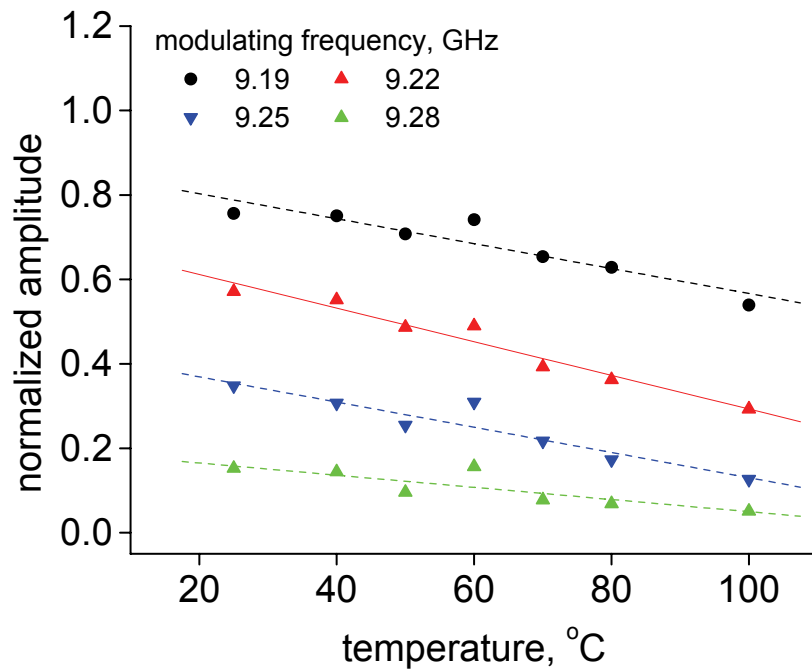


Figure 4.13: Graph of power measured as temperature is increased for different modulator RF bias frequencies located on the falling edge of the second filter peak.

When setting the RF frequency is at 8.98 GHz (rising edge), the observed sensitivity is 0.0024 /°C. On the other hand, choosing the bias frequency at 9.24 GHz, the sensitivity is -0.0036 /°C. This can be observed in Figures 4.14 and 4.15, which illustrate the plot of normalized power as a function of temperature graphs when the modulator is biased at 8.98 GHz and 9.24 GHz, respectively. Note that the normalized power was used to account for the power fluctuation that may have resulted from alternating spectrum and MPF response measurements.

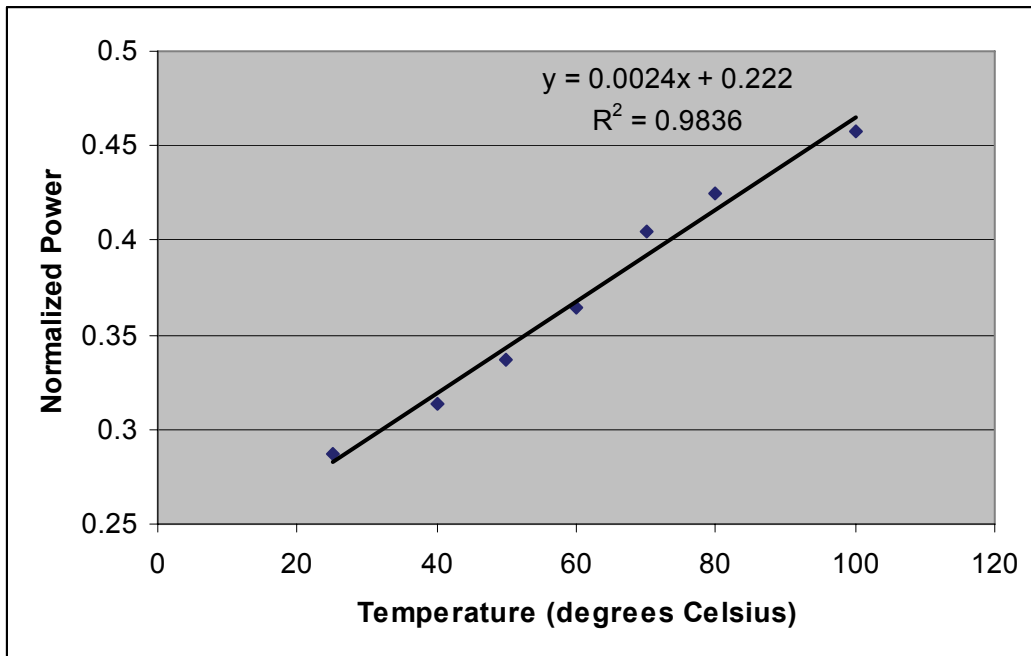


Figure 4.14: Graph of normalized power variation as a function of temperature when the bias RF frequency is 8.98 GHz.

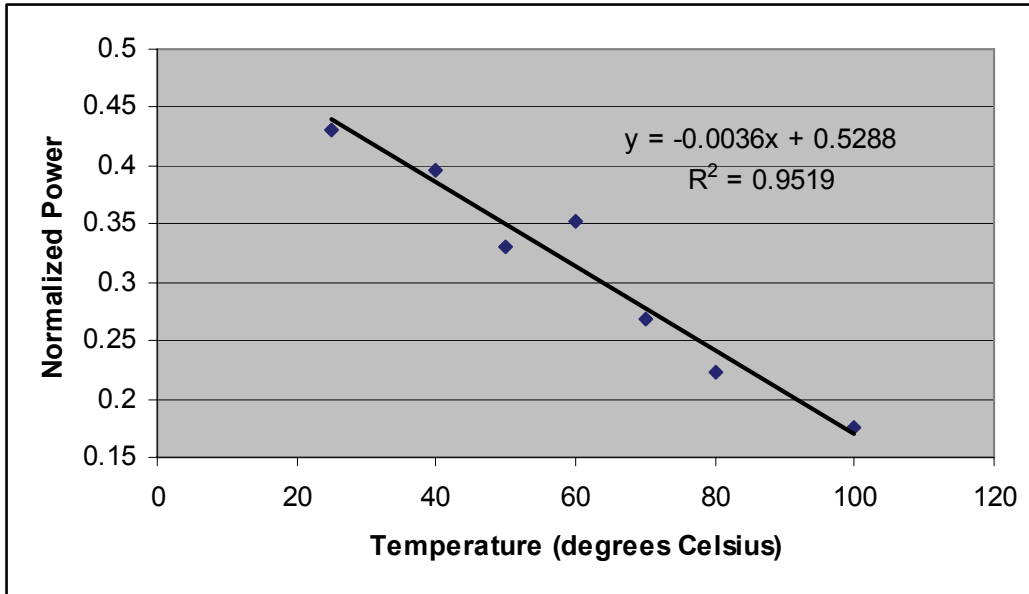


Figure 4.15: Graph of normalized power variation as a function of temperature when the bias RF frequency is 9.24 GHz.

4.5 Conclusion and Discussion

As presented, the proposed interrogation system takes advantage of the MPF systems' ability to translate the response of a multi-wavelength source in the optical domain to a filtering variation in the microwave domain to monitor the changes in the spectral response of an FBG pair. This experiences a sinusoidal response, which gives the MPF a single passband filtering variation. Moreover, the interrogation system allows tailoring the sensitivity and the operability range to satisfy the requirements of different applications. However, using an 85 km long SMF as delay medium involves increased losses and the need to use additional amplifiers, which add noise to the system. At the same time, such lengths of fiber make the system bulky and unpractical. One solution would be increasing the multi-wavelength fringe separation, which can be achieved by decreasing the FBG separation. Also, using fibers of increased dispersion can allow for the use of more compact fiber based delay media. In terms of demodulation method, since the system is based on power measurement, the outcome is dependent on power fluctuations. Also, as discussed, carrier suppression influences the amplitude variation of the MPF. This may induce changes in the amplitude of the peak power, which has the same effect as power fluctuation. Therefore, future work may include a power fluctuation compensation method, such as normalization, which was used to assess the effect of temperature (as in the experiment) or strain on the change in the filter peaks separation.

4.6 References

- [4.1] J. Capmany, J. Mora, B. Ortega, and D. Pastor, "Microwave photonic filters using low-cost sources featuring tunability, reconfigurability and negative coefficients," *Optics Express*, vol.13, no. 5, pp. 1412-1417, 2005.
- [4.2] C. Gouraud, P. Di Bin, L. Billonnet, P. Faugeras, and B. Jany, "Photonic microwave filter using a broadband source sliced by a birefringent optical fiber-based interferometer," *IEEE MTL-S Digest*, pp. 1355-1358, 2003.
- [4.3] J. Capmany, J. Mora, D. Pastor, B. Ortega, and S. Sales, "Microwave Photonic Signal Processing" in *Microwave Photonics: Devices and Applications* by Stavros Iezekiel, Wiley & Sons: Chippenham, Wiltshire, Great Britain, pp. 191-238, 2009.
- [4.4] J. Capmany and D. Novak, "Microwave photonics combines two worlds," *Nature Photonics*, vol. 1, pp. 319-330, 2007.
- [4.5] D. Norton, S. Johns, C. Keefer, and R. Soref, "Tunable microwave filtering using high dispersion fiber time delays," *IEEE Photonics Technology Letters*, vol. 6, pp. 831 – 832, 1994.
- [4.6] M. Y. Frankel and R. D. Esman, "Fiber-optic tunable transversal filter," *IEEE Photonics Technology Letters*, vol 7, pp. 191-193, 1995.
- [4.7] S. Yegnanarayanan, P.D. Trinh, and B. Jalali, "Recirculating photonic filter: a wavelength-selective time-delay for phased array antennas and wavelength code-division multiple access," *Optics Letters*, vol 21, pp. 740-742, 1996.
- [4.8] F. Coppinger, S. Yegnanarayanan, P.D. Trinh, and B. Jalali, "Nonrecursive photonic filter using wavelength-selective true time delay," *IEEE Photonics Technology Letters*, vol. 8, no. 9, pp. 1214-1216, 1996.
- [4.9] F. Coppinger, S. Yegnanarayanan, P. D. Trinh, and B. Jalali, "Continuously tunable photonic radio-frequency notch filter," *IEEE Photonics Technology Letters*, vol. 9, no. 3, pp.339-341, 1997.
- [4.10] J. Mora, B. Ortega, J. L. Cruz, M. V. Andres, D. Pastor, and S. Sales, "Automatic tunable and reconfigurable fiber optic microwave filters based on a broadband optical source sliced by uniform fiber Bragg gratings," *Optics Express*, vol. 10, pp. 1291-1296, 2002.
- [4.11] D. B. Hunter and R.A. Minasian, "Reflectivity tapped fiber optic transversal filter using in-fibre Bragg gratings," *Electronics Letters*, vol. 31, pp. 1010-1012, 1995.
- [4.12] S. Torres, P. Perez-Millan, J.L. Cruz, and M. V. Andres, "Tunable microwave photonic filter based on chirped fiber gratings working with a single optical

carrier at constant wavelength,” *Optics Communications*, vol. 277, pp. 269–272, 2007.

- [4.13] E. Hecht, *Optics*, ed. 4, Addison Wesley: San Francisco, CA, p. 425, 2002.
- [4.14] S. V. Miridonov, M. G. Shlyagin, and D. Tentory, “Twin-grating fiber optic sensor demodulation,” *Optics Communications*, vol. 191, pp. 235-262, 2001.
- [4.15] R. Kashyap, “Principles of Optical Fiber Grating Sensors” in *Fiber Bragg Gratings*, second edition, Academic Press, pp. 441-502, 2010.
- [4.16] Y. Zhao and Y. Liao, “Discrimination methods and demodulation techniques for fiber Bragg grating sensors,” *Optics and Lasers in Engineering*, vol. 41, pp. 1-18, 2002.

5. Improved Arrayed Waveguide Grating-based Interrogation System for Fiber Bragg Grating Sensors

5.1 Introduction

FBGs find extensive use for sensing environmental and mechanical parameters. For example, they have been used to measure strain, which is the result of mechanically perturbing the fiber, and temperature and pressure, which characterize the surrounding medium conditions. All these parameters have an effect on the physical and chemical structure of FBGs, which in turn affect the properties of the light that passes through them. In particular, as discussed earlier, strain affects the period of the alternating refractive index structure, with an insignificant effect on the effective refractive index, which, in comparison, changes significantly with temperature. While the sensor response measurement techniques are mature enough, extensive work is invested in minimizing interrogation systems cost and complexity. A method that simplifies sensor interrogation systems is multiplexing, which allows using the same measurement unit to monitor two or more sensors. Given the wavelength-encoded information provided by FBGs, wavelength-division-multiplexing (WDM) plays an important role in achieving multi-sensor monitoring. However, for applications where a large number of sensors are distributed over long distances, avoiding loss of information and measurement errors relies on using high powers at the transmitter end, or alternately, including amplifiers, which add noise and complexity to the overall system. Another important aspect in the measurement of FBG-based sensor systems is the portability of the detection instrumentation. In general, wavelength-encoded information involves using OSAs. To avoid using such bulky and expensive instruments, mapping wavelength information to power quantities has been widely explored. This can be achieved using any filtering device whose amplitude varies with wavelength, i.e., an edge filter. The basic mapping principle is shown in Figure 5.1 [5.1], where a linear edge filter was used for the purpose of illustration. As observed, the portion of the FBG spectrum that overlaps with the filter spectrum is transmitted. Also, as wavelength changes, the amplitude of the filter increases or decreases, and this affects the amplitude of the measured spectrum. Consequently, the measured power changes, and this leads to the ability to detect the

wavelength change using a power meter, which is less expensive and is more compact. In practice, an edge filter is achieved using any device whose spectrum has an increasing or a decreasing variation with wavelength. For example, another FBG in transmission mode can be used: either its rising or its falling edge can perform as the mapping element to demodulate the wavelength change response of the FBG under test. The same way, as previous work shows, a long period grating can be used because it shows a filtering response in transmission mode only.

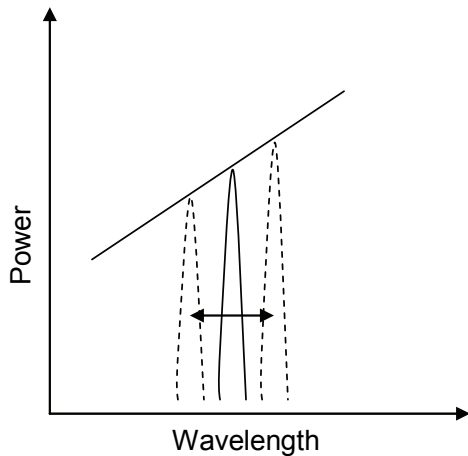


Figure 5.1: Principle of mapping wavelength to power using an edge filter [5.1].

Studies show that AWG channels can be used as edge filters to achieve mapping the FBG wavelength-encoded information to power quantity [5.2-5.6]. The methods proposed have in common the use of the ASE from an amplifier as BBSs to extract the spectral information of a number of FBGs. Then, spectrum reflecting off each FBG is sent to one, and distinctive, AWG channel to achieve wavelength to power mapping. In this chapter, starting from the aforementioned work, we propose providing the system with a feedback mechanism to achieve a lasing configuration. In this chapter we prove that this system achieves improved measurement performance with enhanced power efficiency. For this purpose, we compared both systems in terms of power efficiency and mapping capabilities. Moreover, we explored the effect of using different fiber laser configurations, and we observed the effect of changing the broadband source, which in this case also acts as the amplifying medium of the fiber laser interrogation system. In particular, the comparison of using a semiconductor optical amplifier (SOA) and an EDFA both as broadband sources and as gain media will be provided.

5.2 Fiber Laser Systems

Fiber laser systems find application in many areas because they can be implemented from readily available components such as optical amplifiers, optical filters, couplers and optical fibers. The two basic designs that are generally used to achieve fiber laser systems are the linear cavity (standing wave) and the ring configurations, which are shown in Figures 5.2a) and 5.2b), respectively. The basic components are amplifiers (one or a cascade of amplifiers), which acts as the amplifying medium of the lasing system, a filter, which is used to select the wavelength of the laser light emitted, and a positive feedback mechanism. In the standing wave configuration, the feedback is achieved by placing the amplifier and the filter between two reflective components. These may be in-fiber reflectors, or external reflectors. For the latter, partial or total reflective components covering a wide range of wavelengths can be used, and various methods have been used to obtain in-fiber reflectors. For example, wideband FBGs written in the core of optical fibers can act as reflectors. Note that the system does not need an external source because lasing is triggered by the ASE from the amplifier. This is similar to a conventionally built laser: the first photon is emitted through spontaneous emission, which is regarded as a process generating noise photons [5.7].

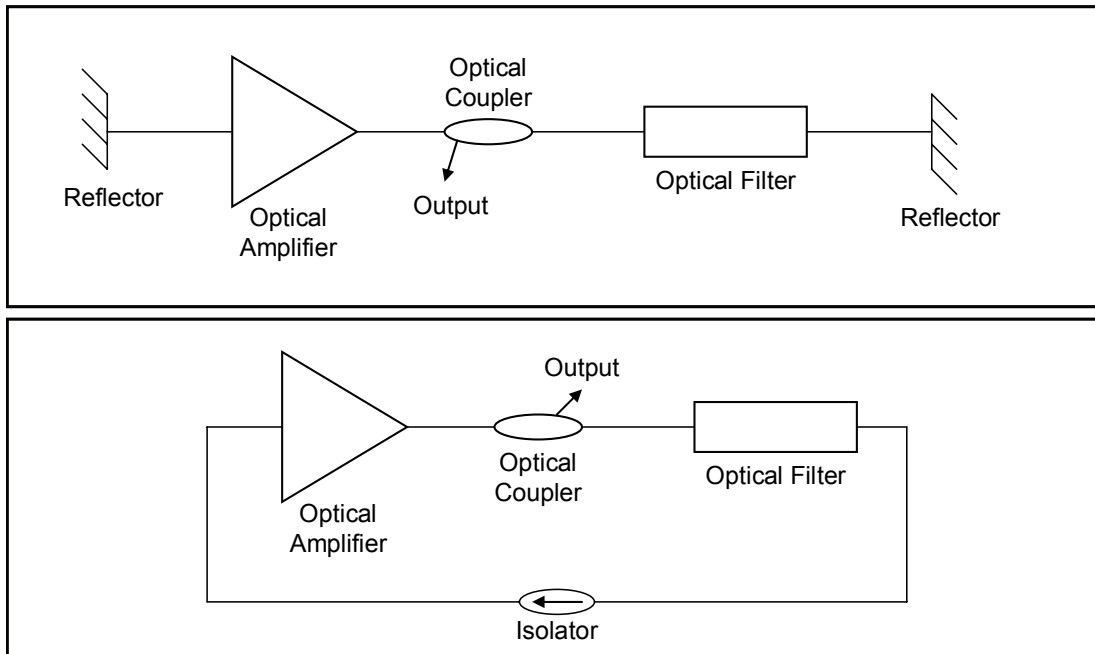


Figure 5.2: Fiber laser configurations: a) standing wave configuration; b) ring configuration.

The fiber laser can be made tunable by using tunable filters. For example, when used as filters, FBG's center wavelength can be tuned by either changing temperature, or by applying strain to the periodic structure. Also, tunable FP filters have been used as tuning element in fiber lasers. For example, in [5.8], a tunable Fabry-Perot filter uses the change in mirrors separation distance to set the lasing wavelength. However, in-fiber filters are more attractive because they offer the fiber compatibility advantage, which leads to a decrease in coupling losses [5.9]. Thus, FBGs, with their wavelength selectivity property, play an important role in defining the wavelength operation in fiber laser system. Moreover, given their sensitivity to temperature and strain, FBGs have been investigated in the context of building tunable fiber laser systems. The possibility to tailor their spectrum characteristics made them useful in a number of applications useful for WDM-based systems.

Since FBG-based sensor systems employ the WDM technology to improve measurement efficiency, FBG-based fiber laser systems have been extensively investigated. For example, in [5.10] and in [5.11] sampled FBGs are used to achieve lasing at two wavelengths in an EDFA-based fiber laser. Moreover, as presented in [5.12] combining FBGs in cavity structures has also been proven useful to obtain multi-wavelength operation when EDFAs are used as fiber laser gain media. As discussed in these works, this is difficult to achieve owing to rare earth doped fiber media's homogeneous spectral broadening at room temperature, which increases mode competition [5.13]. Nevertheless, EDFAs are desirable amplifying media because they offer high gain, high saturation power, and its gain is highly independent of polarization [5.14]. On the other hand, other amplifiers capable of triggering multi-wavelength operation in fiber laser systems have been explored, and SOAs are part of the amplifying devices that are characterized by inhomogeneous spectral broadening, which allows multi-wavelength fiber laser operation [5.15]. SOAs also offer low power consumption, they are compact and can be produced in large quantities [5.16]. In the context of using fiber lasers as interrogation systems for FBG-based sensors, in [5.17] S. Tanaka *et al.* proposed using a fiber laser ring system to monitor the response of FBG vibration sensors. In this case, the fiber laser serves as the source used to measure the vibration sensors' response.

As mentioned before, in this experiment the FBGs act as the filter elements, which are used to select the lasing wavelengths, for both the standing wave and the ring configurations, and as one end partial reflectors for the former. It is expected that the lasing peaks obtained, which characterize the external factors to be measured, can offer better power efficiency, and, eventually, better measurement resolution, which depends on the linewidth of the laser modes. As presented by N. Voo *et al.* in [5.18], in a fiber laser system, the linewidth is inversely proportional to the laser output power (P), and directly proportional to the original linewidth of the wavelength selective element $\Delta\nu_{filter}$, i.e., the linewidth is defined by Schawlow-Townes as

$$\Delta\nu = \frac{2\pi\hbar\nu(\Delta\nu_{filter})^2}{P} \quad (5.1)$$

where ν is the frequency of the lasing wavelength. This phenomenon is observed in cavities and results from the effect spontaneous emissions have on the phase of the laser [5.18].

5.3 AWGs as Edge Filter Components

AWGs are passive fiber optic compatible structures frequently used in WDM systems for filtering, add/drop multiplexing, or laser stabilizers [5.19]. These applications take advantage of AWGs' multi-channel wavelength-selective properties, which can be observed in the basic physical structure of an AWG illustrated in Figure 5.3. As observed, light is coupled into a receiving waveguide, and different wavelength components are directed and coupled to a number of output waveguides. The wavelength division of the input light is achieved by passing the signal through a free propagation region (FPR) before being coupled to a set of waveguides of different special lengths. These are chosen so the difference between the optical path lengths (OPL) of two adjacent channels is proportional to the center wavelength λ_c of the AWG, i.e.,

$$n_{eff}\Delta L = m\lambda_c \quad (5.2)$$

where n_{eff} is the effective refractive index inside the AWG waveguides, ΔL is the length difference between adjacent channels, and m is an integer number that denotes the order of the array. [5.20][5.21]. Two signals traveling inside waveguides of different spatial

lengths experience different phase changes, whose difference determines the nature of the filter, i.e., if the phase difference $\Delta\phi$ is 2π , the AWG is periodic, with the FSR given by $\frac{\nu_c}{m} \left(\frac{n_{eff}}{n_g} \right)$, where ν_c is the center frequency of the AWG, and n_g is the group index of the FPR. The purpose of having different lengths for the array waveguides is to bend the output beams so they can be coupled through an output FPR to different output waveguides [5.21].

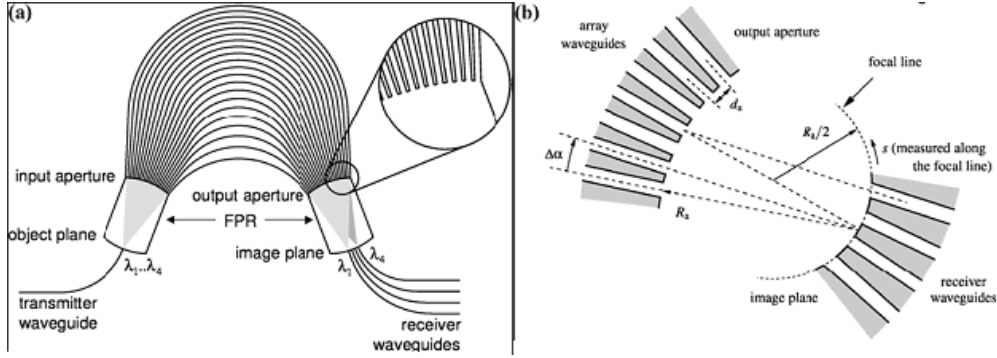


Figure 5.3: (a) AWG geometric structure; (b) Geometric representation of the FPR.

Equation (5.2) predicts that the optical path length difference dependence on temperature provides a method for tuning the wavelength slicing properties of AWGs. This property and the multi-channel characteristic of AWGs have been used for wavelength interrogation of an array of multiplexed FBGs. For example, in [5.20], to measure wavelength change for an FBG, the detection AWG was temperature tuned to achieve the overlap between the centers of one of its channels with the center of the reflection spectrum of the sensor. However, this method relies on wavelength decoding, which involves external tuning and adds complexity to the interrogation system. Previous studies propose taking advantage of the wavelength Gaussian shape of the AWG spectrum, which is imposed by the mode profiles of the array waveguides, to achieve a power measurement-based interrogation of FBGs. The principle behind the operation of such system is the change in the overlap between the AWG and the FBG spectra, as the sensor's wavelength changes. The power resulting from the overlap of the two spectra can be expressed mathematically as
$$P = (1 - \alpha) \int_0^{\infty} I_s(\lambda) R_{FBG}(\lambda) T_{AWG}(k, \lambda) d\lambda$$

(5.3)

where α is the amount of attenuation, $I_s(\lambda)$ is the intensity of the input signal,

$$R_{FBG}(\lambda) = R_0 \exp\left[-\frac{(\lambda - \lambda_{FBG})^2}{2\sigma_{FBG}^2}\right] \quad (5.4)$$

is the reflection transfer function of the sensing FBG of center wavelength λ_{FBG} and of bandwidth

$$\sigma_{FBG} = \frac{FWHM}{2\sqrt{2\ln 2}} \quad (5.5)$$

$$\text{and } T_{AWG}(k, \lambda) = T_0 \exp\left[-\frac{(\lambda - \lambda_k)^2}{2\sigma^2}\right] \quad (5.6)$$

is the transmission transfer function of the k th AWG channel of center wavelength λ_k and of full width at half maximum (FWHM) σ . In equations (5.4) and (5.6), R_0 and T_0 are the reflectivity of the FBG and the transmission function of the AWG channel, respectively [5.19]. As a result, within the same AWG channel, a change in the FBG center wavelength results in a change in the measured power levels at the output of the AWG. As an example, [5.4] proposes an interrogation system based on sweeping of the center wavelength of FBGs with temperature across an AWG channel, and monitoring the output power measurement. On the other hand, in [5.19], the AWG center wavelength is first tuned to have the sensing FBG overlap with two adjacent channels. As the center wavelength of the FBG changes, the amount of overlap with one channel changes relatively to the overlap with the other channel. Therefore, the power ratio between the two channels changes accordingly. When using the AWG as an edge filter for wavelength-to-power mapping, it is important to consider the wavelength measurement error, which is defined as

$$\Delta\lambda = \sqrt{(A_1^2 + A_2^2)C} \quad (5.7)$$

where A_1 and A_2 are the bandwidths of the AWG and of the FBG spectra, respectively, and C represents the fluctuation intensity [5.3]. Therefore, since the AWG channel bandwidth is kept constant, any method that can decrease the FBG spectrum bandwidth can improve the measurement accuracy.

5.4 Experimental Setup and Measurement Method

The setup in Figure 5.4 was proposed as the conventional method to achieve wavelength to power mapping to measure the response of FBGs that are subject to different strains or temperatures—both processes involve a shift in the Bragg wavelength. Figures 5.5 and 5.6 show, respectively, the standing wave and the ring fiber laser configurations used to achieve improved wavelength to power mapping. Here, as mentioned before, the broadband light is the ASE from an optical amplifier. As a result, if light is fed back into the device, amplification is achieved. Therefore, in this case the source has two roles: to provide the broadband light which is sliced by the sensing FBGs, and to amplify the light that is fed back through the amplifier. This method thus reduces the number of components used in the system. For most amplifiers, the gain distribution is polarization dependent, and, thus, the systems in Figures 5.5 and 5.6 use polarization controllers to achieve optimum gain distribution. Note that the circulator used in the system in Figure 5.4 can be replaced by a 3 dB coupler to achieve direct performance comparisons of the conventional with the standing wave and with the ring fiber laser systems. Also, for the ring configuration in Figure 5.6, the circulator is used to ensure unidirectional signal propagation inside the ring.

As discussed earlier, fiber laser systems require a mode selection element that defines the wavelength of the light emitted by the laser. This is usually achieved using an optical filter. Since in reflection mode FBGs act as narrowband filtering elements, multi-wavelength lasing can be obtained when using the sensing FBGs. For experimental purposes, the four FBGs in Figures 5.4 to 5.6 were used as strain sensors. The FBGs were written on separate fibers and linked in series using connectors. For the FBGs numbered from 1 to 4, the Bragg wavelength distribution is as follows: 1536.40 nm, 1538.32 nm, 1540.03 nm, and 1554.12 nm with bandwidths of 200 pm, 220 pm, 230 pm, and 70 pm, respectively. For the AWG in Figures 5.4, 5.5 and 5.6, the channel spacing is 100 GHz at 1550 nm with spectrum bandwidth of 400 pm.

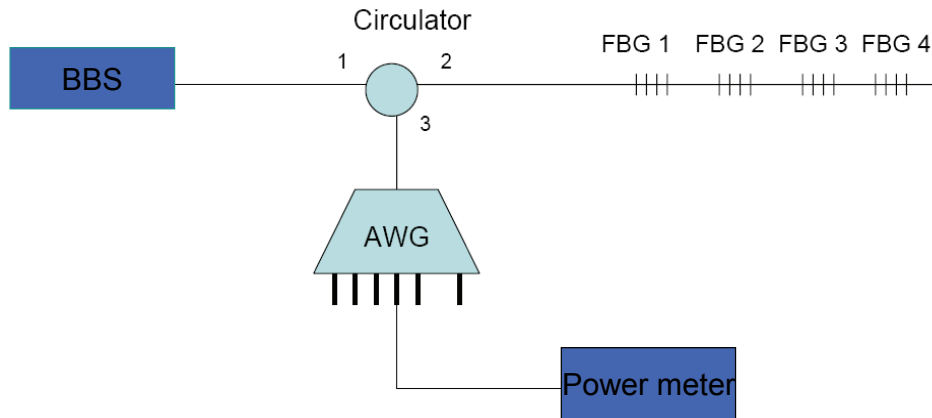


Figure 5.4: Conventional wavelength to power mapping system.

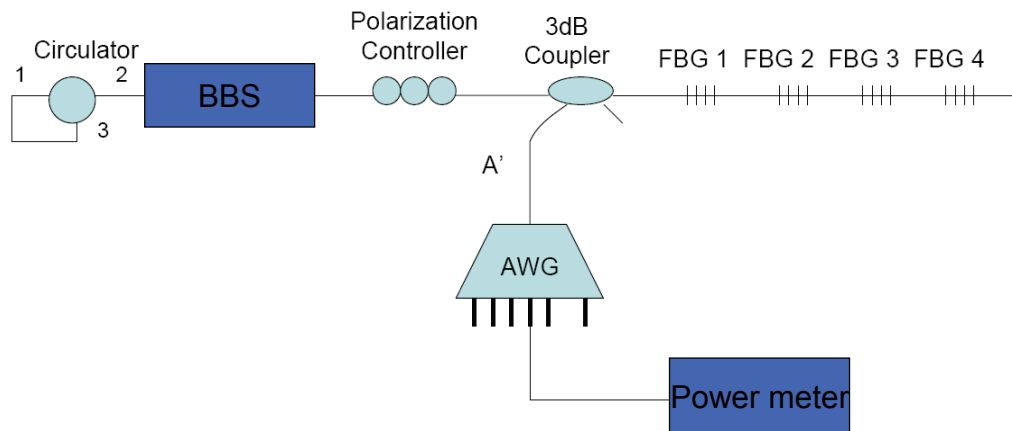


Figure 5.5: Standing wave fiber laser system used to achieve wavelength to power mapping.

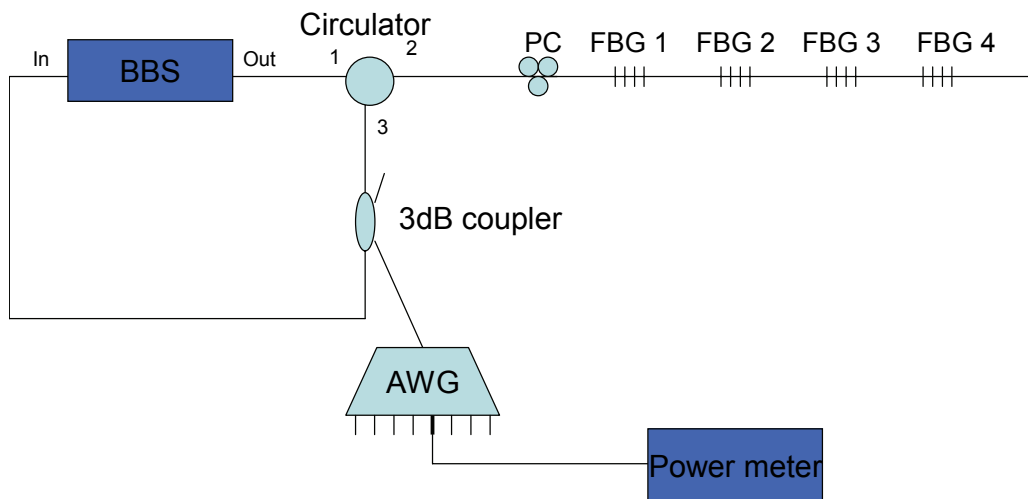


Figure 5.6: Ring fiber laser system used to achieve wavelength to power mapping.

Figure 5.7 illustrates the mechanism used to apply strain to the FBG in a controlled and quantitative manner. The fiber was pivoted and clamped at two ends: one is fixed, and the other is free to glide (moveable end). Each clamp consists of two metal slides, with the bottom one being fixed to the elongation system's table. Using screws, the top slide can be pasted unto the former to hold the fiber in place at the pivoting points. For protection purposes, the fiber was placed between two polymer sheets before being clamped between the metal slides. Rotating the knob in the clockwise direction causes a metallic cylindrical piece to push the moving pivotal end toward the fixed end. This makes the fiber relax, i.e., no strain is applied to the fiber. Changing the direction of the knob's rotation has the opposite effect, i.e., the moving pivotal end moves away from the fixed end, resulting in the fiber being elongated, and thus strain is applied to the FBG. The Vernier scale provided is chosen such that, when the knob is rotated by 50 units, the moving pivotal piece changes position by 0.5 mm. As a result, the fiber is elongated by 10 μm in one rotational unit. To find the zero strain point, a calibration measurement is performed for each FBG. As such, the spectrum of each FBG is monitored using an optical spectrum analyzer, and its center wavelength is recorded every Vernier unit over a certain range. From the plot of FBG reflection spectrum center wavelength as a function of Vernier reading, the linear variation of the curve is extrapolated, and this leads to finding the zero strain position. The elongation of the fiber (ΔL) can be obtained by subtracting the zero strain point from subsequent readings. Then, the strain (ε) is calculated by taking the ratio of the fiber elongation to the entire length of fiber placed between the pivotal points of the strain system L , which is the sum of the FBG length and the surrounding fiber length, i.e., $\varepsilon = \frac{\Delta L}{L}$ [5.22]. The plot of wavelength as a function of strain represents the calibration curve for the wavelength to power mapping process.

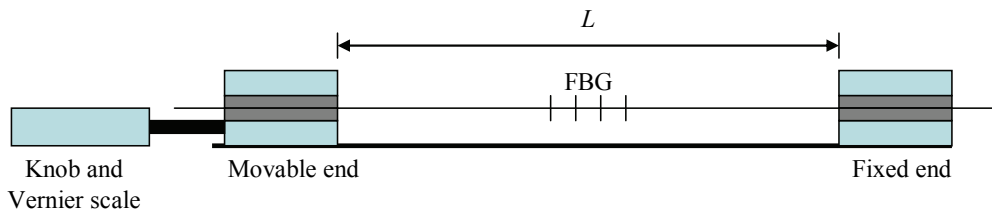


Figure 5.7: Mechanism to apply and measure strain.

Next, the signal reflected off the FBGs was connected to the AWG input, and the power was measured at the output of the channels that overlapped with one of the FBG spectra. As the fiber is strained and the reflection spectrum of an FBG moves towards longer wavelengths, the amount of FBG-AWG spectrum overlap and thus the power level change. Therefore, for each of the systems in Figures 5.3 through 5.5, the plot of power as a function of strain was obtained. Then, the linear calibration curve allowed the one to one mapping of the power as a function of strain to the power as a function of wavelength curve.

5.5 Experimental Results

5.5.1 Using an SOA as Broadband Source

A first experiment performed involves using the ASE from a SOA as the broadband source to the systems in Figure 5.4. For the fiber laser systems in Figures 5.5 and 5.6, as mentioned before, the SOA plays both the role of broadband source sliced by the sensing FBGs and of gain medium. For the SOA used (COVEGA 1117), the ASE power used is 1.16 mW at a driving current of 350 mA. The FBGs spectra for the conventional (non-lasing) system, for the standing wave fiber laser configuration, and for the ring fiber laser configuration are shown in Figures 5.8, 5.9, and 5.10, respectively. Compared to the former configuration, for the fiber laser systems, the main observation is that, as expected, when the lasing characteristic is achieved, the peak powers increase. For example, using the standing wave fiber laser system results in a peak power amplification by 30 to 35 dB for FBGs 1 to 3, and by 45 dB for FBG 4. With the ring fiber laser configuration, the gain can reach 40 dB (for example, for FBG 2). Moreover, the 3 dB level bandwidths decrease for the FBG spectra: as observed in Figures 5.8 to 5.10, the standing wave configuration leads to a reduction in 3 dB bandwidth of about 100 pm or more for FBGs 1 to 3 and of 20 pm for FBG 4. Note that according to Equation (5.7), the reduction in FBG bandwidth leads to a reduction in the error of measuring the wavelength shift associated with a certain change in power measured at the output of the AWG. For example, assuming that $C=1$ and that the AWG channel bandwidth is 400 pm, when the conventional wavelength-to-power mapping system is used, the wavelength measurement errors for FBG number 1 is 447 pm. However, when the standing-wave and

the ring fiber laser configurations are used, the errors are 413 pm and 411 pm, respectively. These are smaller than the error obtained when using the non-lasing configuration. The same tendency is observed in Table 5.1, which includes the measurement errors for the other three FBGs. Moreover, the power level enhancement allows multiplexing a number of sensors over large distances.

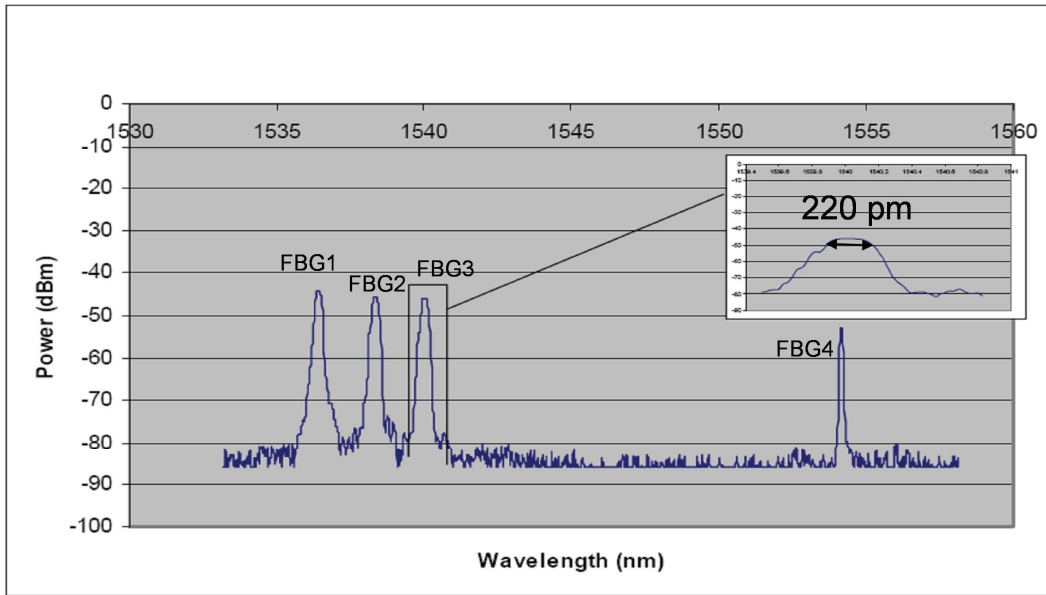


Figure 5.8: FBG reflection spectra for the conventional wavelength to power mapping system.

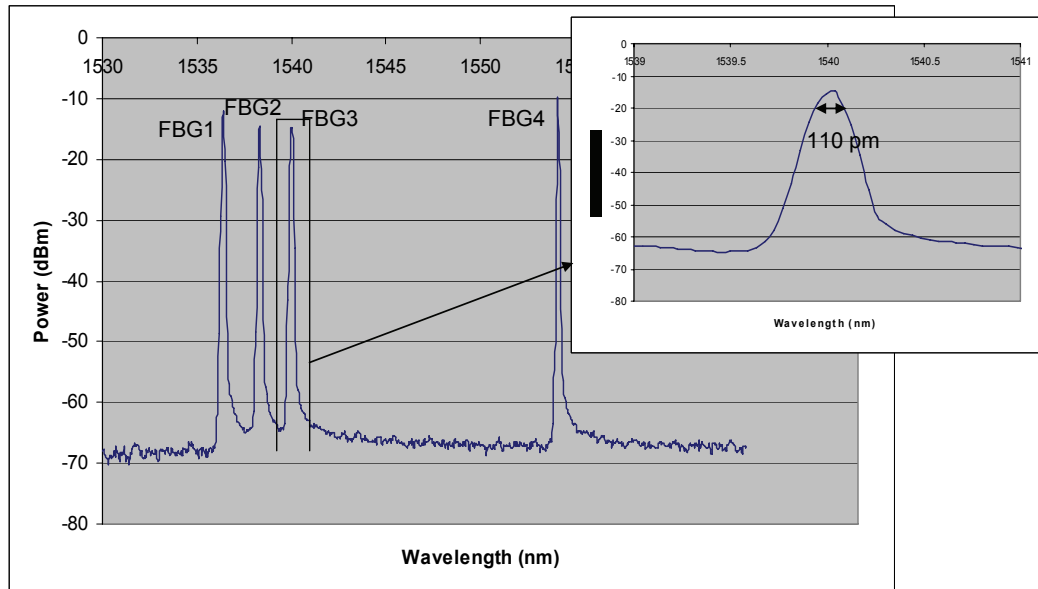


Figure 5.9: FBG reflection spectra for the standing wave fiber laser wavelength to power mapping system.

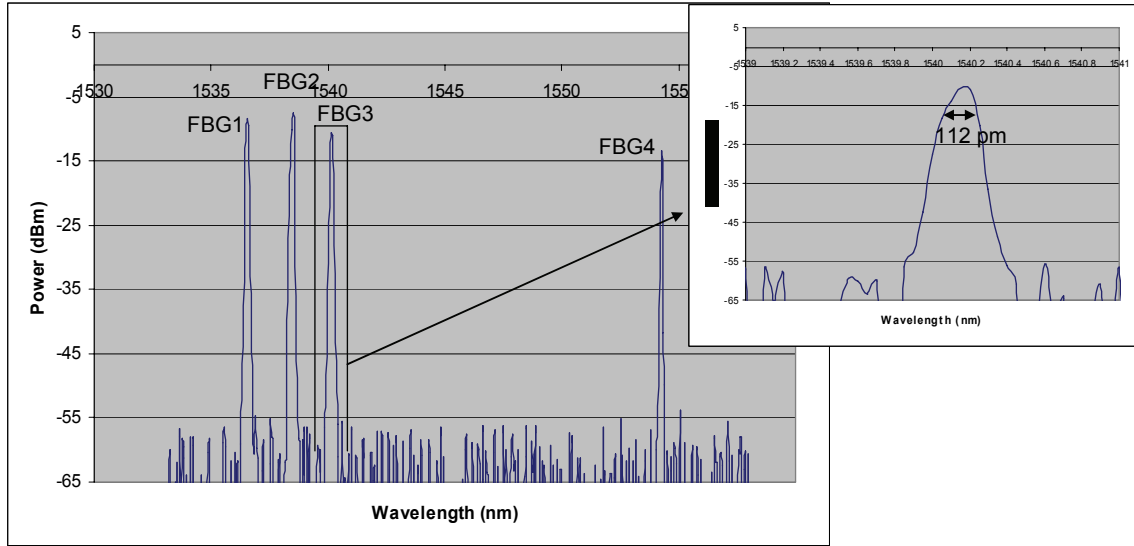


Figure 5.10: FBG reflection spectra for the ring fiber laser wavelength to power mapping system.

Table 5.1 summarizes the bandwidth change for the FBGs when using the two lasing systems and the conventional mapping system.

Table 5.1: Summary of FBG reflection spectra measured bandwidths with the associated wavelength measurement errors.

FBG no.	Center Wavelength (nm)	Non-Lasing		Standing Wave		Ring	
		3dB BW (pm)	Error (pm)	3dB BW (pm)	Error (pm)	3dB BW (pm)	Error (pm)
1	1536.40	200	447	106	413	96	411
2	1538.32	220	456	121	418	104	413
3	1540.03	230	461	110	415	112	415
4	1554.12	70	406	54	404	40	402

For the SOA based interrogation systems, the curve that led to finding the zero strain point corresponding to the strain mechanism used and the calibration curve for the FBG with reflection spectrum centered at 1538.32 nm are shown in Figures 5.11 and 5.12, respectively.

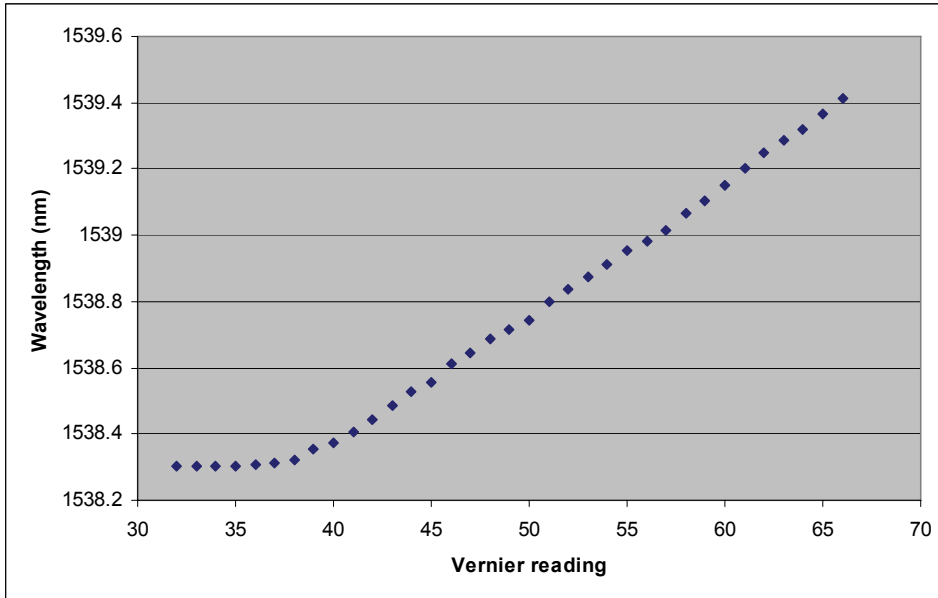


Figure 5.11: Curve used to extract the zero strain point for the FBG whose reflection spectrum is centered at 1538.32 nm.

The measured sensitivity of the wavelength shift with applied strain, which is found by taking the slope of the calibration curve in Figure 5.12, is 1.06 pm/ μ strain and matches the approximate sensitivity of 1.15 pm/ μ strain usually obtained for silica FBGs at 1550 nm [5.23]. Table 5.2 shows that this value is close to the measured sensitivities of all four FBGs used in the experiment.

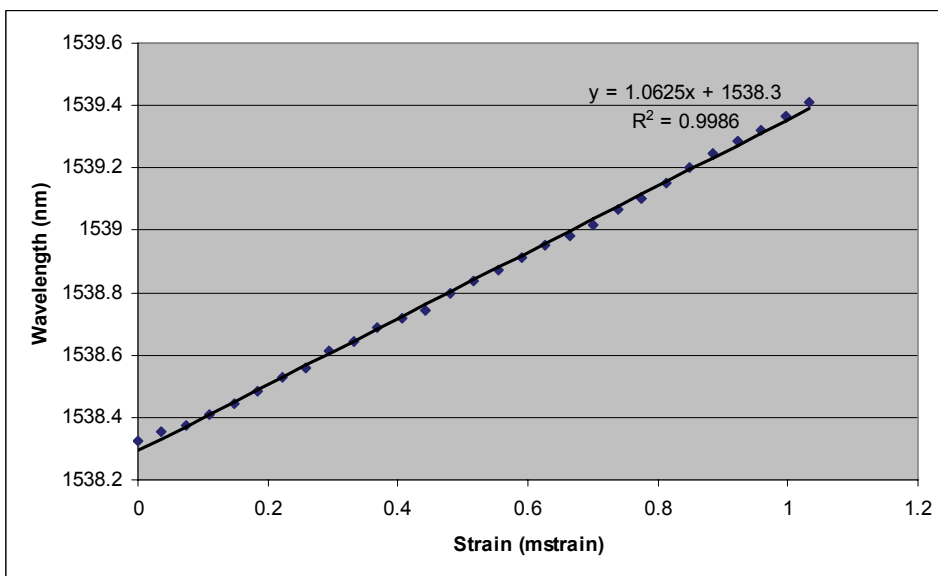


Figure 5.12: Calibration curve for the FBG whose reflection spectrum is centered at 1538.32 nm

Table 5.2: Summary of FBGs sensitivities to strain.

FBG no.	Center Wavelength (nm)	Strain Sensitivity (pm/ μ strain)
1	1536.40	1.02
2	1538.32	1.06
3	1540.03	0.87
4	1554.12	1.29

For the FBG centered at 1538.32 nm, the measured power at the output of its corresponding AWG channel as a function of strain is plotted in Figure 5.13. This plot can be used as illustrated as in Figure 5.14, which illustrates how the calibration curve can be used to obtain the power variation with wavelength change.

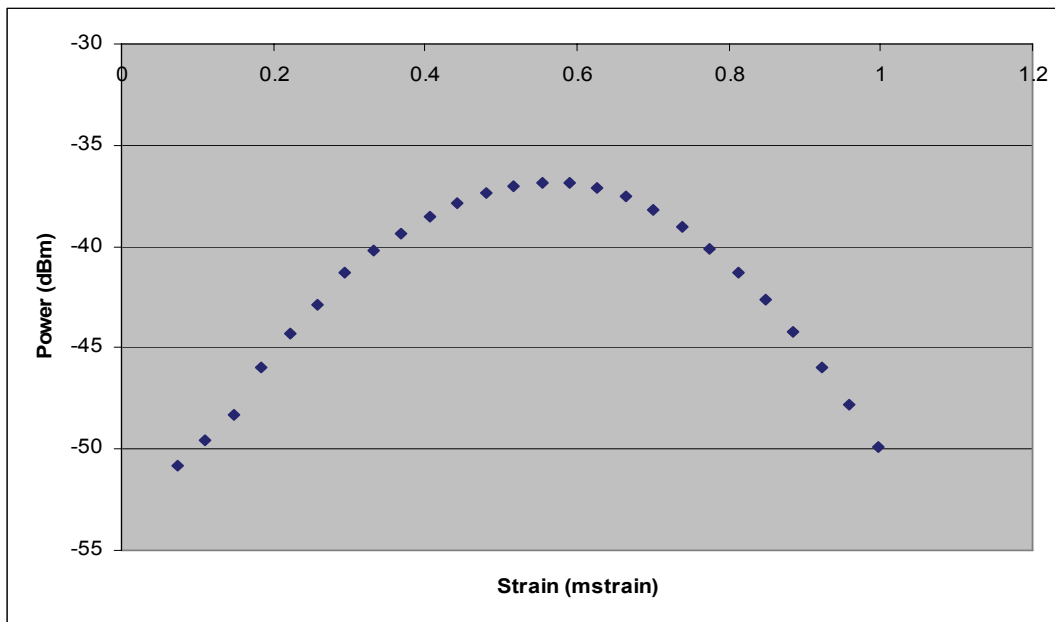


Figure 5.13: Measured power as a function of strain plot.

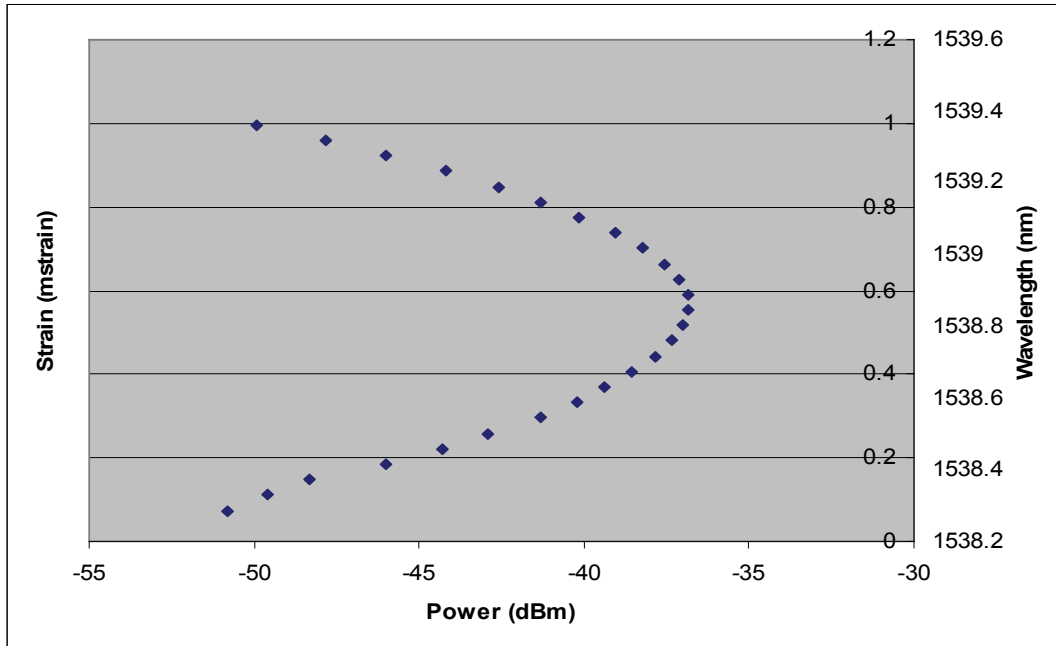


Figure 5.14: Mapping curve showing the wavelength corresponding to the power level measured for different strain levels.

As observed in Figure 5.15, a first advantage of using one of the fiber laser configurations is power enhancement. This is advantageous when using low reflectivity FBGs, for which, after passing through the AWG, the reflected power is too low to be measured using a power meter. In this experiment, the last FBG in the array has the lowest power level; thus, it was not possible to record the power at the output of its corresponding AWG channel. On the other hand, using either the standing wave or the ring configuration, adjusting the polarization controller allows equalizing the peaks. As a result, the sensor of Bragg wavelength at 1554.12 nm experienced the highest gain when the fiber ring interrogation systems were used—this can also be seen in Figures 5.8, 5.9 and 5.10, which show the FBGs spectra for the different measurement systems used.

When contrasting the mapping resolution of the three methods, it is important to consider the system’s sensitivity, which is given by the slope of the almost linear regions corresponding to the falling and to the rising edges of the mapping curve. In this context, the superimposed plot of normalized power as a function of strain in Figure 5.16 shows that on the rising edge of the filtering variation, the ring fiber laser configuration shows the most sensitivity, followed by the measurements made using the standing wave fiber laser system. On the other hand, the falling edge shows that the three systems have about

the same sensitivity. As a result, the main advantage brought about by the use of a fiber laser system in enhanced power efficiency.

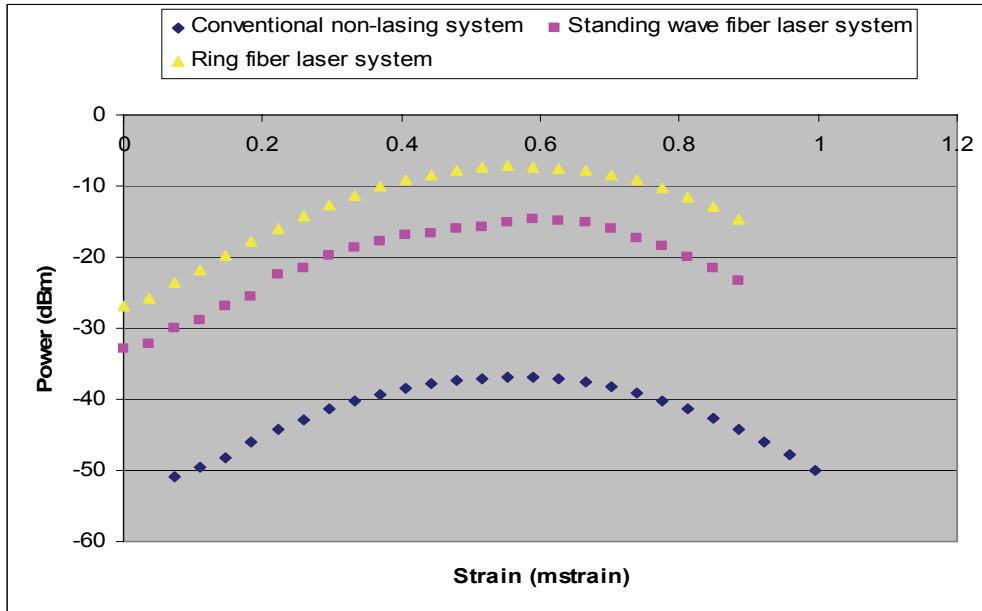


Figure 5.15: Measured power at the output of the AWG corresponding to the FBG of reflection spectrum center wavelength at 1538.323 nm for the three wavelength-to-power mapping systems.

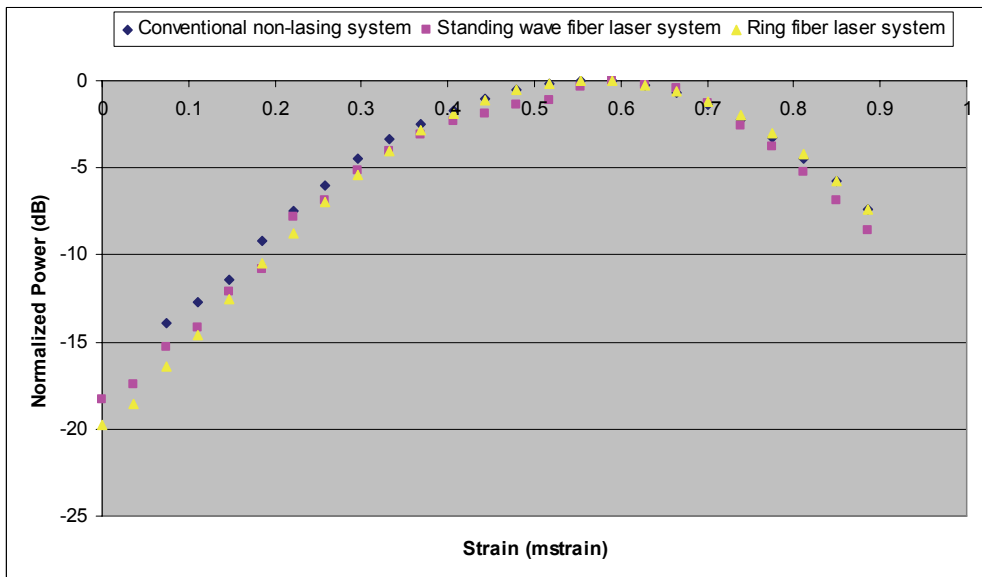


Figure 5.16: Measured normalized power at the output of the AWG corresponding to the FBG of reflection spectrum center wavelength at 1538.32 nm for the three wavelength-to-power mapping systems used to evaluate measurement resolution.

5.5.2 Using an EDFA as Broadband Source

Since, in the absence of an input, the ASE from EDFAs can also be used as broadband sources, the effect of having the SOA replaced by an EDFA in the previous systems was investigated. Commercially available EDFAs include an isolator and thus have unidirectional operation. Therefore they cannot be used in a standing wave lasing configuration, which was achieved by building an in-house EDFA that allows bidirectional propagation. The amplifier block diagram is shown in Figure 5.17: the TEC controller is used to drive the 980 nm pump laser diode. As with the use of an SOA, in the absence of the 1550 nm input, the EDFA output consists of ASE, which can be used as a broadband source. For the measurements, the driving current used was 85 mA, which results in an ASE power of 3.98 mW.

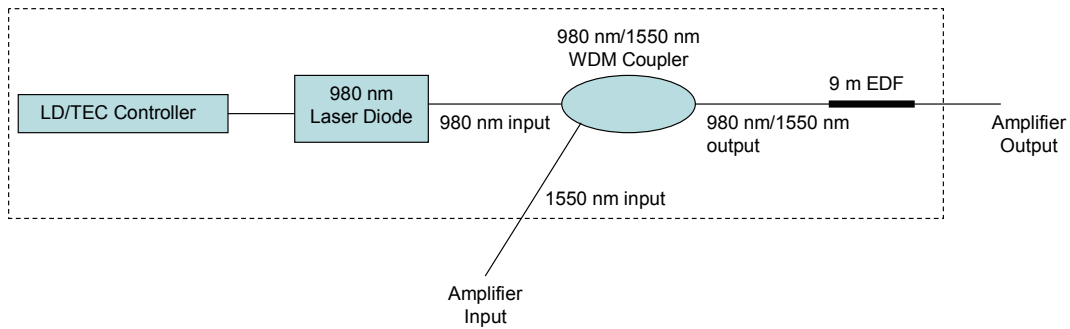


Figure 5.17: In-house built EDFA for the FBG-based strain sensors interrogation systems.

One of the issues encountered when using EDFAs as gain media in fiber laser systems is the single wavelength imposed by the homogenous gain broadening that characterizes Erbium doped media. This was observed experimentally when adding the fiber mirror used to establish the standing wave fiber laser configuration. As a result, measurements were performed for one FBG only for the purpose of exploring the improvement in performance that can be achieved using an amplifying medium other than an SOA. Note that for the ring fiber laser configuration, a unidirectional EDFA was used, instead of the in-house built EDFA.

The measured power as a function of applied strain for the standing wave and for the ring fiber laser configurations against the non-lasing configurations are shown in Figures 5.18 and 5.19, respectively. As observed, the measured power at the output of the corresponding AWG channel is enhanced when either fiber laser interrogation system is

used. Moreover, the wavelength to power mapping resolution improvement is much easily detected when the SOA is replaced by an EDFA. Note that the separate comparisons of the lasing configurations against the non-lasing configuration are plotted on different graphs because different EDFAs were used for the two former systems.

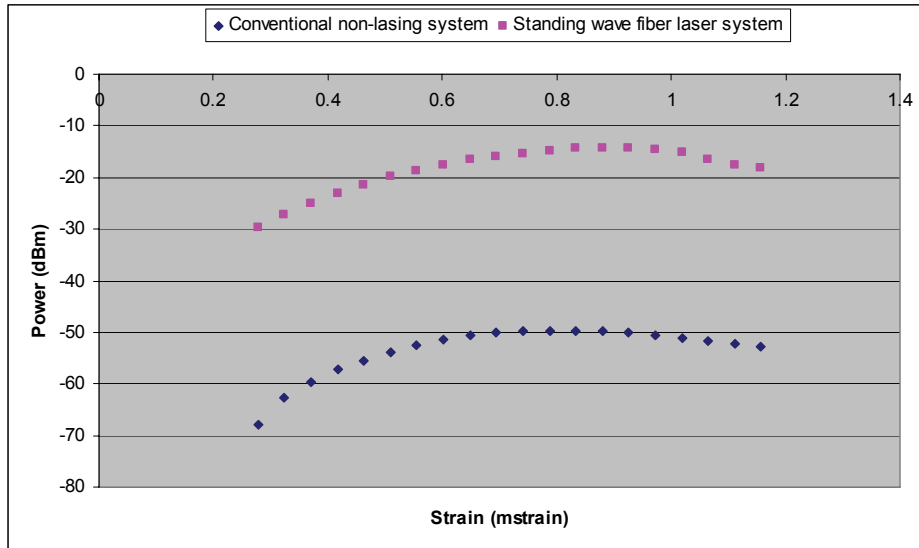


Figure 5.18: Measured power at the output of the AWG as a function of strain for the sensor whose reflection spectrum is centered at 1538.32 nm when the in-house built EDFA is used.

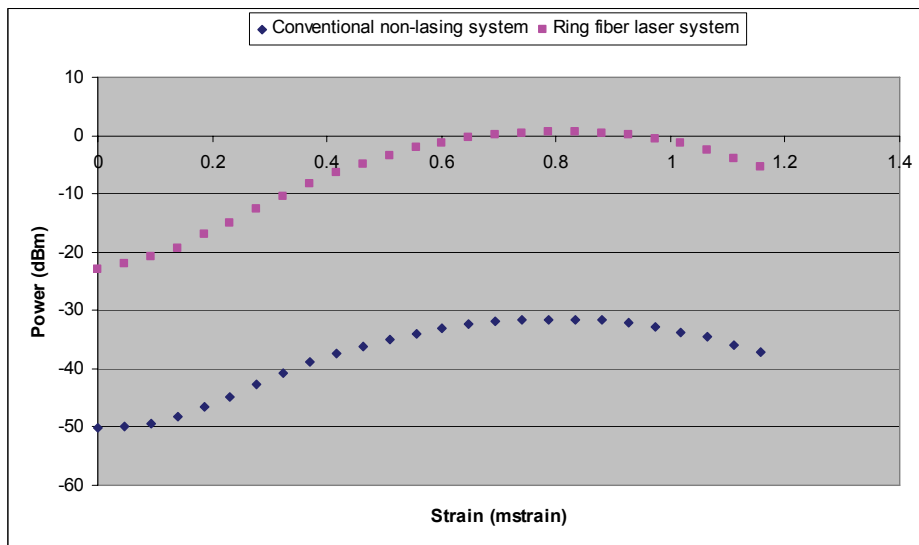


Figure 5.19: Measured power at the output of the AWG as a function of strain for the sensor whose reflection spectrum is centered at 1538.32 nm when a unidirectional EDFA is used.

The resolution plots of normalized power as a function of applied strain are shown in Figures 5.20 and 5.21, respectively, for the systems using an in-house built EDFA and an INO EDFA. These figures show that the ring fiber laser configuration provides better resolution than the standing wave configuration.

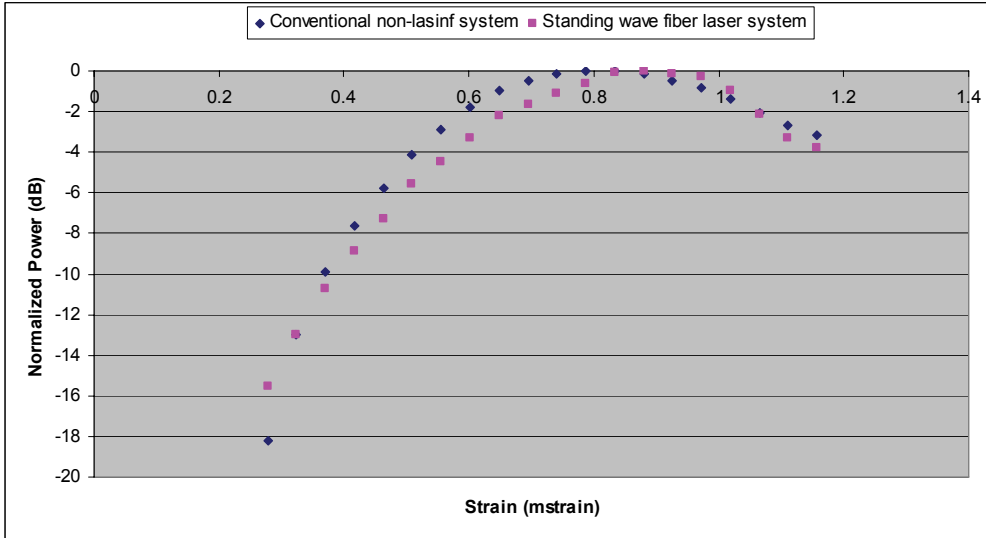


Figure 5.20: Normalized measured power at the output of the AWG as a function of strain for the sensor whose reflection spectrum is centered at 1538.32 nm when the in-house built EDFA is used.

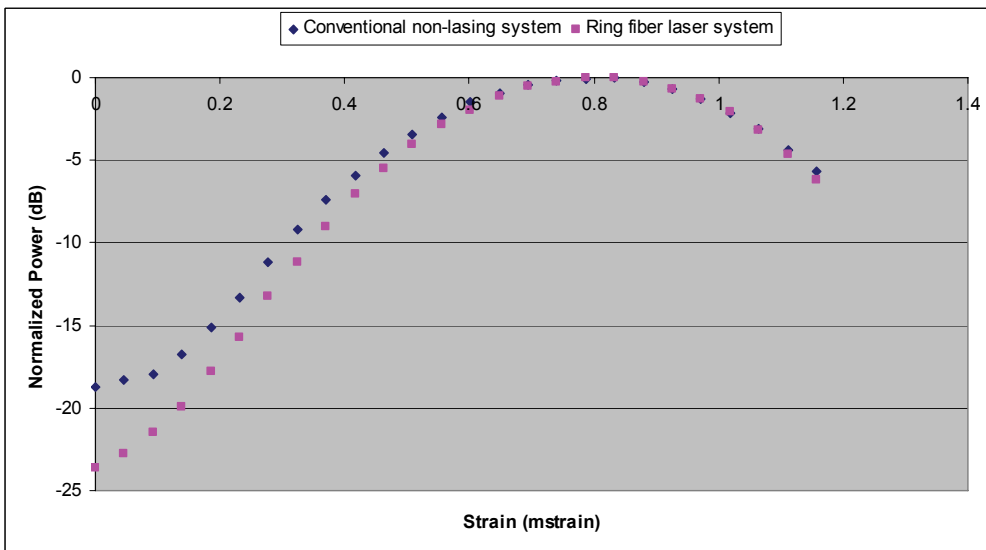


Figure 5.21: Normalized measured power at the output of the AWG as a function of strain for the sensor whose reflection spectrum is centered at 1538.32 nm when a unidirectional EDFA is used.

As previously reported and as predicted by theory, using the lasing interrogation systems cause the 3 dB level bandwidth of the FBG spectrum to narrow. As such, for the FBG centered at 1538.32 nm, for which the EDFA-based fiber laser response was investigated, when the in-house built EDFA is used, the non-lasing spectrum bandwidth is 225 pm, while the lasing bandwidth is 48 pm. When the INO EDFA is used in the ring configuration, the non-lasing bandwidth is 216 pm, and the lasing bandwidth is 52 pm. The OSA trace of this FBG when using an EDFA is shown in Figure 5.22. Table 5.3 summarizes the reduction in BW for the FBGs reflection spectra and the associated decrease in wavelength measurement errors for both cases, when the in-house built EDFA and the INO EDFA were used as BBSs and gain media in the standing wave and ring configurations, respectively.

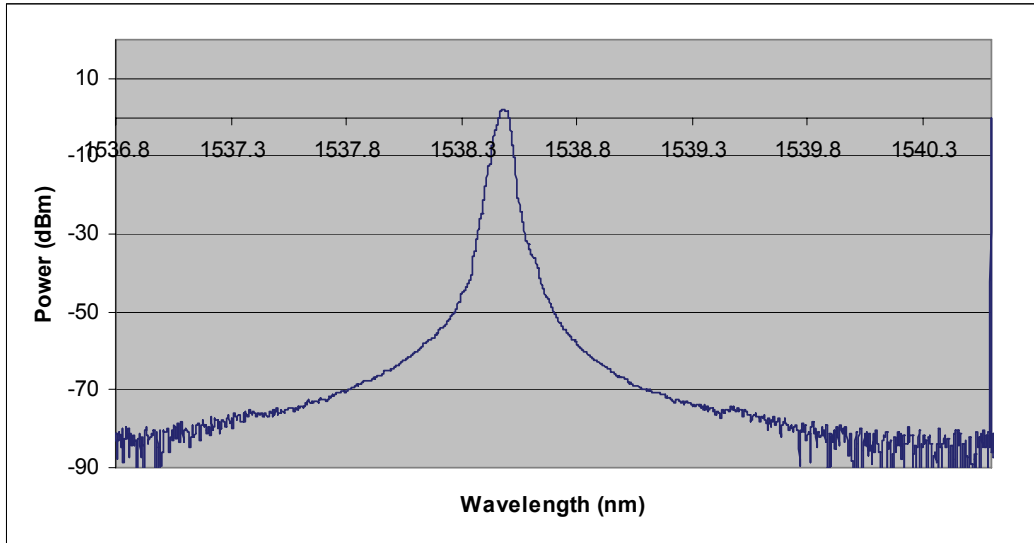


Figure 5.22: Spectral characteristic of FBG 2 when using the fiber laser configuration when an EDFA is used as gain medium.

Table 5.3: Summary of FBG reflection spectra measured bandwidths with the associated wavelength measurement errors when an EDFA is used as BBS and as gain medium:

Center Wavelength (nm)	Non-Lasing (in-house)		Non-Lasing (INO)		Standing Wave (in-house)		Ring (INO)	
	3dB BW (pm)	Error (pm)	3dB BW (pm)	Error (pm)	3dB BW (pm)	Error (pm)	3dB BW (pm)	Error (pm)
1538.32	225	458	216	454	48	402	52	403

5.5.3 Continuous-Time Measurement Results

The experimental results presented earlier were measured in a quasi-steady-state manner. It is also important to investigate the dynamic response of the system, i.e., to assess the suitability of the system to capture dynamically varying perturbations. For this purpose, two experiments were conducted using the setup in Figure 5.23. Note that the experiment was conducted using an RSOA (reflective SOA) as the BBS and gain medium for the fiber laser system.

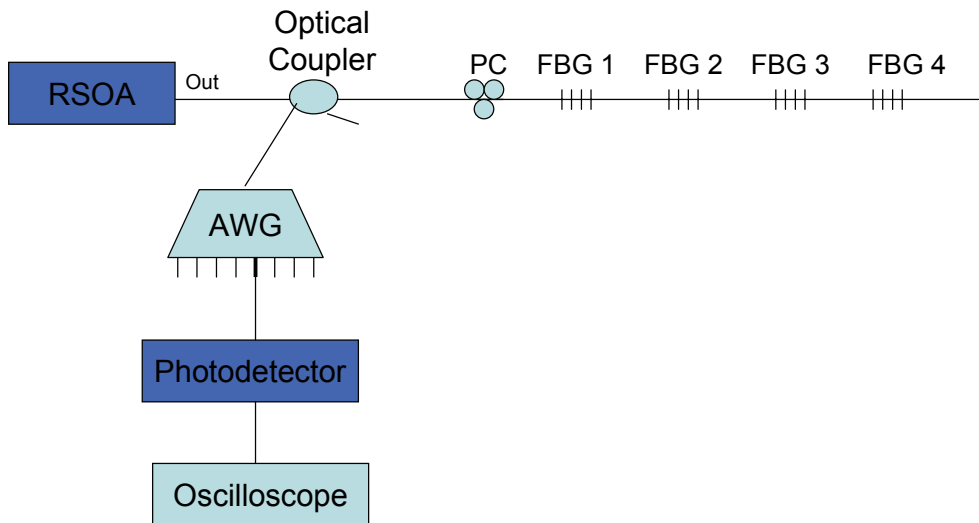


Figure 5.23: Experimental setup for time-domain measurements using an RSOA.

A) Strain and Temperature Effect on the Time-Domain Signal

A first set of experiments were conducted using one FBG immersed in a water filled ultrasonic bath, which emits a signal at 42 kHz. As a result, the FBG is strained or compressed as the fiber follows the ultrasonic signal. At room temperature, when the position of the FBG spectrum relatively to its corresponding AWG signal is as shown in Figure 5.24, the signal measured with the oscilloscope follows a sinusoidal variation in time, at the same frequency as the ultrasonic signal as illustrated in Figure 5.25.

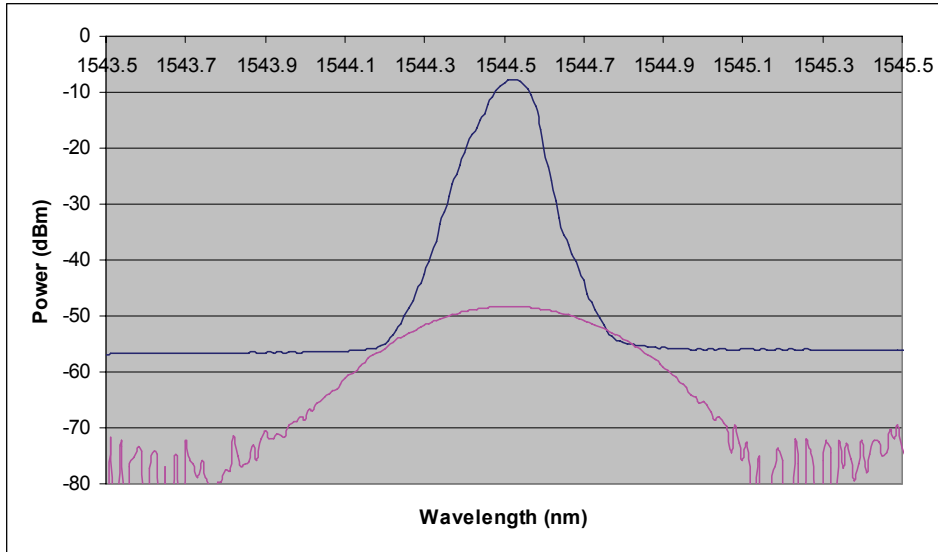


Figure 5.24: The FBG and AWG spectra when the former is placed in the ultrasonic bath at 25 °C.

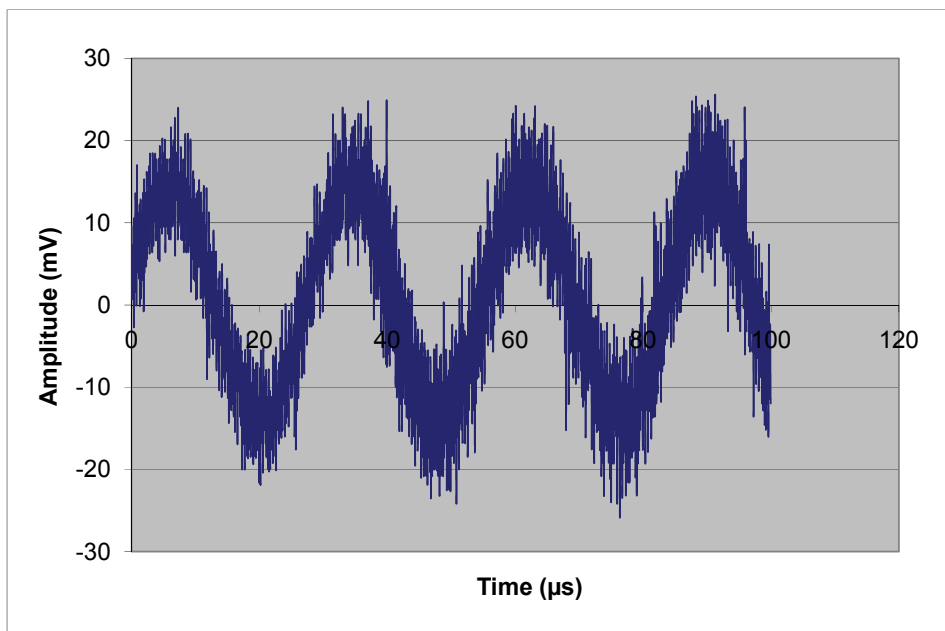


Figure 5.25: Response to the ultrasonic signal when the FBG is placed in the ultrasonic bath at 25 °C.

On the other hand, when the temperature is increased to 50 °C, the FBG is positioned relatively to the AWG channel as shown in Figure 5.26, and the photodetector signal as measured with the oscilloscope experiences a higher amplitude sinusoidal variation, as shown in Figure 5.27. As expected, when the FBG moves towards longer wavelengths when temperature increases, the DC level follows the AWG power level. In this case, as

illustrated in Figure 5.28 a) and b), the DC value decreases from 3.33 V to 2.16 V because at room temperature the spectra of the FBG and AWG overlap at a wavelength close to the peak of the AWG spectrum, whose slope is steeper on its falling or rising edges. As a result, at 50 °C, the ultrasonic signal is translated to an oscilloscope signal of higher amplitude.

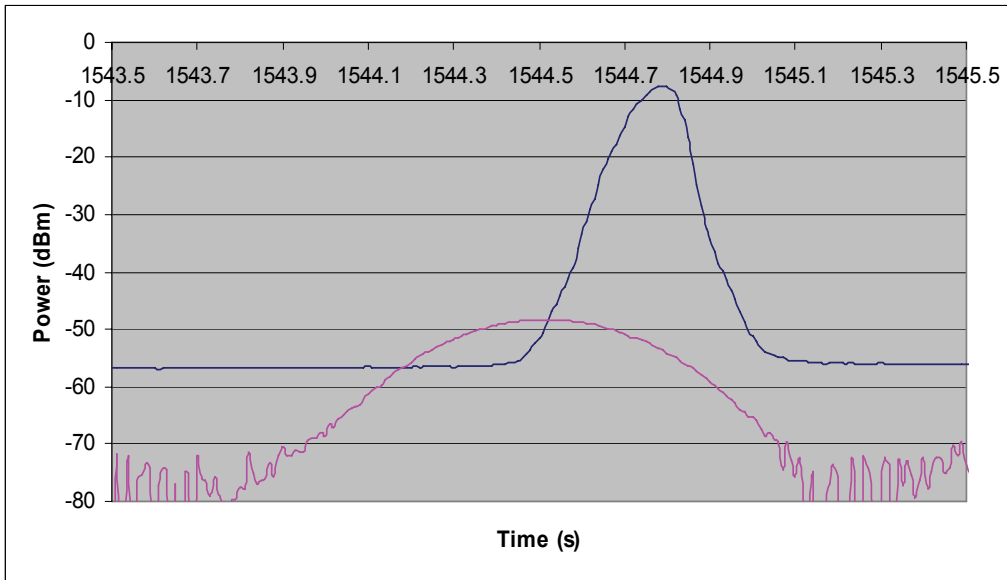


Figure 5.26: The FBG and AWG spectra when the former is placed in the ultrasonic bath and water is heated to 50 °C.

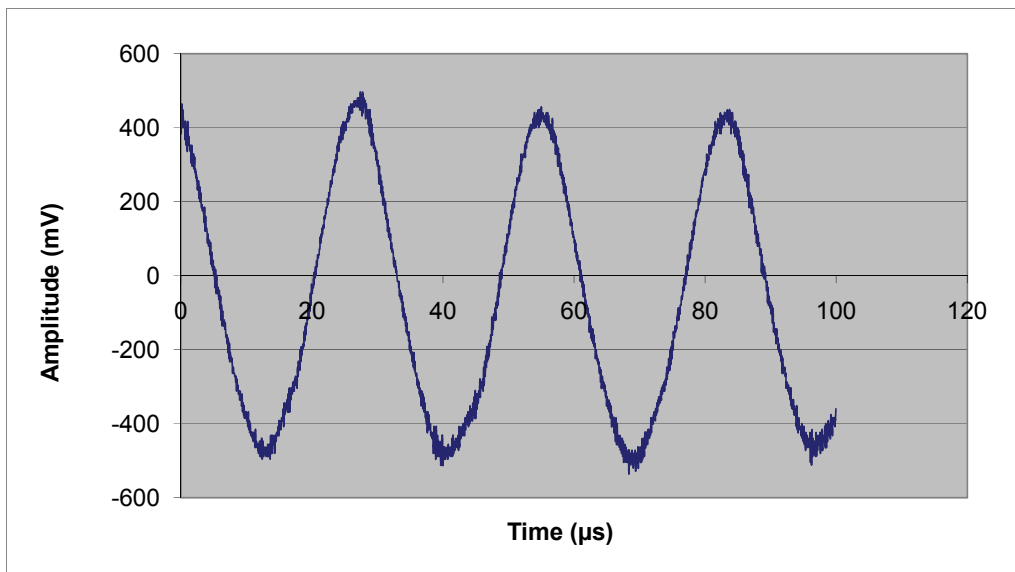
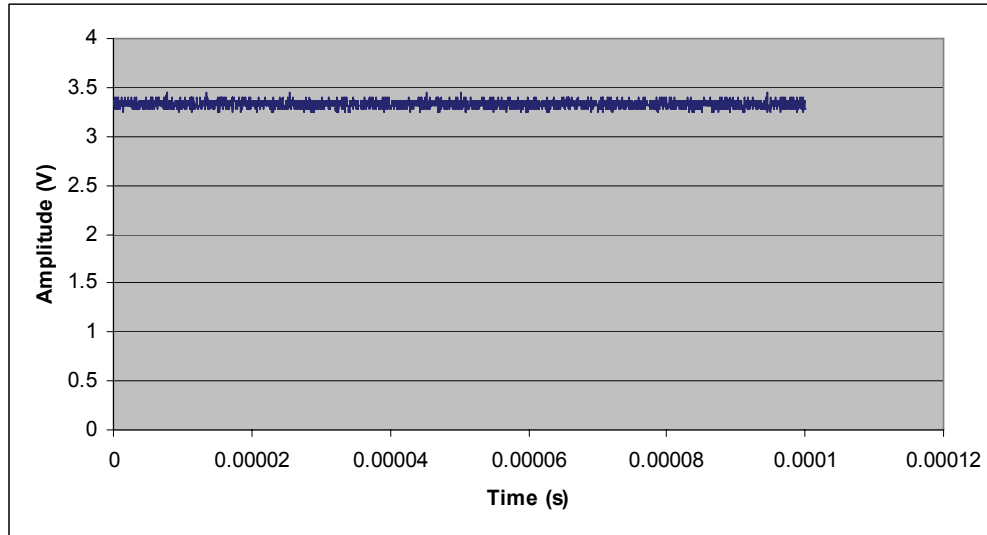
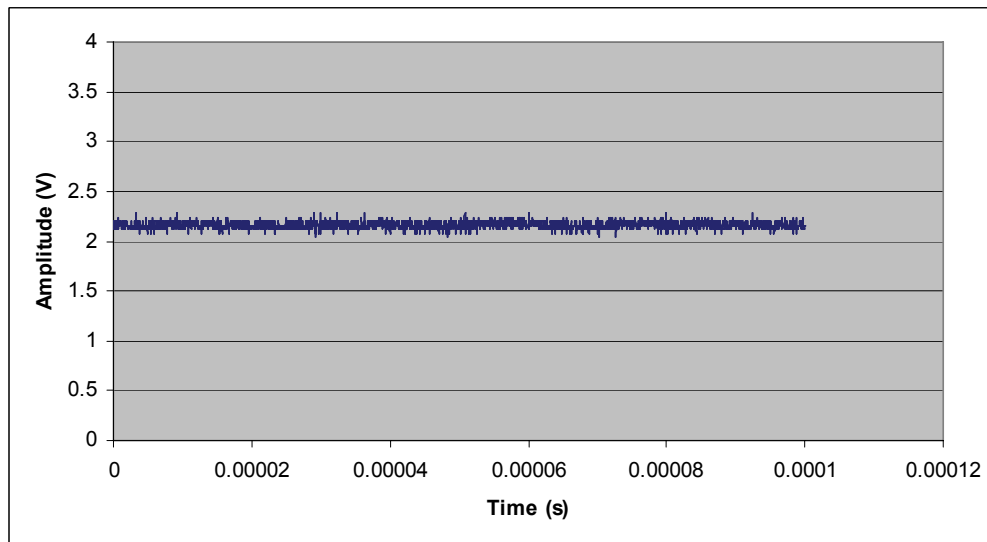


Figure 5.27: Response to the ultrasonic signal when the FBG is placed in the ultrasonic bath at 50 °C.



a)



b)

Figure 5.28: DC amplitude level when the temperature is a) 25 °C, and b) 50 °C.

B) Strain Calibration Measurements

To quantify the amount of strain applied to the FBG (center wavelength at 1538.32 nm as used in the previous experiments) by the ultrasonic signal, a calibration measurement that maps wavelength change to mean amplitude change for the DC signal measured using the oscilloscope is necessary. Thus, Figures 5.29 and 5.30 show the change in wavelength and the change in DC mean amplitude, respectively as functions of applied strain, which is quantified by placing the FBG on the strain system used to perform the discrete measurements. These curves were then used to achieve the mapping

curve, whose rising or falling edges are shown in Figure 5.31 a) and b), respectively, to achieve a one-to-one correlation between the change in wavelength with strain and the mean amplitude measured with the oscilloscope.

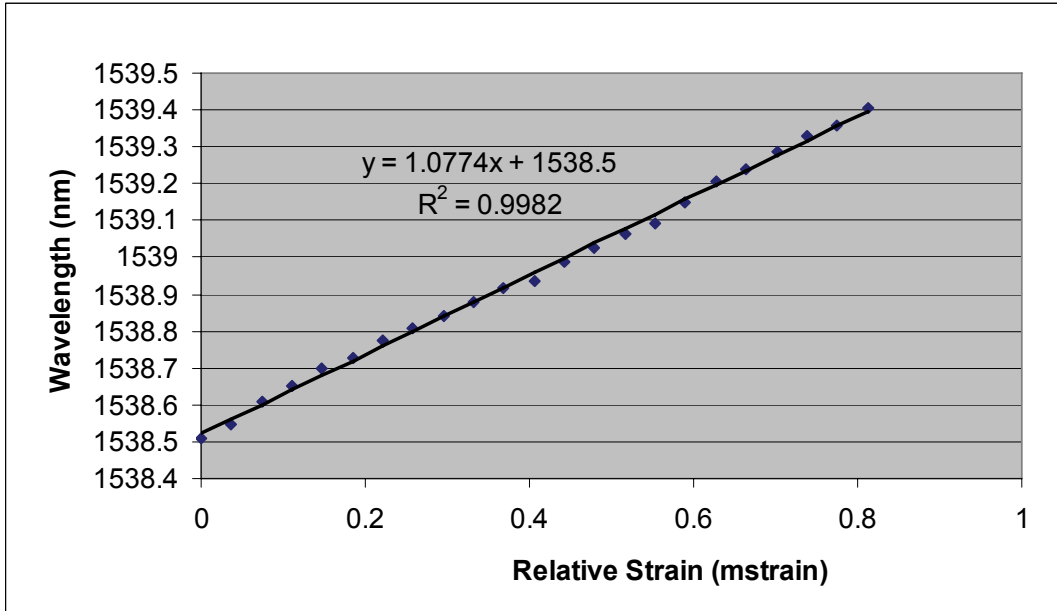


Figure 5.29: FBG wavelength as a function of applied strain.

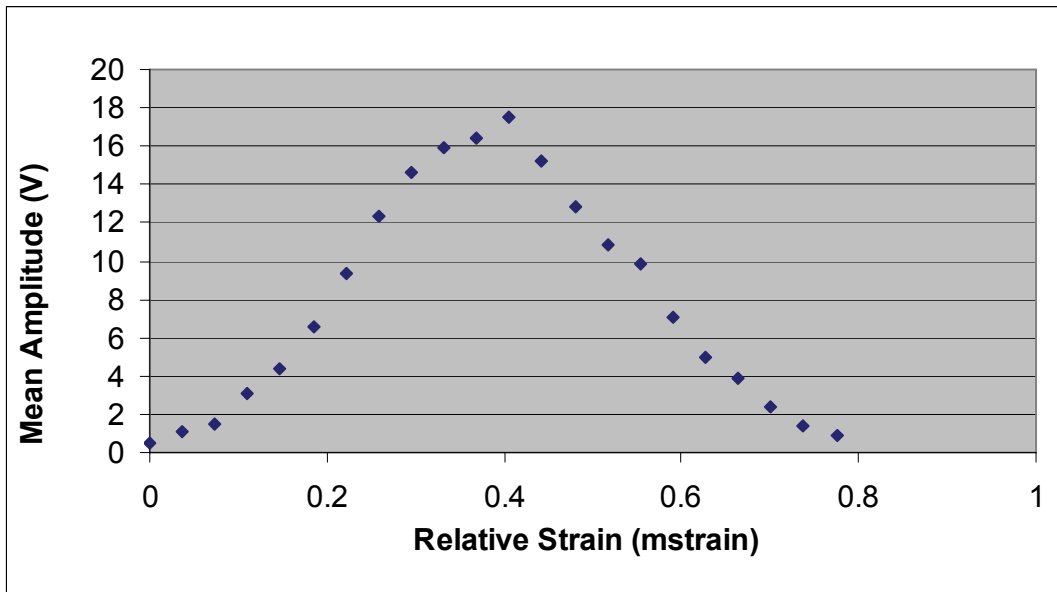
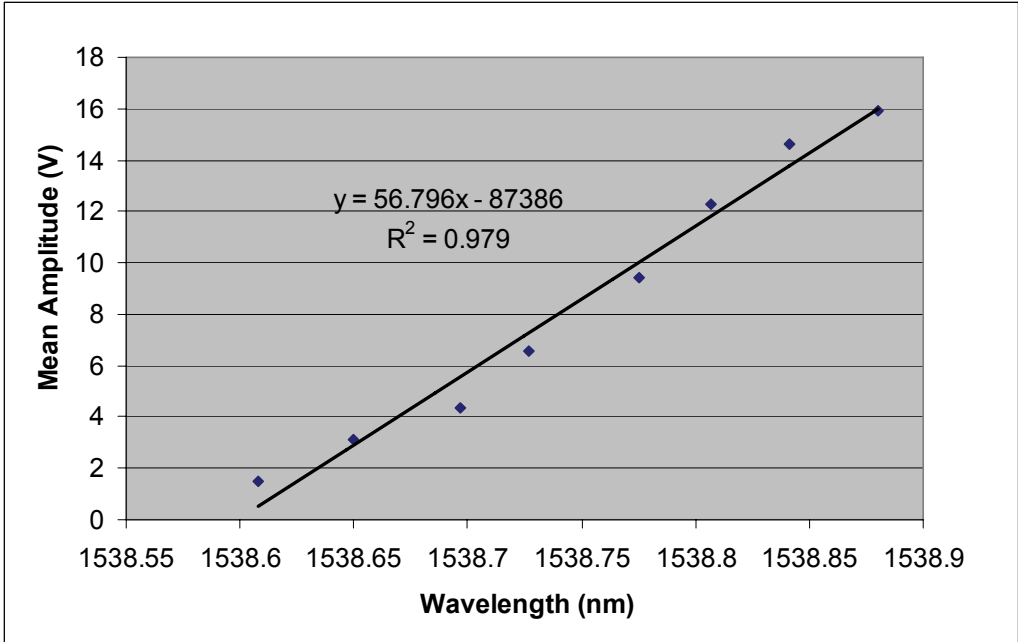
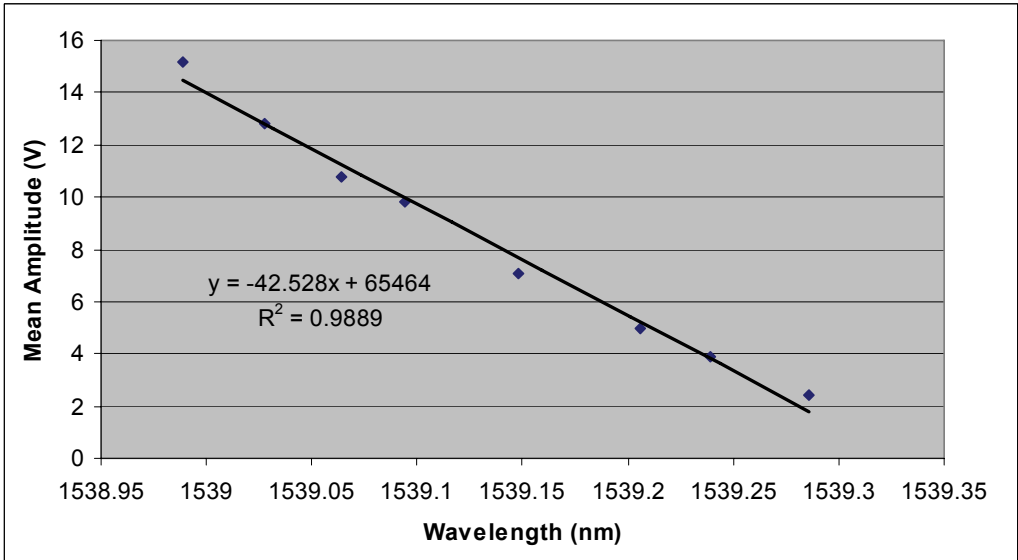


Figure 5.30: Measured mean amplitude measured with the oscilloscope at the output of the AWG channel corresponding to the FBG under test as a function of applied strain.



a)



b)

Figure 5.31: Wavelength-to-electric signal mean amplitude mapping when the FBG overlaps with a) the rising, and b) the falling edges of the AWG channel.

5.6 Discussion and Conclusion

The experimental results successfully demonstrate that using FBGs as part of fiber laser systems helps improve the power efficiency of the wavelength to power mapping procedure previously proposed, i.e., the power enhancement is about 30 dB or more. However, when using the ring fiber laser configuration shows a gain higher by about 10 dB than the standing wave configuration. Moreover, the results also depend on the broadband source used. As such, using an SOA as broadband source and as gain medium shows multiple wavelengths lasing characteristic, while using an EDFA only supports one wavelength. Experimental work using both gain media confirms the prediction that fiber laser systems reduce the 3 dB level bandwidth. However, only a slight increase in wavelength to power mapping resolution is observed. Moreover, using the EDFA as part of the lasing system shows a slightly increased wavelength to power mapping resolution, which may be accounted for by the further decrease in FBG reflection spectrum 3 dB level bandwidth.

Note that the experiments on the FBG wavelength to power mapping systems were performed at constant temperature. However, from a practical perspective, strain sensors are usually used in environments that experience temperature fluctuations, which induce wavelength changes, and may lead to erroneous wavelength to power mapping. Therefore, to obtain reliable strain measurement, further work may involve incorporating a temperature compensation system. Moreover, since the system relies on power measurement, it is important that the fiber laser power levels remain stable in time and are insensitive to external physical perturbation. For this purpose, it is important to work with amplifiers showing relatively low polarization dependence, such that any external disturbance to the fiber or to the FBGs does not affect the power of the lasing mode. This is a problem encountered when using SOAs, whose gain dependence on polarization ranges from very high to very low values. One advantage of having a gain that is highly dependent on polarization is the ability to achieve improved wavelength selectivity; nevertheless, small changes in fiber birefringence amount for large changes in the power level of the lasing wavelengths. Therefore, when evaluating the performance of a fiber laser system, it is necessary to have not only the required lasing characteristics, which for sensor systems imposes a restraint on the number of lasing wavelengths, but also a high

degree of stability, which increases the chances of having reliable parameter measurement.

5.7 References

- [5.1] L. Zhang, W. Zhang, and I. Bennion, “In-Fiber Grating Optic Sensors” in *Fiber Optic Sensors* edited by Shizhuo Yin, Paul B. Ruffin, and Francis T.S. Yu, pp. 109-162, CRC Press, Boca Raton, FL, 2008.
- [5.2] D.C.C. Norman, D.J. Webb, and R.D. Pechstedt, “Extended range interrogation of wavelength division multiplexed fibre Bragg grating sensors using arrayed waveguide grating,” *Electronics Letters*, vol. 39, no. 24, pp. 1714 – 1716, 2003.
- [5.3] F.G. Sun, G.Z. Xiao, Z.Y. Zhang, and Z.G. Lu, “Modeling of arrayed waveguide grating for wavelength interrogation application,” *Optics Communications*, vol. 271, pp. 105–108, 2007.
- [5.4] G.Z. Xiao, P. Zhao, F. Sun, Z. Lu, and Z. Zhang, “Arrayed-waveguide-grating-based interrogator for wavelength-modulated multi-fiber-optic sensor applications,” *IEEE Photonics Technology Letters*, vol. 17, no. 8, pp.1710-1712, 2005.
- [5.5] P. Niewczas, A.J. Willshire, L. Dziuda, and J.R. McDonald, “Performance analysis of the fiber Bragg grating interrogation system based on an arrayed waveguide grating,” *IEEE Transactions on Instrumentation and Measurement*, vol. 53, no. 4, pp. 1992-1196, 2003.
- [5.6] S. Abad, F.M. Araújo, L.A. Ferreira, J.L. Santos, and M. López-Amo, “Interrogation of wavelength multiplexed fiber Bragg gratings using spectral filtering and amplitude-to-phase optical conversion,” *Journal of Lightwave Technology*, vol. 21, no. 1, pp. 127-131, 2003.
- [5.7] A. Yariv and P. Yeh, “Theory of laser oscillation and some specific laser systems” in *Photonics: Optical Electronics in Modern Communications*, 6th ed., pp. 237-312, Oxford University Press, New York, NY, 2007.
- [5.8] C.H. Yeh, C.W. Chow, Y.F. Wu, F.Y. Shih, C.H. Wang, and S. Chi, “Multiwavelength Erbium-doped fiber ring laser employing Fabry–Perot etalon inside cavity operating in room temperature,” *Optical Fiber Technology*, vol. 15, pp. 344–347, 2009.
- [5.9] S. Feng, O. Xu, S. Lu, X. Mao, T. Ning, and S. Jian, “Switchable dual-wavelength Erbium-doped fiber-ring laser based on one polarization maintaining fiber Bragg grating in a Sagnac loop interferometer,” *Optics and Laser Technology*, vol. 41, pp. 264– 267, 2009.
- [5.10] X. Liu, “A novel dual-wavelength DFB fiber laser based on symmetrical FBG structure,” *IEEE Photonics Technology Letters*, vol. 19, no. 9, pp. 632-634, 2007.

- [5.11] Y. Liu, X. Dong, P. Shum, S. Yuan, G. Kai, and X. Dong, "Stable room-temperature multi-wavelength lasing realization in ordinary Erbium-doped fiber loop lasers," *Optics Express*, vol. 14, no. 20, pp. 9293-9298, 2006.
- [5.12] O. Xu, S. Lu, S. Feng, Z. Tan, T. Ning, and S. Jian, "Single-longitudinal-mode Erbium-doped fiber laser with the fiber-Bragg-grating-based asymmetric two-cavity structure," *Optics Communications*, vol. 282, pp. 962-965, 2009.
- [5.13] W. Guan and J.R. Marciante, "Dual-frequency operation in a short-cavity Ytterbium-doped fiber laser," *IEEE Photonics Technology Letters*, vol. 19, no. 5, pp. 261-263, 2007.
- [5.14] Z. Zhang, J. Wu, K. Xu, X. Hong, and J. Lin, "Tunable multiwavelength SOA fiber laser with ultra-narrow wavelength spacing based on nonlinear polarization rotation," *Optics Express*, vol. 17, no. 19, pp. 17200-17205, 2009.
- [5.15] D.S. Moon, B.H. Kim, A. Lin, G. Sun, W.-T. Han, Y.-G. Han, and Y. Chung, "Tunable multi-wavelength SOA fiber laser based on a Sagnac loop mirror using an elliptical core side-hole fiber," *Optics Express*, vol. 15, no. 13, pp. 8371-8376, 2007.
- [5.16] H. Ahmad, A. H. Sulaiman, S. Shahi, and S.W. Harun, "SOA-based multi-wavelength laser using fiber Bragg gratings," *Laser Physics*, vol. 19, no. 5, pp. 1002-1005, 2009.
- [5.17] S. Tanaka, K. Inamoto, H. Yokosuka, H. Somatomo, and N. Takahashi, "Multi-wavelength tunable fiber laser using SOA: application to fiber Bragg grating vibration sensor array," *IEEE Sensors Conference*, pp. 411-414, 2007.
- [5.18] N.Y. Voo, P. Horak, M. Ibsen, and W.H. Loh, "Linewidth and phase noise characteristics of DFB fibre lasers" in *SPIE European Symposium on Optics and Photonics in Security and Defence*, vol. 5620, pp. 179-186, London, 2004.
- [5.19] H. Su and X.G. Huang, "A novel fiber Bragg grating interrogating sensor system based on AWG demultiplexing," *Optics Communications*, vol. 275, pp. 196-200, 2007.
- [5.20] G.Z. Xiao, P. Zhao, F.G. Sun, Z.G. Lu, Z. Zhang, and C.P. Grover, "Interrogating fiber Bragg grating sensors by thermally scanning a demultiplexer based on arrayed waveguide gratings," *Optics Letters*, vol. 29, no. 19, pp. 2222-2224, 2004.
- [5.21] X.J.M. Leijtens, B. Kuhlow, and M.K. Smit, "Arrayed Waveguide Gratings" in *Wave-length Filters in Fibre Optics* by H. Venghaus, pp. 125-187. Springer-Verlag Berlin Heidelberg: Berlin, Germany, 2006.

- [5.22] O. Frazão, S.F.O. Silva, A. Guerreiro, J.L. Santos, L.A. Ferreira, and F.M. Araújo, “Strain sensitivity control of fiber Bragg grating structures with fused tapers,” *Applied Optics*, vol. 46, no. 36, pp. 8578-8582, 2007.
- [5.23] Y. Zhao and Y. Liao, “Discrimination methods and demodulation techniques for fiber Bragg grating sensors”, *Optics and Lasers in Engineering*, vol. 41, pp. 1-18, 2004.

6. Conclusion and Future Work

This thesis proposes and demonstrates the feasibility of using a number of interrogation systems for FBG-based sensors. As presented in Chapter 2, understanding the theory behind such sensors, and acquiring knowledge about previous work performed toward designing practical detection systems are important for identifying existing issues. This leads to finding cost effective and reliable solutions. Moreover, before commercialization, it is important to make sure the sensors can be reliably used. Therefore, Chapter 3 provided an example of characterizing a ready-to-be-commercialized vibration sensor based on a twin FBG pair, and the tests performed on them include operability region, sensor reliability, which is given by the ability of the sensor to measure a unique value for every vibration amplitude and frequency conditions. It was found that a typical calibration curve is linear, with the slope giving the sensor's sensitivity. Moreover, it is important to make sure that, for a given vibration condition, the measurement does not vary considerably, so the system does not measure a different condition than the real one, thus leading to detection errors. In the same chapter, it was found that multiplexing requires a trade-off between the sensor design and the sensing requirements, i.e., if the sensors are designed to acquire data over long distances, the maximum number of sensors can be tailored by increasing the reflectivity of the last sensor in the array, or by decreasing the reflectivities of the preceding FBGs. Another alternative would be to increase the power sent to the multiplexed sensors. On the other hand, for pre-defined system conditions, the number of sensors that can be time-division multiplexed can be increased by decreasing the length span over which sensing is performed.

Chapter 4 presents an extension of the basic design of the vibration sensor to achieve either temperature or strain measurements. As discussed, temperature measurement is used to prove that the ability of the FBG pair structure to slice a broadband beam can be used to tune the peak of a single passband MPF. It was found that, for given temperature conditions, the MPF has a unique value that depends on the dispersion characteristic of the fiber in response to the change experienced by the FBG pair reflection spectrum: both the center wavelength and the FSR of the interference signal increase with temperature;

however, the former changes more compared to the latter. It was demonstrated that, driving the modulator in the MPF system with an RF signal falling on either the rising or the falling edge of the pass-band of the filter results in a linear change in the measured power at the output. It was observed that the MPF characteristic changes so different linearity and sensitivities are obtained—this gives flexibility to the measurement system. For the proposed system, the delay component was an 85 km long SMF, which added loss to the system and made it unpractical. Therefore, future work involves designing the FBG pair so the interference pattern FSR increases, e.g. decrease the separation between the FBGs. Moreover, keeping the sensor design intact, a shorter length of higher dispersion fiber can be used as the MPF delay element to obtain the observed filtering characteristics. In terms of application, in the future the sensor may be used as temperature compensation component when measuring vibration or strain. Note that the latter can greatly benefit from using an MPF system, which is characterized by high speed capability and would allow the fast real-time monitoring of strain.

A second system presented in Chapter 5 provided a solution to obtaining portable, cost effective, and power efficient interrogation systems for FBG strain or temperature sensors. The experimental work treated the measurement of strain, and it involved using an AWG to map the wavelength-encoded information to a power measurement, which allows using cheap and portable instrumentation such as power meters to detect the changes in the FBG reflection spectrum with strain. Moreover, the system was designed in a fiber laser configuration, which provided amplified power (by up to 35 dB), thus increasing the power efficiency of the system. Another aspect that was investigated in this work is the effect the gain medium has both the lasing characteristic of the system (power efficiency) and on the mapping characteristics. The two BBS explored were SOAs and EDFAs. It was found that the former experiences better lasing behaviour than the latter, which, even though it provides slightly improved mapping, experiences single wavelength lasing, and this prevents the effective use of WDM sensor systems. For this work, future work involves investigating the number of sensors supported by the lasing system, i.e., for a given BBS and gain medium, what would the maximum number of sensors that experience lasing with equalized power levels be. Moreover, in general lasers experience instabilities with changing polarization or fiber birefringence, and, therefore,

for practical applications, it is important to characterize the system in terms of stability. Another important parameter that needs to be explored to extend the study to practical applications would be achieving a practical temperature compensation scheme.